Study of High Energy Density Matter through Quantum Molecular Dynamics and Time Resolved X-ray Scattering

Thomas G. White

Trinity College

University of Oxford

A thesis submitted for the degree of

Doctor of Philosophy

Trinity term, 2014

This thesis is dedicated to
Sam, Cameron and Patricio
for their guidance, encouragement and support.

Study of High Energy Density Matter through Quantum Molecular Dynamics and Time Resolved X-ray Scattering

Thomas G. White

Trinity College, University of Oxford

A thesis submitted for the Degree of Doctor of Philosophy

Trinity term, 2014

Abstract

The warm dense matter regime (WDM), defined by temperatures of a few electron volts and densities comparable with solids, is a complex state of matter where multi-body particle correlations and quantum effects play an important role in determining the overall structure and equation of state. The study of WDM states represents the laboratory analogue of the astrophysical environments found in the cores of planets and in the crusts of old stars, but also has practical applications for controlled thermonuclear fusion.

Time resolved X-ray diffraction is used to study the temporal evolution of a sample from solid state towards WDM, either after irradiation with an intense proton/electron beam, in carbon samples, or direct laser illumination, in thin gold nanofoils. The electron-ion equilibration time is extracted through the use of the two-temperature model and in highly excited carbon shown to be longer than previously thought, this is attributed to strong ion-ion coupling screening the interaction (coupled mode theory).

Calculation of the dynamic ion-ion structure factor is performed using orbital-free density functional theory (OF-DFT) and shown to compare well with Kohn-Sham DFT in both the static and dynamic cases. Experimental verification of these results is vital and measurement of the microscopic dynamics of warm dense aluminium have been successfully demonstrated through inelastic X-ray scattering. Using the self-seeded beam at the linear coherent light source (LCLS) scattering at a small momentum exchange allowed the first direct measurement of ion acoustic waves in WDM. This data provides the basis for a direct experimental test of many dense plasma theories through direct comparison with the ion-ion dynamic structure factor.

Acknowledgements

During this work I have been given an enormous number of opportunities, far beyond those expected during a DPhil, and so it is with immense gratitude that I acknowledge the support and guidance of my supervisor, Gianluca Gregori, without whom none of this would have been possible. His encouragement, intuition and, towards the end, patience, has allowed me to achieve all that I have. Besides my principle advisor I also wish to thank Basil Crowley, Scott Richardson, Lee Pattison and James Harris, not just for the funding that allowed me to perform this research, but also the many hours of intense discussion.

I have been exceptionally lucky to have been taught, guided, but most of all distracted, by three excellent post-docs throughout my DPhil. My utmost thanks go to Chris Murphy, Hugo Doyle and Andy Higginbotham for the discussions, however tenuously linked to physics, and for teaching me that the most important physics gets done in the pub!

Next I would like to thank Marcel Stanitzki and Jan Strube for introducing me to the world of physics research during my master's degree and to Peter Norreys for pointing me in the direction of the Oxford HEDP group.

This work is the result of a large collaborative effort and I am indebted to my many colleagues who supported me throughout. Most notably Paul Neumayer, Sebastien Le Pape and Tammy Ma who guided me through my first experimental campaigns but also to fellow scientists Ulf Zastrau, Guilio Monaco, Karen Appel, Dominik Kraus, Anke Otten, Markus Roth, Daniel Hochhaus, Tilo Döppner, Art Pak, Luke Fletcher, Siegfried Glenzer, Jerry Hastings, Don Lamb and Thomas Tschentscher. Additionally, the international facilities I have used for this work require large dedicated teams of staff and engineers, far too many to mention, but all of whom I thank for their tireless work. I must also thank Jan Vorberger, Dirk Gericke, Alex Robinson and Sebastien Hamel for helpful discussions and contributions towards data analysis and simulations.

Thanks are due to my fellow students past and present, James, Katja, Robin, Nick, Jena, Shamim, Paul, Pawel and David whose insight and company was always appreciated.

Very special thanks go to Sam, Cameron, Patricio, Gen, Richard, Joe, Becky, Phil, Sarah, Jay, Celia and Luke for providing me with a welcome distraction from physics and the much needed support over the past four years. Finally, despite your poor knowledge of physics, my heartfelt thanks go to Sam who had the arduous task of putting up with me while I completed the ordeal of thesis writing.

Last but not least, I would like to thank my family for their continued love and support over the years and special thanks must go to my parents, for teaching me to question everything and giving me the tools required to complete this body of work.

Role of the author in this work

This thesis presents both experimental and theoretical results relating to the creation, diagnosis and simulation of *high energy density physics* (HEDP) states of matter. Like most scientific efforts the work in this thesis is a collaborative effort and this section will attempt to make clear the nature of the author's contributions.

Chapters 1 and 2 are introductory chapters designed to review the essential background theory necessary to understand the work presented here. These chapters are reproduced from a variety of sources and the original authors are all identified clearly throughout the text.

The original work in this thesis is presented throughout chapters 3-5. Chapter 3 describes an experimental investigation into temperature relaxation in non-equilibrium high energy density matter. This chapter contains details on three experiments:

- *Temperature relaxation in graphite heated by a high intensity proton beam.* This experiment was conceived by G. Gregori and performed on the Titan laser at Lawrence Livermore National Laboratory in 2011. It was performed by an experimental team of six scientists including the author. The analysis was performed solely by the author and this work is published in Scientific Reports, see White *et al.* (2012) [209].

- *Temperature relaxation in graphite heated by a high intensity electron beam.* This experiment was conceived by P. Neumayer, G. Gregori and the author and performed on the PHELIX laser at GSI, Darmstadt in 2012 by an experimental team of eight scientists led by the author. The analysis was performed by the author and this work is published in Physical Review Letters, see White *et al.* (2014) [206].

- *Temperature Relaxation in gold nanofoils heated through direct laser illumination.* This experiment was conceived by A. Higginbotham and performed on a Ti:Saphire 40 fs terawatt laser in the HEDP laboratory in Oxford in 2013 by an experimental team led by the author. The analysis was performed by the author and P. Mabey. This work is published in Physical Review B, see White *et al.* (2014) [207].

Chapter 4 concentrates on the development of a new theoretical technique based on density functional theory (DFT) to extract both thermodynamic and transport

properties and structural dynamics of high energy density matter. The work in this chapter was carried out primarily by S. Richardson and the author. The code used to develop local pseudopotentials required by this method was developed primarily by the author based upon discussions with S. Richardson and L. Pattison. Details of the code are given in appendix C. The large scale DFT simulations required by this work were performed by S. Richardson on the AWE supercomputer blackthorn. All other work including comparison with classical simulations and calculations of dynamic structure factors were the work of the author. The results of this chapter have been published in Physical Review Letters, see White *et al.* (2013) [208]. Two large open-source codes were used throughout this work, ABINIT for the quantum molecular dynamics simulations and LAMMPS for the classical simulations.

Chapter 5 focuses on a proof of principle experiment performed in May 2013 at the Linear Coherent Light Source (LCLS) to measure the ion fluctuations in a dense plasma for the first time. Comparison of the results with the theoretical technique outlined in chapter 4 is performed, as well as analysis using more conventional hydrodynamic techniques. The work presented in this chapter represents the efforts of a large scale experimental collaboration. The experiment was conceived by G. Gregori and proposed by J. Hastings. The author along with G. Monaco played a major role during the experiment. Calculation of simulated scattering spectra and comparison with experimental data was carried out by the author. The analysis of this work is ongoing at the time of writing by the author and G. Monaco.

Work presented in the appendix is reproduced directly from other sources or modified to fit the extent of this work and all original authors are clearly identified in the text. The exceptions to this are appendices B and C which give details of computational codes written by the author. The first of these codes performs large-scale Fourier transforms of data from molecular dynamics simulations to predict scattering spectra. The second code uses a genetic algorithm to develop non-local pseudopotentials from local pseudopotentials for use in orbital-free DFT techniques.

Throughout this research the author has had the opportunity to contribute to numerous experimental campaigns on high intensity laser-matter interactions. This has lead to co-authoring numerous journal articles that are not directly relevant to the work presented in this thesis. A complete list of publications involving the author can be found in appendix J.

Contents

List of Figures

List of Tables

Chapter 1

Introduction

"There are infinite worlds both like and unlike this world of ours."

Epicurius, c.300 B.C.

At the dawn of the 16$^{\text{th}}$ century Nicolaus Copernicus suggested a dramatic change to our way of thinking and ousted the Earth from its, until then, unrivalled position at the centre of the universe. This new heliocentric view of the solar system whereby the planets revolve around the sun would go on to inspire Italian philosopher Giordano Bruno to predict, almost entirely correctly, that the sun was not unique in the universe and that there existed an infinite number of suns, each with their own planetary systems [70].

The search for these so called *exoplanets* did not really begin for over a century, and the first documented search was by Christiaan Huygens in 1698[1]. The first claimed discovery of an exoplanet occurred in 1855 when Captain W. S. Jacob of the East India Observatory suggested that orbital anomalies in the binary star system 70 Ophiuchi were caused by an orbiting planet. However, this was proven not to be the case. The first confirmed discovery of an exoplanet came in 1992 when Aleksander Wolszczan and Dale Frail discovered two planets orbiting the pulsar PSR B1257+12 [82, 212]. Since then a total of 1028 planets in 782 solar systems[2] have been discovered [180].

Planets with sizes ranging from Earth type masses to masses of up to twenty-two times that of Jupiter have now been discovered, and just like their solar counterparts

[1]This was actually before some of the largest inter-solar planets had been discovered. Uranus was discovered in 1781, Neptune in 1846 and Pluto not until 1930. Although Pluto was downgraded to "dwarf planet" in 2006.

[2]The rate of exoplanet discovery is rapidly increasing, and this number will surely be outdated before long.

many unanswered questions remain regarding their formation and evolution [142]. The cores of these planets can reach pressures above a megabar and temperatures of up to one hundred thousand kelvin, and any successful description must include the effects of strong ion-ion correlations and high electron degeneracy. Efforts to describe the structural dynamics of the cores of these planets, as well as those within our solar system, such as the *JUNO* mission to Jupiter scheduled to arrive in 2016 intended to measure higher order gravitational moments, are an area of intense scientific interest. This thesis is primarily concerned with the process of creating, diagnosing and modelling the behaviour of these extreme states of matter, a task that requires answering some fundamental physics questions spanning condensed matter, plasma physics and laser physics, and utilises recent technological advances in both high power lasers and ultra-fast X-ray science.

1.1 The Advent of High Energy Density Physics

The study of matter in extreme conditions, such as those found in the cores of Jovian planets, is now collectively known as *high energy density physics* (HEDP) and incorporates many other more traditional areas of physics including plasma physics and fusion energy, condensed matter, material science, astrophysics and laser and particle beam physics [52]. The most widely accepted definition of HEDP is the one set out in the US National Academy of Sciences, *Frontiers in High Energy Density Physics*, where a material should have an energy density of above 10^{11} J m^{-3}, or equivalently a pressure of order 1 Mbar [93]. This definition was chosen to be the pressure at which solid density matter compresses significantly, in other words it is the same order of magnitude as the internal energy of a hydrogen molecule $\sim$Mbar.

In order to study these extreme states of matter more easily scientists attempt to reproduce conditions relevant to these planetary core conditions here on earth. Accessing the high pressure and temperature regions of phase space requires inputting huge amounts of energy into a system, achieving this has typically required both large and costly machines, and as a result the major technological advances associated with this field of study has in general been driven by defence and the pursuit of fusion-energy.

Pressures above a Mbar cannot typically[3] be obtained during static compression, such as using a diamond anvil cell, but requires dynamic compression such as driving

[3]However, there is a trade off between sample volume and the maximum pressure which can be reached. With nano-diamond inserts small volumes of the order of a few cubic microns have recently been compressed to pressures of over 6 Mbar [53].

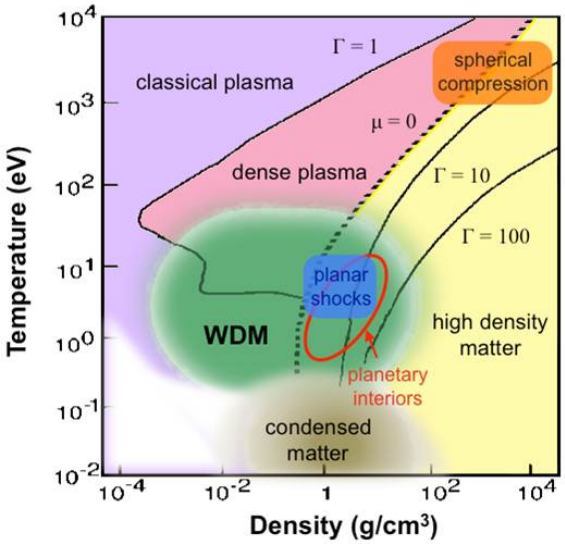

Figure 1.1: Phase diagram showing the location in phase space of the WDM regime. Figure reproduced from Ref. [57].

an intense shock wave through a material, often after high intensity laser irradiation. The first appearance of these high energy density conditions here on earth came with the development of nuclear weapons in the 1940s. These early underground nuclear explosion tests were often used as a driver for the shock compression of matter up to pressures of around 100 Mbar. However, this method of creation is no longer available after the recent *comprehensive nuclear-test-ban treaty* in 1996, and has necessitated the need to find alternative methods [32].

Two stage gas guns developed in the 1940s would use an explosive charge to drive a piston into a light gas, this in turn would rupture a diaphragm at a particular pressure, driving a flyer plate towards a sample at velocities approaching $\approx$10 km s^{-1}, reaching pressures in excess of 6 Mbar [36, 95]. Until recently the majority of work on obtaining high pressure equation of state (EOS) data from dense materials was carried out this way, however in the last few decades high intensity laser sources have been exploited to allow access to new, higher pressure, physical regimes in the laboratory. These intense laser-matter interactions can be used in a variety of forms to increase the energy of a system to above 10^{11} J m^{-3}, from producing large fluxes of particles which can be used to isochorically heat matter, or driving intense shock waves into materials to compress matter to ultra high densities. These new techniques have opened up a huge area of phase space for exploration.

One area of HEDP that has been identified as a significant challenge is the warm

dense matter (WDM) regime. This state is characterised by high pressure (∼1 Mbar), temperature (∼1 eV) and approximately solid density, see Fig. 1.1. It represents a major challenge theoretically, computationally and experimentally as it lies in the regime between traditional solid state and plasma physics, where expansion techniques are no longer applicable, and neither the kinetic nor the potential energy can be treated perturbatively. Strongly coupled ions, non-equilibrium species ($T_e/T_i \neq 1$) and non-negligible electron degeneracy play an important role in defining structural dynamics [78]. Here, T_e and T_i are the electron and ion temperature, respectively. A complete description of the WDM regime is important for describing many physical phenomena ranging from phase transitions within the interior of large astrophysical objects [40] to temperature relaxation rates during the internal processes of inertial confinement fusion (ICF) [127]. In many text books WDM is referred to as a strongly coupled or non-ideal plasma.

1.1.1 Outstanding Questions

Our understanding of these states of matter is rapidly increasing with access to increased computing power and experimental facilities such as free electron lasers(FELs). However, there are still many unanswered questions:

- What is the equation of state of high pressure and temperature systems? What relevance does this have to the formation and evolution of planets? [57]
- On what time-scale is the electron-ion (lattice) equilibration in non-equilibrium matter? [33, 143, 199]
- What is the stopping power of warm dense matter for fast particles? [168]
- What are the transport coefficients in a strongly coupled plasma? [51, 179]
- How does the conductivity change in high pressure and temperature systems? [46, 138]

Answering any of these questions requires a complete understanding of the behaviour of both the electrons and ions within these states of matter. The disparate time-scales associated with both electron and ion dynamics, coupled with being unable to resort to many approximations used in other areas of physics, means the computational cost of answering these questions is often prohibitively high. Solving

these problems from first principles requires solving the Schrodinger equation to obtain the electron-wave functions, but the ion motion necessitates that a huge number of microstates are sampled when calculating thermodynamic properties. Experimentally accessing these high pressure states is difficult as here on earth these states exist only for time-scales of a few nanoseconds before they disassemble; in addition to this they are optically dense meaning experimental diagnosis requires the use of ultra-bright short-pulse high energy X-rays.

1.2 Development of the Field

To help answer these long standing questions associated with materials under extreme conditions it is informative to reviewe briefly the developments that have led up to this point, and in many ways permitted the study presented in this thesis. Here I will present an overview of high power optical lasers[4], short pulse X-ray sources and molecular dynamics, as these are the tools used primarily throughout this thesis to create, probe and simulate these extreme matter conditions. A more detailed description of each of these techniques is given in chapter 2.

1.2.1 Creation: High Power Optical Lasers

The creation of HEDP states of matter here on earth relies on dumping a huge amount of energy into a system within a short time frame. High power optical lasers are the perfect tool for this as they offer flexibility in their use and make large regions of phase space accessible.

The first functional optical laser was developed in 1960 by Theodore H. Maiman [125] and used flash-lamps to pump a ruby crystal emitting light at a wavelength of 694 nm. Also that year the physicists Ali Javan, William R. Bennett, and Donald Herriott constructed the first gas laser that produced light at a wavelength of 1.15 μm from a helium/neon filled cavity [103]. These first lasers had a low average power and were typically either continuous wave or had pulses of the order of milliseconds. However, the importance of lasers to scientific discovery meant that over the next five decades huge advances would be made in the number of attainable wavelengths (developments in gain medium and 3-wave mixing processes) as well as the average and peak powers possible (mode-locking [137], Q-switching [128], CPA [152, 186]). In

[4]The creation of extreme matter states through high power laser-matter interactions is by no means the only method. Alternative schemes relying on diamond anvil cells, gas guns, pulsed power machines and free electron laser irradiation exist, but are outside the scope of this thesis.

particular the development of chirped pulse amplification has led to an increase in peak power of over five orders of magnitude, see Fig. 1.2 [115].

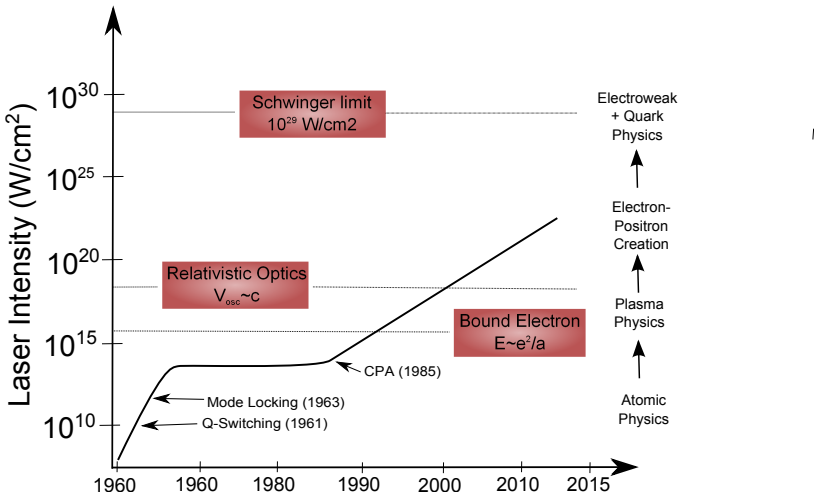

Figure 1.2: History of laser intensity for high power lasers reproduced from Ref. [115]. Important advancements in the history of laser science and the physics areas that can be accessed with increasing intensity are highlighted.

Nowadays laser technology is split into two categories depending on the pulse length, typically either long (∼ns) or short (∼fs-ps) pulses. Both pulse length regimes are useful in the creation of HEDP states. Long pulse lasers with tunable pulse shapes are typically used to ablate the surface of a solid target. The laser light is absorbed by the surface[5] of the target to within a few skin depths generating a high temperature plasma. The plasma expands from the free surface into the vacuum generating a reaction force, this force launches a compression wave into the target while the expanding plasma continues to absorb the laser light up to some critical density. Recent advances in the pulse shaping capability of long pulse lasers has given great precision over the density and temperature states that can be accessed. For example, a slowly increasing intensity (ramp wave) can compress a target along the isentrope, increasing the density of the system while keeping the temperature low. A step like laser profile on the other hand can be used to drive a shock wave with velocities on the order of km/s through solid targets. The shock wave increases both the density and temperature of a system according to relations known as the Hugoniot conditions discussed further in section 2.4.2.

[5]In some situations a second material known as an ablator is deposited on the surface of the target to increase the pressures that can be reached, see section 2.4.2 for more detail.

Short pulse lasers are not often used to compress a target, typically due to the lower energy contained in the pulse[6]. Instead the ultra-high intensities available are more often used to accelerate charged particles (electrons, protons or ions) into solid targets, heating on ultra-short time-scales before hydrodynamic expansion sets in. This isochoric heating of materials gives access to a region of phase space not typically available to long pulse interactions.

Lasers are now routinely used in the laboratory to create high pressure states of matter not accessible through static compression. These states of matter typically exist on nanosecond time-scales and are held together through inertial confinement. That is to say they exist on very short-times scales before huge internal pressures cause them to disassemble. To this end any diagnosis must also take place on these ultra-short time-scales.

1.2.2 Diagnosis: Short Pulse X-rays

On the 8th November 1895 Wilhelm Conrad Röntgen discovered that a screen coated with barium platino-cyanide placed on the one side of his laboratory in Munich would fluoresce when he fired a discharge tube on the other side. He went on to discover that the unknown ray causing this fluorescence could penetrate card and aluminium without attenuation, and even that it could penetrate skin - but not bone [165]. Röntgen was able to deduce that this effect was coming from an unknown type of radiation which he named X-rays[7]. The first X-ray image ever recorded was taken of his wife's hand, see Fig. 1.3. Röntgen received the first ever Nobel prize in physics for his discovery in 1901.

The definition of an X-ray is conventionally the region of the electromagnetic spectrum with a wavelength between $0.01 - 10$ nm, or equivalently an energy between 120 eV and 120 keV [130]. X-rays lie in the region of the electromagnetic spectrum between vacuum ultraviolet (VUV) at lower energies and gamma rays at higher energies, however the boundaries are not strict and a definition based upon the source of the radiation is preferred by some authors[8].

Since their discovery X-rays have been at the heart of many breakthroughs in science, from the determination of crystal structures in 1913 (Bragg and Bragg) [26, 56], the discovery of the double helical nature of DNA in 1953 (Crick, Watson and

[6] Although advances in the energy available within a short pulse laser and the increased precision obtainable means that they are increasingly used as a drive system [131].

[7] Although the term Rötgenstrahlung was used for a while around their discovery.

[8] That is describing radiation emitted from nuclear interaction as gamma rays and radiation from outside the nucleus as X-rays [45].

Figure 1.3: Discoverer of X-rays Wilhelm Röntgen along with the first X-ray photograph showing the hand of his wife, Anna Bertha. Image reproduced from Ref. [92].

Wilkins) [203] to diffraction imaging of biological samples, viruses and proteins [157]. The wavelength of X-rays make them perfectly suited for probing systems where the atoms are spaced a few Ångströms apart, as well as optically dense systems.

Observing transient events such as phase transitions, high pressure shock waves or rapid thermal expansion requires extremely bright pulses of X-rays produced on a time-scale shorter than the response of the system being probed. Modern day X-ray science has focussed in part on this effort, which is in essence taking a snapshot of the atoms in a dynamically evolving system. Since laser-produced shock waves travel at speeds of the order of tens of kilometres per second, and experimental samples are typically tens of micrometers thick, a natural time-scale for the event is of the order of a few nanoseconds. Furthermore, the speed of shock waves produced from laser-solid interactions means that any such X-ray source must be synchronised to an event, not least because the sample is usually destroyed by the intense laser irradiation [90].

The earliest efforts towards this goal of diffraction from a short X-ray pulse was the creation of a millisecond X-ray source by Tsukermann and Avdeenko in 1942 [191, 201]. By utilising a pulsed X-ray tube they managed to obtain diffraction patterns from single crystal aluminium samples. A year later Al'tshuler used similar techniques to produce diffraction patterns from steel samples with a time resolution of below 10 μs [9, 92]. However, the brightness of the X-ray sources meant only static diffraction patterns were possible at the time.

Over the resulting decades pulsed X-ray sources become become steadily brighter

and radiography of shocked materials become common place. However, in 1969 the brightness of X-ray sources had increased enough such that Johnson was able to record the first diffraction pattern from a shocked solid [104]. The development of short pulse radiation sources would then diverge into two different technologies both of which are used in the experimental work discussed here. The first method revolves around using a high intensity optical or near-optical laser to drive electrons into metal targets releasing characteristic X-ray radiation, bremsstrahlung radiation or thermal radiation. The second technique revolves around using conventional accelerator technology to drive high intensity electron beams into a metal target or later, an undulator, to produce synchrotron radiation.

1.2.2.1 Laser Produced X-rays

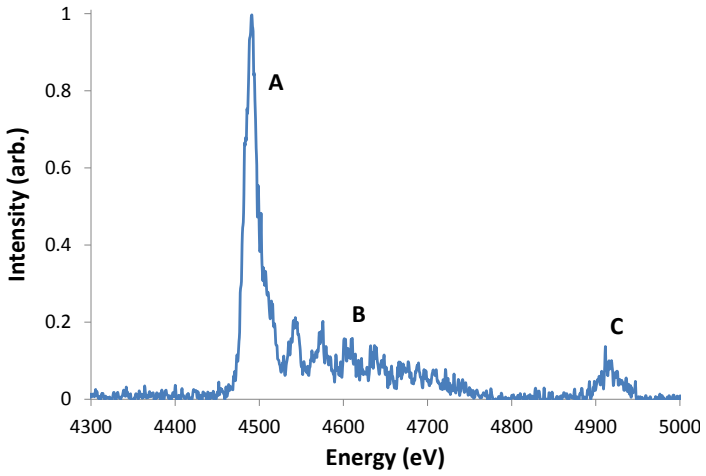

Figure 1.4: Typical spectrum of a K_α source taken from short-pulse (40 mJ, 40 fs) laser irradiation of a thin (10 μm) Ti foil. The spectrum was recorded using a HOPG crystal analyser with a CCD placed equal distance away. Energy calibration was carried out using the known energies of the K_α (A) and K_β lines (C). Satellites arising from additional ionisation levels can also be seen, marked (B).

As detailed in section 1.2.1 the development of high powered lasers led to the ability to create high pressure and temperature states of matter for very short periods of time in the laboratory. However, the interaction of an intense pulse of optical or near-optical radiation with matter can also act as a source of X-ray radiation that can be used to probe the target. Typically the interaction of a long pulse laser with an intensity of around $10^{15} - 10^{16}$ W cm^{-2} with a solid density target creates a hot plasma in a highly ionised state with many He-like ions. These He-like ions emit

radiation from the 2p-1s transition with high efficiency (0.1% conversion of optical light into X-rays) yielding around 10^{11} photons per joule in modern experiments. This type of X-ray source has been used as a back-lighter to study laser driven shocks for the past decade but suffers due to relatively long pulse length and a large bandwidth, typically of the order of 10^{-2}. Additionally, the energy spectrum is not smooth, containing features from different orbital transitions as well as satellite lines.

The interaction of a short-pulse laser with a thin foil excites fundamentally different physical processes in the target. The radiation drives an intense beam of electrons travelling at relativistic speeds into the target. As these electrons pass through the target collisional excitation leaves vacancies in the inner shell and electrons from higher orbitals drop down an energy level to fill the shell emitting characteristic K_α radiation [59, 176]. This line radiation typically has a pulse length of the order of the laser pulse length and a much cleaner spectrum than that of the He-α source. The down side is that the conversion efficiency is of the order of 10^{-4}, coupled with the reduced energy in short-pulse laser systems, makes using this radiation source a challenge. However, before the advent of forth generation light sources optical laser produced X-rays were one of the prevailing technologies used to capture the behaviour of ultra-fast events in dense materials. Alternative methods to observe events occuring on a sub-picosecond timescale utilised X-ray streak camera technology, developed in the 1970s [61, 121, 129, 141].

1.2.2.2 Free Electron Lasers

Another method of short pulse X-ray production is based on accelerator technology. Among the first of these was the PHERMEX linear accelerator which sent a short electron bunch into a tungsten target producing bremsstrahlung radiation in the soft X-ray regime [184]. The development of accelerator based light sources is generally split into generations, with the first generation generally being machines traditionally used for particle or nuclear physics modified, or adapted to a light source. The second and third generation light sources utilised synchrotron and wiggler radiation to produce harder radiation. Finally, there are fourth generation light sources where a high intensity X-ray beam is passed through an undulator to produce an ultra-short coherent X-ray beam[9].

[9] As part of efforts to develop the fourth generation light source at Stanford an accelerator-based X-ray source, the Sub-Picosecond Pulse Source (SPPS), based on linac acceleration and electron bunch compression schemes was able to produce 80 fs pulses which were succesfully used to observe ultra-fast transient phenomena [122]

One important measure of the quality of a light source is the brilliance. The brilliance of a source is a measure of the number of photons per second, per angular divergence, per cross sectional area, per 0.1% bandwidth. In general the greater the brilliance the more photons that can be concentrated on a single spot in a set amount of time. Fig. 1.5 plots the change in brilliance of X-ray sources over the last century. The most brilliant X-ray sources on the planet are FELs.

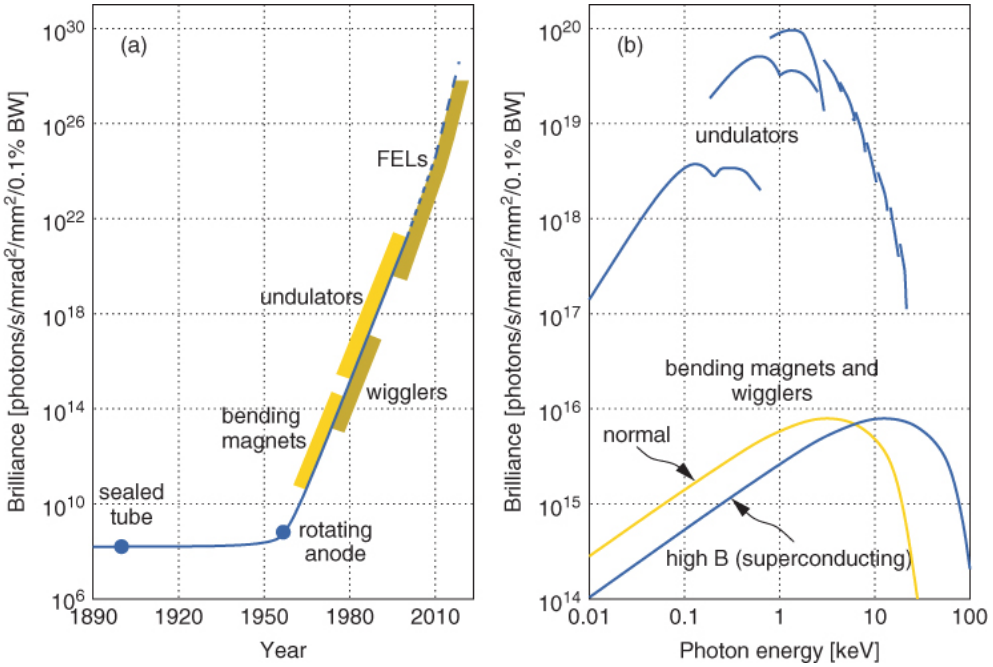

Figure 1.5: Comparative brilliance of third and fourth generation light sources, reproduced from Ref. [211].

A FEL works by passing a beam of electrons accelerated to relativistic energies through an alternating transverse magnetic field, called an undulator. If the undulator period λ_0, radiation wavelength λ, and electron beam velocity $c\beta$ are matched according to $\lambda \approx \lambda_0(1-\beta)/\beta$, where c is the speed of light then resonance is achieved and efficient exchange of energy between the electrons and magnetic field takes place.

With the advent of fourth generation light sources based on free-electron laser technology, experiments that require extremely high photon flux become possible. Chapter 5 outlines a ground breaking experiment where the ultra-high brilliance of the linac coherent light source (LCLS) is exploited to measure the low frequency ion waves in dense plasma. A detailed description of the LCLS, including the new low bandwidth self-seeding mode, can be found in section 5.1.

1.2.3 Simulation: Molecular Dynamics

The primary simulation technique used throughout this thesis is molecular dynamics (MD). Molecular dynamics is a technique that is able to model the detailed microscopic dynamics of the ions in a gas, liquid, solid or even a plasma. Classical MD revolves around solving numerically the Newtonian equations of motion, $F = m\ddot{x}$, for a particular ensemble of atoms to obtain the time evolution of the many-body dynamics. This deceivingly simple technique developed in the 1950s by Alder and Wainwright is extremely powerful and can be used to investigate systems in chemistry, physics and biology [3]. It can be used to calculate dynamic properties of an evolving system, as well as to sample from particular statistical ensembles as a means to determine equilibrium thermodynamic properties such as temperature and pressure. A huge advantage of this technique is that if a system displays the correct macroscopic properties, for example the output could be matched to an experimental result, then the simulation can be interrogated at a microscopic level not always possible experimentally. These simulations provide an important link between the micro physics describing the exact ion-ion interactions and the macro physics - for example the temperature and pressure.

The very first MD simulations were performed in the 1950s by Alder and Wainwright [3, 4] and were used to study the interaction of systems of hard spheres. Although this provided many insights into the behaviour of liquids, the development of more accurate potentials was required to simulate more complex physical systems. This was achieved in 1960 when the Vineyard group simulated the radiation damage of a copper crystal [69] and in 1964 when Rahman simulated liquid argon using a potential developed from the van der Waals interaction [160]. Since then the development of more accurate potentials and the parallelisation of MD algorithms has led to larger spatial and temporal simulations being performed with increased physical accuracy. In classical MD it is now routinely possible to simulate systems with over 1 million atoms on a small cluster of a few tens of CPUs [108]. Indeed, this is done in section 3.5 where a thin 200 nm gold foil reaching temperatures of just a few hundred Kelvin is modelled completely in one dimension. However, when studying HEDP states it is not always possible to find a suitable potential which can model the ion-ion interactions over large temperature and density scales. As such quantum molecular dynamics where the potential can be calculated for each condition and on each time-step in a simulation represent a significant improvement over classical models. However, this typically limits the number of atoms it is possible to simulate to less than 10^3. Hence this technique is typically used in quantum chemistry, where

molecules are simulated, or in condensed matter where the periodicity of the problem allows the complexity of the problem to be reduced. The simulation of HEDP states in this work uses an orbital-free technique, which acts as a middle ground between the classical and full quantum descriptions, and is described in chapter 4.

1.3 Structure of the Thesis

This section will briefly outline the structure of this thesis.

Chapter 2 begins by reproducing some of the fundamental theoretical concepts that underpin the work in this thesis. The topics discussed include basic crystallography, X-ray scattering from solids and plasmas, classical molecular dynamics and laser-solid interactions.

Chapter 3 outlines the problem of temperature relaxation in non-equilibrium plasmas, a problem identified as an outstanding question in this area of research, see section 1.1.1, and crucially is relevant to the creation of HEDP states in the laboratory. Details of three different experiments each designed to measure the time-scale of electron-ion equilibration will be presented. Each experiment uses time-resolved X-ray diffraction to measure the structural dynamics of the ions and infer the ion temperature, but in each case a different heating mechanism was used (high intensity proton beam, high intensity electron beam and direct laser illumination). The results show the need for an increased understanding of the electron-ion coupling in extreme matter states and highlights that many experiments investigating high pressure EOS may not in fact be in local thermodynamic equilibrium as previously assumed.

Chapter 4 concentrates on the application of a theoretical technique based around density functional theory to enable the extraction of both thermodynamic properties and structural dynamics of HEDP states of matter. In this section the process of creating suitable pseuodpotentials necessary for a quantum MD simulation is discussed thoroughly along with the validity of this approach. The computational speed up offered by this approach is exploited to allow self-consistent quantum calculations of the dynamic ion-ion structure factors for the first time. Classical simulations are compared with the quantum molecular dynamics simulations and the differences discussed.

Chapter 5 presents a ground breaking proof-of-principle experiment performed at the LCLS to directly measure the ion-ion fluctuations in a dense plasma. Time resolved X-ray scattering from laser shock produced HEDP states are spectrally resolved to observe the ion feature which can be compared directly with the dynamic

ion-ion structure factor presented in chapter 4. The comparison between experiment and theory shows that the sound speed and acoustic peak position is captured accurately in the simulations while the entropy (central) peak shows discrepancies. A separate analysis technique revolving around a hydrodynamic description of a dense plasma is also discussed briefly and shown to be a powerful method to describe the data, and to extract thermodynamic and transport properties.

Chapter 6 contains an overview of the thesis, and the work performed. Finally, a short insight into the direction this work could take in the future is included.

Chapter 2

Elementary Theory

This chapter will cover some of the elementary theory relevant for understanding the work presented in this thesis. Ideas presented here can be found in many textbooks but is presented here for reference. In addition, it is hoped that the necessary difficulty of alternative nomenclature present when working in a multidisciplinary field is lessened when similar ideas are presented side-by-side.

2.1 States and Phases of Matter

There exist many different states[1] of matter in our universe. Solids, liquids and gases are the most common and we come into contact with these on a daily basis, but more exotic states of matter exist, such as plasmas or Bose-Einstein condensates, and are often highly studied due to their unique properties and prevalence in astrophysical environments. This thesis is about the creation and study of extreme states of matter, i.e. those states which are rarely found here on earth but must be created in the laboratory in order to be studied up close. In particular it is concerned with the study of WDM, a state that lies in the transition regime between solids, liquids and plasmas and has characteristics associated with all three. Experimental and theoretical work surrounding WDM requires techniques and theories from each discipline. It is therefore useful to cover some basic theory from condensed matter and plasma physics to provide a framework for this thesis.

[1] Although the word phase is often used interchangeably with state this should be avoided as within a particular state there are often multiple phases of matter, e.g. liquid-liquid phase transitions within hot dense hydrogen or the solid-solid ($\alpha - \epsilon$) phase transition during shock compressed iron [92].

2.1.1 Solids, Liquids and Gases

A solid can be defined as a rigid structure in which the atoms are tightly bound, that is the atoms do not contain enough kinetic energy to move significantly from their equilibrium positions. Often the most energetically favourable structure is for the atoms to arrange themselves into a regular periodic structure, a crystal. This long range order is a characteristic property associated with many solids. A crystal is described mathematically first by defining a lattice made up of a linear superposition of N independent basis vectors, where N is the dimension of the crystal. For a 3-dimensional crystal the position of the lattice points in real space can then be expressed as -

$$L(\mathbf{r}) = \sum_{u=-\infty}^{\infty} \sum_{v=-\infty}^{\infty} \sum_{w=-\infty}^{\infty} \delta(\mathbf{r} - u\mathbf{a} - v\mathbf{b} - w\mathbf{c}) \,, \tag{2.1}$$

where $\mathbf{a}$, $\mathbf{b}$ and $\mathbf{c}$ are the basis vectors and u, v and w integers that act as indices for the atoms.

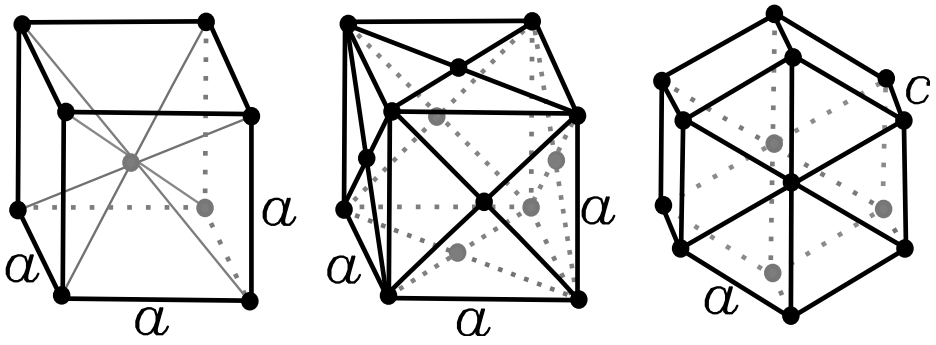

Figure 2.1: Three examples of the 14 Bravais lattices. From left to right are the body-centred-cubic (BCC), the face-centred cubic (FCC) and the simple hexagonal lattices. The letters a and c are the lengths of the unit cells.

Every lattice point is equivalent and the system of points displays translational symmetry along each of the basis vectors. To turn this description of a lattice into a description of a real crystal we define a basis set. A basis set is a set of N vectors which describe the position of the atoms in relation to each lattice point. The simplest basis set is to place a single atom at each lattice point (i.e. the basis set would consist of a single vector of length $\mathbf{0}$), in this situation each atom is equivalent and the number of crystal structures is limited by translational symmetry. It has been shown that in this case only 14 lattices, called Bravais lattices, can be defined. This includes the three common crystal structures, the crystal structure of iron known as body-centred

cubic (BCC), the structure of aluminium known as face-centred cubic (FCC), and a hexagonal crystal structure, hexagonal close packed (HCP), all shown in Fig. 2.1. The volume defined by the vectors **a**, **b** and **c** creates a unit cell which when tessellated fills all space and fully defines the crystal. There exists an unlimited number of unit cells for each crystal structure, however, in practice two are generally used. The conventional unit cell which most easily describes the full symmetry of the crystal and the primitive unit cell which is the smallest possible volume that can describe the crystal. For example, the conventional unit cell of an FCC structure contains 4 atoms and has a cubic unit cell while the primitive unit cell contains a single atom and is rhomboidal in shape. More complex crystal structures require a multi-atom basis, graphite for example has the HCP lattice shown in Fig. 2.1 but requires a four atom basis. The basis vectors place atoms at locations (0,0,0), (0,0,$\frac{c}{2}$), $\frac{a}{2}$($\frac{1}{\sqrt{(3)}}$,1,0) and ($\frac{-1}{2\sqrt{3}}$,$\frac{-a}{2}$,$\frac{c}{2}$). The resulting crystal is shown in Fig. 2.2. In a HCP lattice the vectors **a** and **b** are at 120° to each other and equal in length, they map out the basal plane, while the c-axis represented by **c** is perpendicular to both.

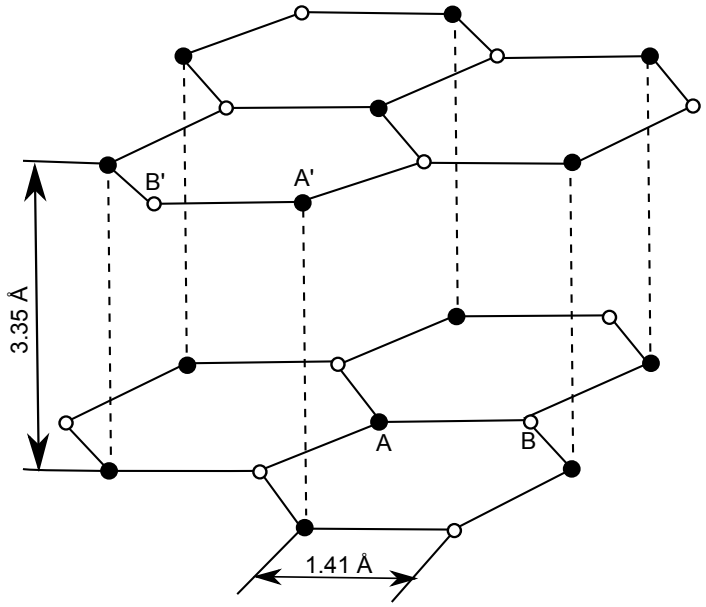

Figure 2.2: Graphite crystal structure showing the four atoms in the unit cell (A, B, A', B').

As the temperature of a system is increased, at some point, the thermal energy of the atoms becomes high enough to overcome the potential barrier binding the atoms together, and the long range order vanishes. Typically, liquids retain a short-range order while gaseous systems are characterised by complete disorder. The radial distribution function (RDF) can be used to quantify the level of disorder present in

a system. It is defined by writing the average number of atoms, $\delta N(r)$, in a spherical shell of radius r and thickness δr around any given reference ion as,

$$\delta N(r) = 4\pi n \int_{r}^{r+\delta r} r^2 g(r) dr \,, \tag{2.2}$$

where n is the average ion density and $g(r)$ the RDF. For $g(r) = 1$ which is the case for an ideal gas, characterised by complete disorder, the expression reduces to $\delta N \approx n \times V_{shell}$ where V_{shell} is the volume of the shell. If there is either short or long range order in the system then the RDF is non-trivial and for solids can also have directional dependence where g depends on vector $\mathbf{r}$. For a solid at T=0 K the RDF would be a sum of delta functions located at the lattice sites while for an isotropic liquid the RDF can be averaged spherically. Fig. 2.3 shows the loss of structure in the RDF of solid density aluminium as the temperature is increased from 0.2 to 20 eV. The RDFs were were calculated from 32 atom orbital-free DFT calculations run for 1 ps in 1 fs steps. Full calculation details are given in chapter 4. The peaks in the function represent shells of atoms located around the reference atoms, the first peak is often located at the nearest-neighbour distance. For all liquids the long range behaviour is to tend to unity due to to the absence of long range order.

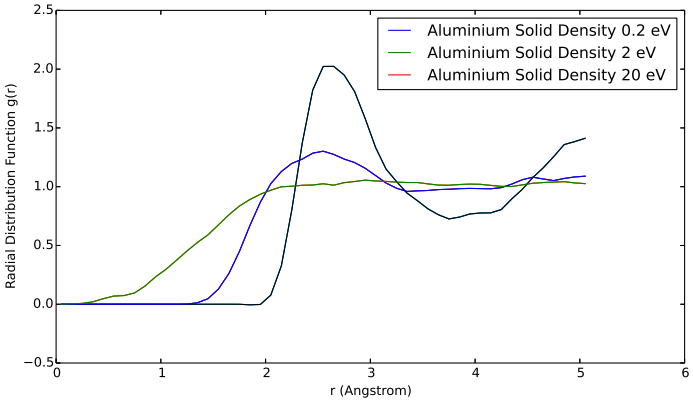

Figure 2.3: Radial distribution function of solid density aluminium at 0.2, 2 and 20 eV. RDFs were calculated from 32 atom orbital-free DFT calculations run for 1 ps in 1 fs steps. Full calculation details are given in chapter 4.

2.1.2 Non-Ideal Plasmas

A plasma is defined as a quasi-neutral system of charged particles. It is the natural state of matter at high temperatures where the electrons in the system have enough

energy to become ionised. This partially ionised system presents difficulties over, for example, an ideal gas as the electromagnetic fields from the ions create a collective many-body system. Classical plasma physics is focussed on high temperature, low density systems. Here the ions are treated as point particles and ion-ion interactions are considered weak or neglected completely. Non-ideal plasmas, such as WDM are characterised by strong ion-ion correlations and the presence of short range order, such as that commonly associated with a liquid. It is this short range order (or in some special conditions long range order[2]) which can considerably alter the physics and renders much of the classical statistics-based plasma physics techniques unsuitable.

An example where electron-ion interactions play an important role in determining the behaviour of a physical system is charge screening. First developed by Debye and Huckel in 1923 for electrolyte solutions the idea of charge screening has become a ubiquitous tool in describing non-ideal plasmas [43]. The idea is that the Coulomb field surrounding a positive ion in a plasma is screened by the negatively charged electrons which it attracts. Classically, by considering the distribution of free electrons surrounding an ion the screening length can be shown to be,

$$\lambda_D = \sqrt{\frac{\epsilon_0 k_B T_e}{e^2 Z^2 n}}\,, \tag{2.3}$$

where k_b is the Boltzmann constant, T_e the electron temperature, Z the average ionisation state and n the ion number density. The Debye length then defines a region around the ion known as the Debye sphere where the Coulomb interaction is screened and the potential can be written in the form,

$$V(r) = \frac{e}{4\pi\epsilon_0 r} e^{-r/\lambda_D}\,, \tag{2.4}$$

this is the screened Coulomb potential, or the Yukawa potential.

The number of electrons contained in the Debye sphere surrounding an atom is given by $N_D = 4/3\pi n\lambda_D^3$. For a typical ideal plasma with an ion density of $n \sim 10^{14}$ cm^{-3} and a temperature of around 8 keV this number is of the order of 10^8. However, for the types of systems considered here this is often not the case. The centre of Jupiter which is thought to consist of a Hydrogen plasma with a density of $n \sim 10^{24}$ cm^{-3} and a temperature of around 1 keV we find that this number comes out as 10^{-3} demonstrating that for such non-idea plasmas the statistical approach to the concept of screening as given by the Debye length is not appropriate. Although

[2]It is possible to have a high temperature/pressure system where the ions form a crystalline lattice. In fact it is believed that the centre of the earth is crystalline in nature [126].

the concept of screening from plasma physics has been shown to be inapplicable in the regimes studied here, the idea of screening is one that is still useful in HEDP states of matter. Alternative screening concepts based on the Thomas-Fermi screening length are routinely used in high pressure systems where the electron degeneracy is high and screening plays an important role in electron-ion coupling (see section 4 on developing potentials for use in both classical and quantum simulations).

A second concept from plasma physics which is used in this work is that of plasma frequency. This is the frequency of characteristic oscillations associated with the electrons (or ions) in an ionised system. Since this work is focussed on the ion dynamics in a dense plasma the useful quantity is the ion plasma frequency. This is given by,

$$\omega_p = \sqrt{\frac{n(Ze)^2}{\epsilon_0 m}}\,. \tag{2.5}$$

The inverse of this frequency dictates the typical time-scale during which ion motion occurs. The electron plasma frequency is obtained by replacing the ion charge (Ze) with the electron charge and the ion mass (m) with the electron mass. The electron plasma frequency is not discussed in this work but plays a crucial role in dictating the absorption of electromagnetic radiation into a target. Radiation with a frequency lower than the plasma frequency cannot penetrate further into the target and this defines a critical density ($n_e = \omega\epsilon_0 m_e/e^2$) above which radiation is reflected from the surface. The plasmas studied in this work all fall into this optically *over-dense* category emphasising further the need for X-ray diagnostics.

Beyond classical plasma physics a few parameters have been defined specifically for the study of WDM. One of these parameters is the ion-ion coupling parameter. The ion-ion coupling parameter is defined by,

$$\Gamma = \frac{(Ze)^2}{4\pi\epsilon_0 k_B T_i a} \tag{2.6}$$

where $a = 3/(4\pi n)^{\frac{1}{3}}$, is the Wigner-Seitz radius (average inter-particle separation). Eq. (2.6) expresses the ratio of the pairwise Coulomb interaction to the average kinetic energy. An exact definition of WDM is difficult as it encompasses a huge area of phase space where other theories break down, however it is reasonable to assert that WDM is defined by the region where the coupling parameter is of order unity or greater.

- When ($\Gamma << 1$) the kinetic energy of the ions is the dominant term and the system can be treated as an 'ideal' plasma. It is within this regime that kinetic theory and hydrodynamics are most applicable.

- A value of order unity represents a system where the Coulomb interaction becomes non-negligible and correlations between particles must be incorporated into any theory. This typically defines the WDM regime discussed throughout this work.

- At ($\Gamma >> 1$) the influence of the Coulomb interaction is greater than the kinetic energy and the ions arrange themselves around their equilibrium lattice positions. In this crystalline phase the ions oscillate around the equilibrium lattice positions. For a pairwise Coulomb system the phase transition occurs at $\Gamma = 171.8$ increasing with additional screening effects [83].

A second important quantity relevant to the study of WDM is related to the degeneracy of the system. As the density of the plasma is increased further the inter-particle separation becomes comparable to the DeBroglie wavelength of the electrons,

$$\Lambda_e = \frac{h}{\sqrt{2\pi m_e k_b T_e}} \,. \tag{2.7}$$

At this point the electrons no longer follow Maxwell-Boltzmann statistics (another reason the Debye screening is no longer applicable in dense plasma states) but have a Fermi-Dirac distribution. The highest occupied energy level in a fully degenerate system (T_e=0 K) is given by the Fermi energy,

$$E_F = \frac{\pi^2 \hbar^2}{2m_e} \left(\frac{3n_e}{\pi} \right)^{\frac{2}{3}} \,, \tag{2.8}$$

which gives a characteristic temperature of the electron system as $T_f = E_F/k_B$. The final important parameter in characterising WDM is then the degeneracy parameter defined as,

$$\Theta = \frac{k_B T_e}{E_F} \,. \tag{2.9}$$

When this parameter is small the electrons are in a degenerate state and quantum statistics play a crucial role in their description. In particular, if the electrons are in lower energy states the Pauli exclusion principle becomes important, and in crystalline materials Bloch waves are set-up altering the material characteristics dramatically. At higher Θ thermal effects increase and the electrons can be considered to behave as classical point-like particles. There are other parameters that describe the conditions

of a dense plasma, such as the importance of relativistic effects, but at the electron temperatures considered here they can be considered non-relativistic [99, 100].

In a fully degenerate plasma the Debye screening length is replaced with the Thomas-Fermi screening length given by,

$$\lambda_{TF} = \sqrt{\frac{2\epsilon_0 E_F}{3Zn_e^2}}. \tag{2.10}$$

For conditions considered for most WDM states the limiting cases of the Debye screening length and Thomas-Fermi screening length are not appropriate. Some models have been proposed which interpolate between these two extremes. One particularly successful example is that of an electron gas at arbitrary degeneracy which has been shown to yield results with less than 2% error for all densities [67].

2.1.3 Correlation Functions

From a theoretical point of view the physics behind the many-body correlations present in a strongly coupled system is studied through the use of distribution functions [86, 133]. The short-range order present in the systems studied here can be characterised by the *density-density correlation function*. A correlation function is used to assess if there is a statistical correlation between one or more functions at multiple points, often spatially or temporally separated. A time dependent correlation function is generally defined as,

$$G_{AB} = \langle A(\mathbf{r_1}(t), \mathbf{r_2}(t)...\mathbf{r_N}(t))^* B(\mathbf{r_1}(0), \mathbf{r_2}(0)...\mathbf{r_N}(0))\rangle_T, \tag{2.11}$$

where A and B are dynamical variables. In this case they are variables which depend on the position of the particles in the system, but in principle can depend on other quantities such as the particle momenta[3]. The angle brackets $\langle ...\rangle_T$ in the correlation function denote an ensemble average at temperature T, that is an average weighted by the partition function for a system in thermodynamic equilibrium. Details of the ensemble average is given in section 2.3.1, which deals with calculating these functions from MD simulations. This thesis will only be concerned with calculating autocorrelation functions, that is functions where the dynamical variables A and B are the same. One such variable is the microscopic density of the system.

[3]The velocity autocorrelation function or current correlation functions are examples correlation functions that depend on variables other that the particle positions.

Following the derivation by Baiko *et al.* [15] we begin by defining $\hat{\mathbf{r}}_i$ as the position operator of the ith atom. The Heisenberg operator of the microscopic density is then given by,

$$\hat{\rho}(\mathbf{r}, t) = \sum_{i=1}^{N} \delta(\mathbf{r} - \hat{\mathbf{r}}_i(t)) \,. \tag{2.12}$$

From the real space microscopic density, the correlations between the density at two points in space and time can be defined through the dynamic density-density autocorrelation function, also known as the van Hove function,

$$G(\mathbf{r}, \mathbf{r}', t) = \frac{1}{N} \langle \hat{\rho}(\mathbf{r}' + \mathbf{r}, t) \hat{\rho}(\mathbf{r}', 0) \rangle_T \,. \tag{2.13}$$

For a translationally invariant system the van Hove function can be integrated over $\mathbf{r}'$ removing the dependence on the choice of origin,

$$G(\mathbf{r}) = \frac{1}{N} \left\langle \int \rho(\mathbf{r} + \mathbf{r}', \mathbf{t}) \rho(\mathbf{r}, \mathbf{0}) d\mathbf{r}' \right\rangle_T = \frac{1}{N} \langle \sum_{i=1}^{N} \sum_{j=1}^{N} \delta(\mathbf{r} - \mathbf{r}_i(t) + \mathbf{r}_j(0)) \rangle_T \,. \tag{2.14}$$

The density-density correlation function can then be split into two terms. The first term is the self-correlation and represents a particle's correlation with itself, while the second term is the pair distribution function and represents the correlation between two particles in the system,

$$G(\mathbf{r}, t) = G_s(\mathbf{r}, t) + G_p(\mathbf{r}, t) \,, \tag{2.15}$$

with,

$$G_s(\mathbf{r}, t) = \frac{1}{N} \langle \sum_{i=1}^{N} \delta(\mathbf{r} - \hat{\mathbf{r}}_i(t) + \hat{\mathbf{r}}_i(0)) \rangle_T \,, \tag{2.16}$$

$$G_p(\mathbf{r}, t) = \frac{1}{N} \langle \sum_{i \neq j}^{N} \delta(\mathbf{r} - \hat{\mathbf{r}}_i(t) + \hat{\mathbf{r}}_j(0)) \rangle_T \,. \tag{2.17}$$

For the static case (t=0) the above expression simplifies to,

$$G(\mathbf{r}, 0) = \delta(\mathbf{r}) + \rho g(\mathbf{r}) \,. \tag{2.18}$$

In the time-independent case the self correlation term is the probability of finding the same particle at position $\mathbf{r}$ away from its initial location, this reduces to a delta function. The pair correlation term, $g(\mathbf{r})$, represents the probability of finding a

different particle a distance of $\mathbf{r}$ away given that there is a particle at the origin, this is just the RDF, $g(\mathbf{r})$, introduced in section 2.1.1. The van Hove function can be thought of as a time-dependent RDF.

The RDF plays an important role as many thermodynamic properties can be written as an integral over $g(r)$. The average potential energy of a system, a quantity that is important in describing the EOS, can be obtained by integrating the potential energy multiplied by the mean number of particles in a shell of thickness δr from $r = 0$ to $r = \infty$. That is, the excess internal energy of a system can be written as,

$$U^{ex} = 2\pi N n \int_0^\infty r^2 v(r) g(r) dr \,, \tag{2.19}$$

where we have divided the result by two to prevent double counting. The total internal energy of a system can then be found by adding the internal energy of the ideal gas ($U_0 = 3/2 N k_b T$) to this excess energy.

The pressure associated with the system can then be written in terms of the excess energy according to,

$$P = P_0 \left(1 + \frac{1}{2} \frac{U - U_0}{U_0} \right) , \tag{2.20}$$

where $P_0 = n k_B T$ is the pressure of the idea gas. From these relations further thermodynamic relations such as the heat capacity or compressibility can be derived through the usual thermodynamic relations [133].

The real space auto-correlation functions are in a way very intuitive, that is they can be expressed as the probability of finding a particle at some particular distance and time away from another particle. However, in a homogeneous system, the Fourier transform of these functions can provide a much greater wealth of information.

The intermediate scattering function (ISF) is defined as the spatial Fourier transform of the van Hove function,

$$F(\mathbf{k}, t) = \int_{-\infty}^{\infty} G(\mathbf{r}, t) e^{-i\mathbf{k}.\mathbf{r}} \, \mathrm{d}\mathbf{r} = \frac{1}{N} \langle \hat{\rho}(\mathbf{k}, 0) \hat{\rho}(-\mathbf{k}, t) \rangle_T \tag{2.21}$$

where,

$$\hat{\rho}(\mathbf{k}, t) = \sum_{i=1}^{N} e^{-i\mathbf{k}.\hat{\mathbf{r}}_i(t)}. \tag{2.22}$$

In the case of an isotropic system (such as a liquid, gas or plasma) the value of these functions depend only on the magnitude of $\mathbf{k}$ and hence the ISF will be denoted

$F(k,t)$ where appropriate. The temporal Fourier transform of the ISF is a quantity called the dynamic structure factor (DSF),

$$S(\mathbf{k},\omega) = \frac{1}{2\pi}\int_{-\infty}^{\infty} F(\mathbf{k},t)e^{-i\omega t}\,\mathrm{d}t\,. \tag{2.23}$$

This is a quantity which describes both temporal and spatial correlations present in the density fluctuations in a system. It is important theoretically as it can be related to the density response function through the fluctuation-dissipation theorem,

$$S(\mathbf{k},\omega) = -\frac{k_B T}{\pi n\omega}\Im m[\chi((k),\omega)]\,, \tag{2.24}$$

and is a quantity which can be measured directly through X-ray scattering measurements discussed in section 2.2.

The integral of Eq. (2.23) is a quantity known as the static structure factor (SSF),

$$S(\mathbf{k}) = \int_{-\infty}^{\infty} S(\mathbf{k},\omega)\,\mathrm{d}\omega = 1 + n\int e^{-i\mathbf{k}\cdot\mathbf{r}}g(\mathbf{r})d\mathbf{r}\,, \tag{2.25}$$

which as one would expect for the reciprocal correlation function of a static system is related to the Fourier transform of the RDF. The SSF is a quantity which like the DSF can be measured through the X-ray scattering techniques discussed in section 2.2. Fig. 2.4 shows a comparison between the RDF and the DSF for a copper lattice. It is informative to notice how the peaks broaden with temperature in the RDF but not in the Fourier space SSF.

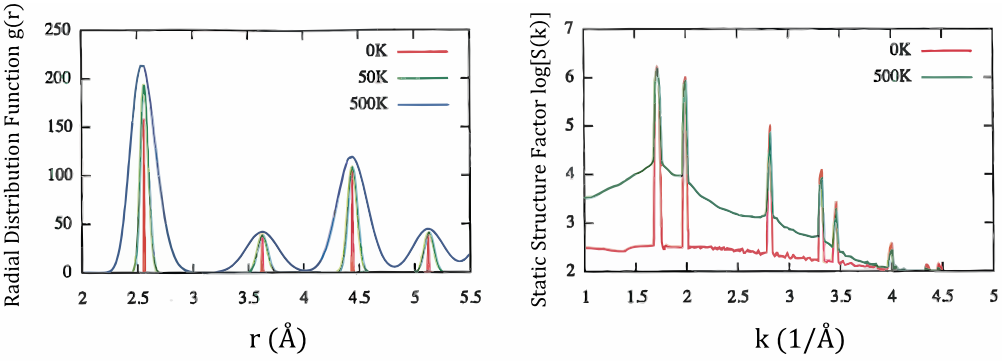

Figure 2.4: Comparison between the static structure factor and radial distribution function for a 500 000 atom MD simulation of Cu arranged in an fcc lattice with periodic boundary conditions. The RDFs have been scaled to demonstrate the change with temperature, while the structure factors have been plotted on a log scale. This figure was adapted from [108].

2.1.3.1 Correlation Functions in Solids and Plasmas

In the previous section correlation functions have be discussed without much thought as to what particles the microscopic density function represents. For example, the equations in the previous section are all perfectly valid if we are discussing electron density as they are when discussing ions. Since this report is focussed on describing the strong correlation between the ions in a dense plasma system, we will assume from this point that the density function represents the ions in the plasma.

Fig. 2.5 shows some computed static ion-ion structure factors for various ion temperatures in graphite. In the high temperature regime the structure factor tends towards unity for all values of k. This is the limit for a high temperature non-interacting gas where there are no correlations between the particles. At lower temperatures more structure appears and the liquid correlation peak ($k/k_{Bragg} \approx 0.7$) grows as the correlations in the more strongly coupled plasma appear. At lower temperatures or conversely higher ion-ion coupling parameters the influence of the Coulomb interaction is increased and the ions arrange themselves around their equilibrium lattice positions. In graphite this gives rise to the lattice planes and, as can be seen from Fig. 2.5, a delta-like peak appears at $k = k_{Bragg}$ where $k_{Bragg} = 2\pi/d$ and d is the inter-plane separation.

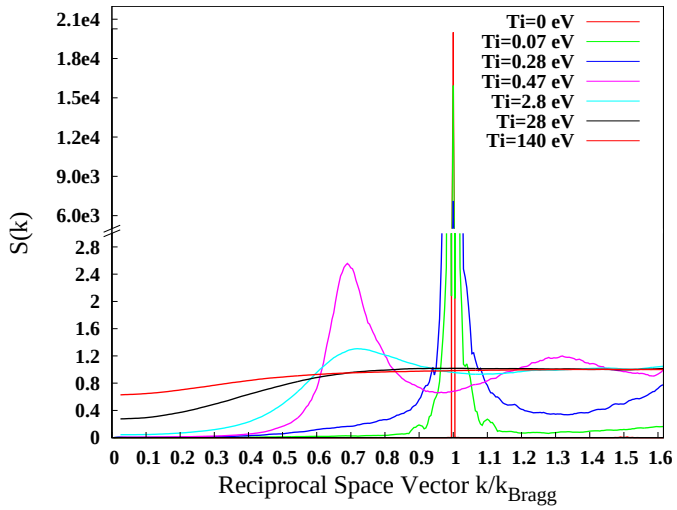

Figure 2.5: Ion-ion static structure factor for graphite where k is aligned perpendicular to the planes. Obtained from molecular dynamics simulations performed with LAMMPS (see section 2.3).

The origin of this peak is most easily understood by treating graphite as an infinite perfect crystal, which in a single lattice direction can be represented by a Dirac comb of separation d. The Fourier transform of this Dirac comb is another Dirac comb with

separation $2\pi/d$. This gives rise to the peaks in the SSF of a solid. It will be shown in the next section that the peaks in the SSF lead to X-ray scattering only when the condition $2d\sin(\theta_s/2) = n\lambda$ is satisfied.

2.2 X-ray Scattering

X-rays typically have energies of a few keV and a wavelength of the order of a few Ångstöms, this length scale is comparable to the inter-particle distance in solids, liquids and dense plasmas and hence makes them an ideal candidate for probing these states of matter[4].

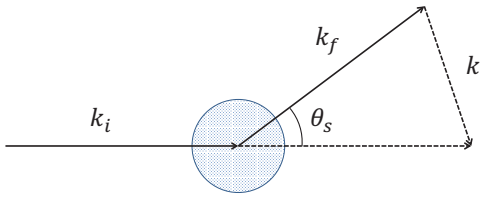

Figure 2.6: Schematic showing the typical set-up for an X-ray scattering experiment.

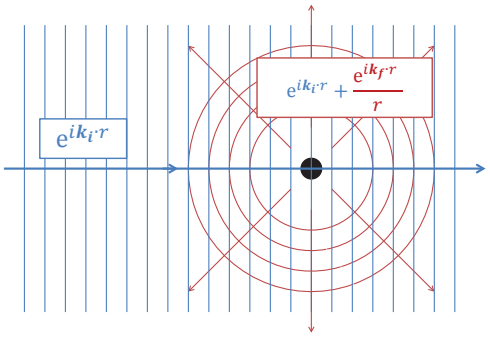

Figure 2.7: Scattering of a plane wave from a single potential or atom.

This section will outline some of the basic theory associated with X-ray scattering which is essential to understanding the experimental techniques discussed in the later sections. A schematic of a general scattering experiment is shown in Fig. 2.6. An incident beam of photons with energy E_i and wave-vector $\mathbf{k_i}$ intercepts a sample and is scattered by an angle θ_s into a new beam with energy E_f and wave-vector $\mathbf{k_f}$ [30]. The energy and momentum transfer from the scattering process is given by,

$$E = \hbar\omega = E_i - E_f \qquad \hbar\mathbf{k} = \hbar\left(\mathbf{k_i} - \mathbf{k_f}\right). \tag{2.26}$$

In the non-relativistic limit where the energy transfer is less than the photon energy as will be considered throughout this work the momentum transfer is simply related to the scattering angle by,

[4]Thermal neutrons are also often used to probe the structure of solid density matter having a typical wavelength of ∼1 Å.

$$\hbar\mathbf{k} = 2\mathbf{k_i}\sin\left(\frac{\theta_s}{2}\right). \tag{2.27}$$

We begin by considering an incoming plane wave scattering from a single potential located at the origin. In this case the original incoming plane wave is superimposed with a spherical wave of scattering amplitude $f(\mathbf{k}, \hat{\mathbf{r}})$, see Fig. 2.7. At large distances the scattering amplitude can only depend on the incident wave vector[5] and on the direction of the scattered light [22],

$$e^{i\mathbf{k}_i\cdot\mathbf{r}} \to e^{i\mathbf{k}_i\cdot\mathbf{r}} + f(\mathbf{k}_i, \hat{\mathbf{r}})\frac{e^{i\mathbf{k}_f\cdot\mathbf{r}}}{\mathbf{r}}. \tag{2.28}$$

For scattering of unpolarised electromagnetic radiation from a bound electron where the frequency of the X-rays is much larger than the typical resonance of an electron (i.e. hard X-rays) the scattering cross section can be written as (see appendix A for further details),

$$\left(\frac{d\sigma}{d\hat{\mathbf{r}}}\right) = |f(\hat{\mathbf{r}})| = \frac{1}{2}r_e^2(1+\cos^2\theta), \tag{2.29}$$

where $r_e = 2.8\times10^{-15}$ m is the classical electron radius. The total scattering cross section can then be calculated by integrating over all directions,

$$\int_0^{2\pi} d\Theta \int_0^{\pi} \sin(\theta)d\theta\left(\frac{d\sigma}{d\hat{\mathbf{r}}}\right) = \frac{8}{3}\pi r_e^2 = 0.665\times10^{-24}\text{cm}^2. \tag{2.30}$$

The exceptionally low value of the Thomson cross-section explains why experimentally X-ray scattering required the development of high intensity X-ray fluxes or to exploit the properties of coherent scattering and constructive interference from crystals in order to observe a significant signal.

2.2.1 Scattering from Ensembles of Electrons

Next it is typical to consider the scattering of X-rays from ensembles of electrons. This begins with the case of an electromagnetic wave scattering from two electrons, one at the origin and another at $\mathbf{r}$. The phase difference between the two waves can be shown to be

[5]For a spherically symmetric potential the scattering cross section is independent of $\mathbf{k}_i$.

$$\begin{aligned} \frac{2\pi}{\lambda} \times \text{path} &= \frac{2\pi}{\lambda}\left(\frac{1}{k_f}(\mathbf{k}_f \cdot \mathbf{r}) - \frac{1}{k_i}(\mathbf{k}_i \cdot \mathbf{r})\right) \\ &= \frac{2\pi}{\lambda}\frac{1}{k_i}(\mathbf{k}_i - \mathbf{k}_f) \cdot \mathbf{r} \\ &= \mathbf{k} \cdot \mathbf{r} \end{aligned} \tag{2.31}$$

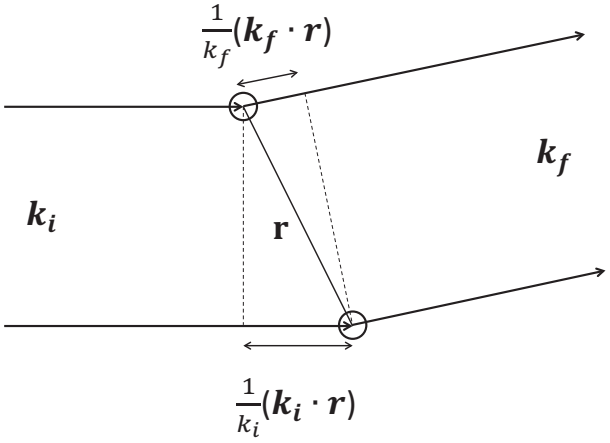

Figure 2.8: Path difference and change in phase due to scattering from two potentials separated by $\mathbf{r}$.

The total scattering amplitude from an ensemble is obtained by summing the scattered wave from each of the electrons ensuring that the phase of the scattered waves are correctly taken into account. It is clear that the scattering amplitude will hence depend not only on the scattering wave vector but also the relative position of the two electrons. In reality an atom is surrounded by many electrons which form a cloud around the atom. This electron cloud is typically defined as an electron density $n_e(\mathbf{r})$ around the atom. Addition of the scattering amplitudes from all the electrons with the correct phase shifts is given by,

$$f(Q) = \int n_e(\mathbf{r}) e^{i\mathbf{Q}\cdot\mathbf{r}} dV. \tag{2.32}$$

The function $f(Q)$ is known as the atomic form factor and reduces to Z, the number of electrons in the atom, for the forward scattering $\mathbf{Q} = 0$ case. Eq. (2.32) can be interpreted as the Fourier transform of the spatial distribution of electrons around the atom $n_e(\mathbf{r})$. Typically this spatial distribution is spherically symmetric

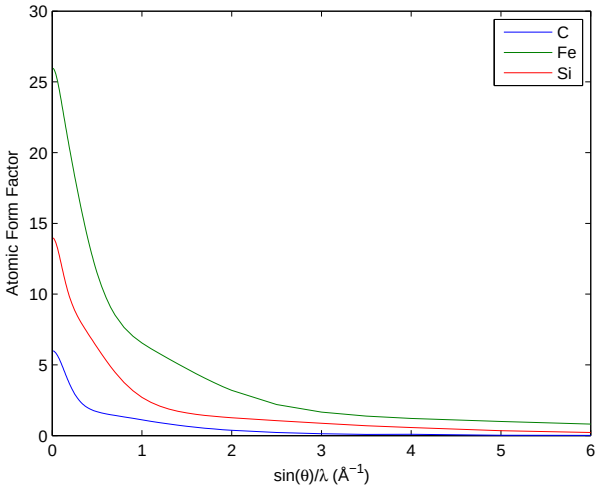

Figure 2.9: Spherically averaged atomic form factor for C, Si and Fe.

and so a Q dependence is introduced into the scattering behaviour. The form factor for some typical elements is shown in Fig. 2.9.

2.2.2 Scattering From Solids

This section will look at the scattering of hard X-rays from solids, in particular crystals where the atoms are arranged into a periodic lattice. Incoming waves scatter from the atoms as shown in Fig. 2.10 and the path difference between X-rays scattering from adjacent planes with spacing d is given by $2d\sin\theta_B$. The waves interfere constructively and destructively. When the path length is an integer multiple of the wavelength, i.e. when,

$$2d\sin\theta_B = n\lambda, \tag{2.33}$$

the waves interfere constructively. This method of looking at scattering from a crystal follows the ideas developed by Bragg in 1913. However, in parallel to Bragg an approach developed by von Laue described the same behaviour in reciprocal space. This idea was touched upon earlier in section 2.1.3.1 on the origin of the shape of the SSF.

The scattered amplitude from a crystal lattice described by the Bravais lattice $\mathbf{r}_n = n_1\mathbf{a} + n_2\mathbf{b} + n_3\mathbf{c}$ with N lattice points is given by the phase-correct addition of the scattering from each atom,

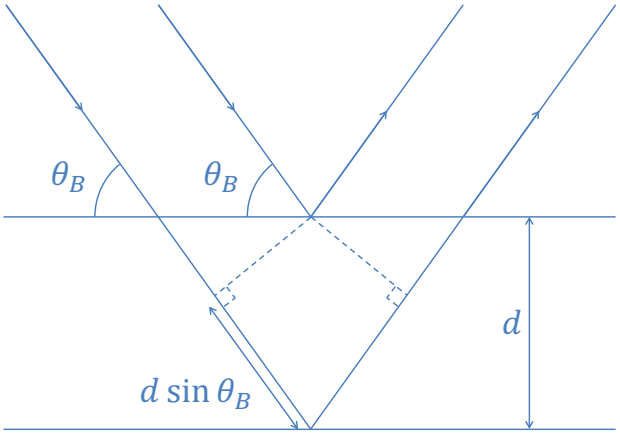

Figure 2.10: Schematic representation of Bragg diffraction. Bragg's law comes from the requirement that the path required for two X-rays to constructively interfere is $2d \sin \theta_B$.

$$F'(\mathbf{Q}) = \sum_n^N f(\mathbf{Q}) e^{i\mathbf{Q}\cdot\mathbf{r}_n}, \tag{2.34}$$

$$= f(\mathbf{Q}) \sum_{n_1,n_2,n_3}^N e^{i\mathbf{Q}(n_1\cdot\mathbf{a}+n_2\cdot\mathbf{b}+n_3\cdot\mathbf{c})}, \tag{2.35}$$

$$= f(\mathbf{Q}) \left(\sum_{n_1}^{N_1} e^{in_1\mathbf{Q}\cdot\mathbf{a}} \right) \left(\sum_{n_2}^{N_2} e^{in_2\mathbf{Q}\cdot\mathbf{a}} \right) \left(\sum_{n_3}^{N_3} e^{in_3\mathbf{Q}\cdot\mathbf{a}} \right). \tag{2.36}$$

Each term in Eq. (2.36) can be approximated as a geometric sum which leads to the equation,

$$F'(\mathbf{Q}) = f(\mathbf{Q}) \left(\frac{\sin[0.5N_1\mathbf{Q}\cdot\mathbf{a}]}{\sin[0.5\mathbf{Q}\cdot\mathbf{a}]} \right) \left(\frac{\sin[0.5N_2\mathbf{Q}\cdot\mathbf{b}]}{\sin[0.5\mathbf{Q}\cdot\mathbf{b}]} \right) \left(\frac{\sin[0.5N_3\mathbf{Q}\cdot\mathbf{c}]}{\sin[0.5\mathbf{Q}\cdot\mathbf{c}]} \right) \tag{2.37}$$

Eq. (2.37) describes the constructive and destructive interference pattern that the X-rays produce. For this to be non-zero $\mathbf{Q}$ the scattering wave-vector must satisfy the following three equations,

$$\mathbf{Q}\cdot\mathbf{a} = 2\pi h \quad \mathbf{Q}\cdot\mathbf{b} = 2\pi k \quad \text{and} \quad \mathbf{Q}\cdot\mathbf{c} = 2\pi l. \tag{2.38}$$

where h, k, and l are integers. These equations are known as the Laue conditions and reduce to the well known Bragg's Law[6]. The diffraction pattern from a crystal sample can therefore be thought of as a direct image of the underlying reciprocal lattice. In the real world the spatial extent of the crystal and thermal vibrations will alter the diffraction pattern from the simple picture discussed here, an idea exploited in section 3 to measure the ion temperature in a dynamically evolving system.

2.2.2.1 Kinematic vs Dynamic Diffraction

Up to this point the idea of X-ray scattering (and in particular diffraction) has been discussed on a micro-structural level. There has been the assumption that each point in the macroscopic sample will scatter independently from the rest of the crystal. This assumption is known as kinematic diffraction theory and is traditionally the norm. This assumption holds true for weakly interacting samples where the scattered signal is weak compared to the incoming X-rays. Each atom in the crystal will be exposed to the same incident beam. However, in reality this is not necessarily the case. For example, in an infinite perfect crystal diffracting in a manner similar to Fig. 2.10 each layer will diffract some of the X-rays from the incoming beam such that the layer below will be exposed to less radiation. This effect is measured by the primary extinction length in a crystal and is most prevalent in large perfect crystals.

In reality most samples are not perfect crystals and are made up of a mosaic of smaller crystallites each of which is slightly misoriented with respect to the crystal. The effect of this is to slightly broaden the diffraction peaks, but at the same time the chances of multiple crystallites lining up perfectly and reducing the beam intensity further into the crystal is considerably lower than in a perfect crystal. In such samples the primary extinction length is replaced by the secondary extinction length. For graphite samples such as those studied in section 3 the primary extinction length is 10 μm and the secondary extinction length 1.4 mm [194]. A full theory of diffraction taking into account the spatial extent of the sample and extinction is known as dynamical diffraction theory and is needed primarily for large perfect crystals.

2.2.3 Scattering From Liquids and Plasmas

The previous section demonstrates that the scattered intensity from a crystal is an image of the crystal lattice in reciprocal space (Laue conditions). However, this

[6]The Laue conditions can be written in a much more succinct form as $\mathbf{Q} = \mathbf{G}$ where $\mathbf{G} = h\mathbf{A} + k\mathbf{B} + l\mathbf{C}$. Here, $\mathbf{A} = \frac{2\pi}{V_c}(\mathbf{b} \times \mathbf{c})$, $\mathbf{B} = \frac{2\pi}{V_c}(\mathbf{c} \times \mathbf{a})$ and $\mathbf{C} = \frac{2\pi}{V_c}(\mathbf{a} \times \mathbf{b})$ are the reciprocal wave vectors.

result is much more general than this. In section 2.1.3 on correlation functions the structure factor of a sample is derived as a useful measure from statistical mechanics of quantifying correlations amongst atoms and electrons. However, this structure factor is simply the Fourier transform of the electron density distribution in a sample. Hence, it is not unsurprising that the intensity of scattered radiation from a sample can be directly linked to the structure factor of that sample,

$$I \propto S(\mathbf{Q}) = |F'(\mathbf{Q})|^2, \tag{2.39}$$

or more generally,

$$P_s(\mathbf{R}, \omega) d\Omega d\omega \propto \frac{P_0}{A} S_{ee}(\mathbf{k}, \omega) d\omega, \tag{2.40}$$

where ω is the frequency shift of the scattered photon and Ω the solid angle [73]. This expression holds in the kinematic limit and describes the intensity of scattered radiation at position $\mathbf{R}$ as proportional to the value of the dynamic electron structure factor S_{ee}, the incident power P_0 and the inverse irradiated area A.

It should be noted here that the dynamic structure factor in Eq. (2.40) is the electron-electron structure factor. i.e. the scattered radiation is a measure of the electron-electron density correlations. However, a widely used approach is to split S_{ee} into three separate terms each of which can be modelled independently [37, 38].

$$\begin{aligned} S_{ee}(k, \omega) = |f(k) + q(k)|^2 S_{ii}(k, \omega) + Z_f S^0_{ee}(k, \omega) \\ + Z_c \int S_{ce}(k, \omega - \omega') S_s(k, \omega') d\omega'. \end{aligned} \tag{2.41}$$

The three terms here can each be modelled independently making theoretical analysis simpler. The first term corresponds to electrons that are either bound or dynamically follow the ion motion. The term $f(k)$ is the traditional form factor while $q(k)$ can be thought of as a form factor for free electrons that surround the ions. This thesis is concerned primarily with the ion motion in dense plasmas and solids and so it is the first term S_{ii} that will be of primary interest. The second term in Eq. (2.41) is the high frequency component corresponding to electron-electron oscillations or plasmons. The third term represents bound-free transitions in the interactions. Essentially, it can be thought of as electron-hole pair creation by the incoming X-ray. Many X-ray scattering experiments ignore this term as it is *usually* smaller than the S_{ee} term.

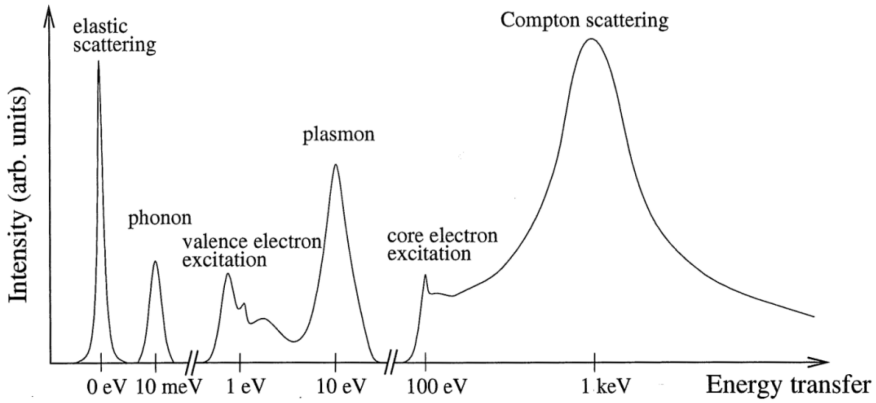

Figure 2.11: Schematic representing possible energy losses that can occur during inelastic X-ray scattering event, reproduced from [62].

The splitting of the spectrum accordingly raises an important point. Up to now the scattering has been considered to be entirely elastic. However, the generality introduced by Eq. (2.40) and the splitting in Eq. (2.41) are related to inelastic scattering, that is the X-ray gaining or losing energy during the scattering process. A typical X-ray inelastic scattering profile is shown in Fig. 2.11.

By resolving the energy transfers in addition to the momentum transfers of the scattered radiation information on both the structure and dynamics of a sample can be determined. Lattice vibrations and scattering from ions (phonons/ion acoustic waves) typically have a smaller energy transfer of the order of a few hundred meV while scattering from the lighter electrons (plasmons) gives higher energy transfers of the order of tens of eV. Chapter 5 concentrates on the difficulty of measuring experimentally the small energy shifts associated with ion motion and contains the first measurements of such shifts in a WDM sample.

Finally, it is common to separate the scattering from a material into a coherent and incoherent part. This splitting is somewhat arbitrary, and separates the scattering that arises from interference effects and collective scattering from that which occurs from interactions with single particles. This same splitting has been seen before in the section on correlation function where the pair distribution function is split into self correlation (Eq. (2.17)) and pair correlation (Eq. (2.18)) terms[7]. A rough estimate as to the importance of the two terms to the scattering process is to compare the length scales associated to the system with the wavelength of the probing radiation

[7]In the field of diffraction (scattering from crystals) incoherent scattering is given the name thermal diffuse scattering.

by use of the parameter $\alpha = \frac{1}{k\lambda}$, where k is the usual momentum transfer and λ a typical length scale such as a screening parameter or inter-particle distance. If $\alpha > 1$ then large length scale collective scattering is observed. If $\alpha < 1$ then single-particle scattering is observed.

X-ray Thomson scattering (XRTS) is today used as a broad term referring to the scattering of X-rays from a sample, both inelastic and elastically. Modern day experiments on dense plasmas employ the high spectral purity and large X-ray photon fluxes obtained from long-pulse optical laser irradiation of macroscopic samples to produce Ly_α or He_α sources, or using short pulse lasers to produce a K_α source. As well as these more conventional back-lighters the development of large FELs capable of producing high fluxes of monochromatic X-rays with much higher repetition rates has led to increased interest in their use in characterising dense matter. XRTS scattering provides a powerful tool of directly measuring the DSF of a material giving complete information on the structure and dynamics of both the electrons and ions in a system.

2.3 Classical Molecular Dynamics

Molecular dynamics is a method of solving the classical Newtonian equations of motions that govern the microscopic evolution of particles or atoms in a system. Computational advances in hardware and the development of massively parallel MD codes such as the Large-scale Atomic/Molecular Massively Parallel Simulator (LAMMPS) software package have meant that it has become a widespread and important theoretical tool [156]. It is used in many areas of science from physics to chemistry and biology and allows the dynamical behaviour of systems of gases, liquids, solids, surfaces, clusters [192] and more recently plasmas to be studied [135, 136] computationally. The advantage of this is that detailed properties of the system not readily accessible to experiment can be probed or manipulated in an effort to glean additional understanding.

The essence of MD is to take a system of N particles with masses (m_i,$i = 1, \ldots, N$) at positions $\mathbf{R}_i$ which interact through a prescribed potential given by $V(\mathbf{R})$ and evolve their trajectories by integrating Newton's laws of motion (within a particular statistical ensemble). Typically, in a classical simulation a pairwise additive potential is used - although this can be an 'effective' two-body potential where the effects of higher order interactions have been incorporated [5]. The equation of motion of the N particles is given by,

$$m_i\ddot{\mathbf{R}}_i = \mathbf{a}_i = -\nabla V_i\left(\mathbf{R}_i \ldots \mathbf{R}_N\right), \tag{2.42}$$

where in the case of a pairwise additive potential,

$$-\nabla V_i = \sum_{j\neq i}^{N} v(r_{ij}). \tag{2.43}$$

Once the initial conditions of the atoms in the simulation have been defined (i.e. the positions and velocities of every atom in the system) a discretised form of Eq. (2.42) is iteratively solved. The first proposed integration algorithm was developed by Verlet [195] in 1967 and is still generally used for most MD simulations performed today [60]. The algorithm begins by examining two Taylor expansions for the particle positions. One forward in time,

$$\mathbf{r}_i(t+\Delta t) = \mathbf{r}_i(t) + \mathbf{v}_i(t)\Delta t + \frac{\mathbf{a}_i(t)}{2}\Delta t^2 + \frac{\dot{\mathbf{a}}_i(t)}{3!}\Delta t^3 + O(\Delta t^4) \tag{2.44}$$

and one backwards,

$$\mathbf{r}_i(t-\Delta t) = \mathbf{r}_i(t) - \mathbf{v}_i(t)\Delta t + \frac{\mathbf{a}_i(t)}{2}\Delta t^2 - \frac{\dot{\mathbf{a}}_i(t)}{3!}\Delta t^3 + O(\Delta t^4), \tag{2.45}$$

where Δt is the time step of the simulation. Adding Eqs. (2.44) and (2.45) gives,

$$\mathbf{r}_i(t+\Delta t) \approx 2\mathbf{r}_i(t) - \mathbf{r}_i(t-\Delta t) + \frac{\mathbf{a}_i(t)}{2}\Delta t^2 + O(\Delta t^4). \tag{2.46}$$

This equation can be used to update the positions of the atoms at each time-step where the acceleration is derived from Eq. (2.42). The error is of order of Δt^4, and the computational time-step should be selected such that $\Delta t^4 << r(t)$ and the trajectory does not diverge. In practice a slightly modified version of this integrator known as the 'velocity Verlet' algorithm is used where an additional step calculating the updated velocities is included,

$$\mathbf{v}_i(t+\Delta t) = \mathbf{v}_i(t) + (\mathbf{a}_i(t+\Delta t) - \mathbf{a}_i(t))\Delta t. \tag{2.47}$$

This particular implementation first calculates the new atom positions using Eq. (2.46), and from these new positions calculates the updated velocities from Eq. (2.47). It has been shown previously that this algorithm generates identical results to the original algorithm but at any instant in the time the positions and velocities are correctly defined. The advantage of this is that properties that depend on these quantities such as the total (kinetic + potential) energy are accurately captured. Since this algorithm

requires the positions of the atoms at two time-steps, care should be taken when initialising the simulation, although in this work we allow the simulation to equilibrate before extracting data and as such this additional error has a negligible effect. All simulations performed in this work have used the 'velocity Verlet' algorithm.

As mentioned previously the choice of time-step should be $\Delta t^4 << r(t)$ such that the trajectories of the particles do not diverge from their true trajectory. Another way of stating this is that the algorithm conserves the total energy of the system. If the time-step is too large the atoms can travel too large a distance on a single time-step and hence end up un-physically close to another atom, this situation leads to a jump in potential and hence total energy. Conversely the time-step must be large enough such that the physical process under consideration is visible in a simulation of reasonable length. This balance becomes particularly important for high temperature MD simulations where the atoms can travel large distances on a short time-scale due to large velocities. A typical time-step for the simulations present in this work is about a femtosecond.

2.3.1 The Ergodic Hypothesis and Ensembles

MD can be used to simulate the microscopic behaviour of particles in a system which is in thermal equilibrium. However, practically we are usually trying to extract a macroscopic property of the system such as pressure or the DSF which can be compared with experimental results. From statistical mechanics we know that measurements of thermodynamic properties are an ensemble average, that is they are a weighted average over the different microstates[8] of the system. The different weighting factors in the average correspond to the different ensembles in statistical mechanics, each of which serves a different purpose. The most common is the microcononical ensemble, which holds the number of particles, volume of the system and total energy constant (known as constant NVE). This ensemble equates to averaging equally over all microstates with a total energy equal to E. Another common ensemble is the canonical ensemble (NVT) where the temperature rather than the total energy is kept constant, this is often used to represent systems that are coupled to a heat bath of infinite extent. Experimentally where the number of atoms is large (N$> 10^{23}$) the system is in the thermodynamic limit and the results from each ensemble can be shown to be formally equal. In MD where we have considerably fewer atoms care must be chosen when choosing the correct ensemble [193].

[8] A microstate of the system in this case is defined as a particular set of atom positions and velocities.

A straight forward MD simulation using an energy conserving integrator can be seen to be a representation of the microcanonical (NVE) ensemble. In MD simulations an (NVT) ensemble is often approximated by running in the microcanonical ensemble and applying a thermostat to keep the mean velocity constant. The simplest of these is the velocity rescaling thermostat which scales the velocities of the atoms at each time step such that the temperature of the system is maintained at a constant value. A velocity rescaling 'thermostat' is relatively common, but known to be non-physical and does not in fact reproduce any statistical mechanical ensemble. Often velocity rescaling is used to bring the system in to equilibrium before being switched off for the calculation of the system properties. More complex methods of maintaining constant velocity have since been developed such as the Nose-Hoover (deterministic) or Langevin (stochastic) thermostats which are designed to better mimic temperature fluctuations present in a real system and approximate the (NVT) ensemble.

A MD simulation running in the microcanonical ensemble which has run for a sufficiently long time will reach an equilibrium macrostate where these macroscopic quantities are constant (or rather fluctuate around an average value). If a thermodynamic property is calculated from the simulation by averaging over successive microstates we will obtain a time average rather than the desired ensemble average. We can imagine however that if the simulation was allowed to run for a long enough time it would eventually sample all microstates accessible to it and the time average would converge on the ensemble average. This is the idea behind the ergodic hypothesis, it relates the time average properties of the system to the ensemble average. Mathematically it is stated as,

$$\langle ... \rangle = \lim_{\tau \to \infty} \frac{1}{\tau} \int_0^\tau ...dt \tag{2.48}$$

where the left hand side of Eq. (2.48) is the ensemble average and the right hand side a time average. This hypothesis has never been proven rigorously, and even if this were possible a simulation of infinite extent would be necessary to obtain an exact result. Additionally, the integration performed in Eq. (2.48) is a discrete summation over time-steps and so the final results is only ever an approximation. A longer simulation with finer time-steps will calculate more accurately the ensemble average. In this work all results are checked for convergence with an increasing number of time-steps so the accuracy with which an average can be found is known. A detailed description of the ergodic hypothesis can be found in [60].

2.3.2 Periodic Boundary Conditions

In deriving thermodynamic properties from MD simulations we are often required to the take the thermodynamic limit, that is the limit where $N \to \infty$. However, it is obvious that such a simulation would be impossible. Even though the largest simulations possible today contain a few trillion atoms [68], this only represents a volume of around one cubic micron, it is clear that surface effects will still play a huge role in determining behaviour [133]. This is overcome by introducing periodic boundary conditions (PBC) whereby if an atom is to exit a simulation from one direction it would enter the the opposite side with the same velocity. In addition all forces between atoms must also be transmitted across the boundary - in essence an infinite lattice is simulated.

However, this does not completely negate finite size effects in the simulation. For example, a particular problem in this work looking at the ion dynamics is that the simulation can only support ion modes up to the size of the simulation box. Mathematically this means that the structure factor cannot be determined below a value of $k = \frac{2\pi}{L}$, where L is the box length. Numerous studies have looked at changes in the SSF as the number of particles is increased, a recent study by J. P. Mithen in 2013 found the thermodynamic properties did not change above 600 atoms [133].

2.3.3 Classical Potentials

Surprisingly it is not the numerical integrator or ergodic hypothesis that are the main contributors towards errors from MD simulations, rather they stem from inaccuracies present in the inter-atomic potential. Most MD potentials are developed empirically and often contain fitting parameters which are used to match the simulation to experiment. Typical properties used for this are the lattice parameter or bulk modulus in solids [92] and RDF or SSF in dense plasmas [198].

The simplest potentials are pair-wise interactions where the potential is a function only of the distance between two atoms. Examples of this type are the Lennard-Jones potential which is often used to describe liquids and simple solids,

$$V(r) = 4\epsilon \left[\left(\frac{\sigma}{r}\right)^{12} - \left(\frac{\sigma}{r}\right)^{6} \right], \tag{2.49}$$

and the Yukawa[9] (or screened coulomb) potential often used in plasma physics, see Eq. (2.4). A potential based on the screened coulomb potential but with additional

[9]The origin of the Yukawa potential in plasmas comes from the screening effect of electrons around the ions.

short range repulsion (SRR) effects has recently shown success in accurately describing the strong ion correlations in a dense aluminium plasma [123, 197],

$$V_{ii}^{\text{eff}}(r) = \left[\frac{Z^2\mathrm{e}^2}{r} + \frac{(Z_c^2 - Z^2)\mathrm{e}^2}{r}e^{-br}\right] e^{-\kappa r}, \tag{2.50}$$

where $Z_c = 13$ is the atomic number for aluminium, $Z = 3$ is the charge state, and κ is the Thomas-Fermi screening length. The parameter b represents the effect of increased nuclear repulsion when there is interpenetration of the bound electron charge clouds around each nucleus. It determines the onset of the SRR. Setting $b \to \infty$ gives the usual Yukawa potential. This potential will be be explicitly examined in chapter 4 and compared with results from quantum MD simulations. It will be shown that although the static properties are in agreement some differences arise in the dynamic structure factor.

The Lennard-Jones potential is derived from the electrostatic dipole-dipole interaction present in gases and liquids but at low temperatures freezes to a FCC structure. This property and huge amounts of historical work lead to this potential often being a substitute in more phenomenological studies. However, a new method was developed to capture more accurately the behaviour of complex materials such as phase transitions and vacancy energy. The limitation of pairwise potentials in solids stems from their preference to maximise the number of nearest neighbours thus minimising the binding energy of the system, that is they have a tendency to form close packed structures[10]. In metals the embedded atom model (EAM) is a particularly successful approach,

$$E_i = F\left(\sum_{i\neq j}\rho(r_{ij})\right) + \frac{1}{2}\sum_{i\neq j}\phi(r_{ij})\,. \tag{2.51}$$

The EAM approach was developed in 1983 by Daw and Baskes [42]. The basic premise is that the excess energy felt by an interstitial atom at any point is given by the sum of internal energy over all other atoms in a system, Eq. (2.51). The potential felt by the excess atom, provided the interstitial does not alter the crystal, is then the potential at that point regardless of if the interstitial is present. In Eq. (2.51) F is the energy required to embed an atom into electron density ρ and ϕ is the pair-wise potential between two atoms. Chapter 3.5 utilises an EAM potential for gold to simulate the mechanical oscillations in gold nano-foils after short-pulse laser radiation.

[10] A common problem with pair potentials is that Cauchy pressure is found to be zero, whereas it should be non-zero for real metals.

The difficulty associated with classical MD is finding a potential that can accurately capture the physics of a situation across large temperature and density conditions as well acting as a predictive tool. Quantum molecular dynamics (QMD), or DFT MD, is a tool which allows the potential between ions to be calculated from first principles on each time-step of the simulation, the benefit of this is that situations where the potential is difficult to describe analytically (for example during bonding) or where the potential changes due to electron temperature increases (for example the system may ionise as it is heated). However, the downside of this method is that it requires huge computational effort, particularly if the number of atoms in the simulation is large. Typical QMD simulations scale as $O(N^3)$ compared to $O(N^2)$ for classical calculations. Chapter 4 details a new method known as orbital free DFT that has shown considerable success in the high temperature and high pressure regime. Section 4 gives details of the first calculations of the DSF performed for WDM using self-consistent quantum molecular dynamics.

2.4 Intense Laser-Matter Interactions

The interaction of a high-power laser with a solid target is the main method used in this work to both create HEDP states of matter and produce the X-rays used for diagnosis.

Throughout this thesis various phenomena are exploited to create HEDP states of matter, but they are unified in that they utilise intense laser-matter interactions. This section will discuss in detail the interaction of a high intensity laser with a solid target in the context of creating extreme matter states. The three main mechanisms used in this work are direct radiation absorption into the free electrons (inverse-brehmstrahlung), charged particle acceleration (protons or electrons) and shock wave generation.

It is important to distinguish laser-matter interactions performed with either a long or short pulse beam, as this dictates the time-scales associated with the experiment. A long pulse laser will typically have an intensity of $10^9 - 10^{16}$ W cm^{-2} and a pulse length measured in nanoseconds, while a short pulse laser can have intensities of up to 10^{23} W cm^{-2} and typically a pulse length measured in picoseconds or even femtoseconds. The energy contained in a long pulse laser beam can be more than an order of magnitude greater than in a short-pulse beam and hence can drive larger samples to greater pressures and temperatures.

2.4.1 Target Normal Sheath Acceleration

The method utilised in section 3 to create a WDM state is to use a high intensity proton beam created through a method known as target normal sheath acceleration (TNSA). This method uses a short pulse laser interaction with a thin foil, the laser-matter interaction induces charge seperation on the surface of the foil. This charge seperation leads to extremely high longitudinal electric fields which in turn accelerates ions and protons on the surface resulting in a high intensity proton beam. On a short time scale the protons heat the sample (primarily through collisions with free electrons) and there is not enough time for hydrodynamic expansion to occur. This method allows for solid density but high temperature samples to be created in the laboratory. The standard set-up for TNSA is the interaction of a pulse above 10^{18} W cm^{-2} with a thin foil [168]. The interaction of the laser with the solid target and subsequently the expanding plasma drives fast electrons into the target with a quasi-thermal energy spectrum given by,

$$N_{\text{fast}}(E) = n_0 e^{\left(-\frac{E}{k_B T_{\text{fast}}}\right)} . \tag{2.52}$$

Many different processes act during laser-matter interaction and are responsible for electron acceleration, however the pondermotive potential of the laser pulse and direct conversion of laser energy into hot electrons through $\mathbf{J} \times \mathbf{B}$ heating are thought to contribute the most in this regime [149]. The electrons travel through the thin foil with a large angle of divergence and emerge on the rear-side. As the electrons escape the target the foil becomes positively charged and an electrostatic sheath field is created. This field is strong enough to confine electrons with energies well in excess of an MeV and causes the electrons to re-enter the target in a process known as refluxing. Eventually electrostatic sheath fields build up on both the front and rear surface of the target. At the rear surface there is no plasma cloud created through laser irradiation and so the sheath fields are not screened allowing them to reach strengths of several TV/m. These fields can accelerate ions from the rear surface of the target (typically impurities on the surface) up to MeV energies.

The second method utilised in section 3 to create a WDM state is similar to the TNSA method in that a short pulse laser hitting a thin foil is used, however, the difference is that the sample to be heated is mounted such that it is in contact with the interaction foil. The result of this is that no sheath field is created and the fast elections themselves are accelerated through the foil and into the target. The

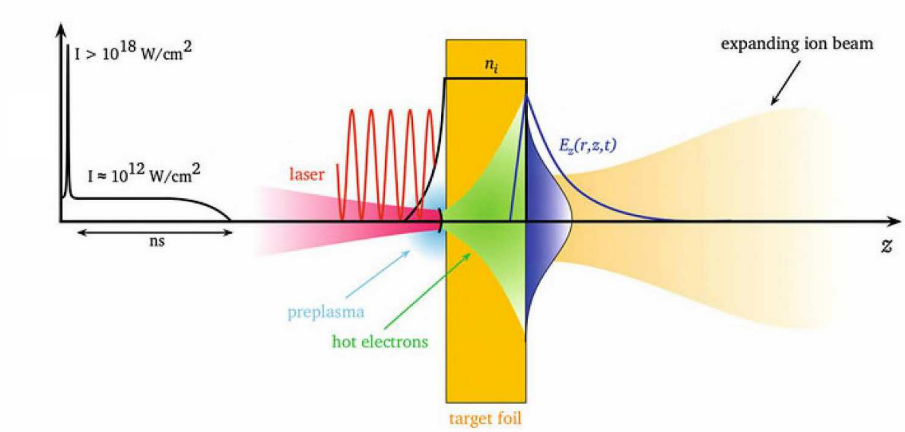

Figure 2.12: Schematic showing the principles of the target normal sheath acceleration (TNSA) ion acceleration method, reproduced from Ref. [167].

fast electrons scatter in the target depositing energy into the ions. Details of the differences between proton and electron heating is given in section 3.

2.4.2 Laser Produced Shock Waves

A completely separate method of producing HEDP in the laboratory is to create a high pressure shock wave in the sample. This can occur when a long-pulse laser of the order of nanosecond duration and with an intensity of above approximately 10^9 W cm^{-2} interacts with a solid target. The surface is heated and expands to produce a plasma, as this plasma expands the reaction force produces a shock wave in the target. Typically one of two cases are used, either the plasma is free to expand or a transparent material is used to confine the plasma. If the expanding plasma is confined by a transparent material then typically higher pressures can be reached in the sample. This technique is known as adding an ablator or tamper to the target and a full description of the effects of material and thickness can be found in the review article by Swift *et al.* [189].

A shock is characterised as a discontinuity in a thermodynamic variable, typically the material pressure or density. The laser produced shock wave method is used throughout this thesis to produce HEDP states of matter. A set of equations known as the *Rankine-Hugoniot* relations define the relationship between material before and after the shock. These equations are the result of applying conservation laws across the shock front. They are typically derived by considering a solid of cross sectional area A, carrying a shock wave travelling at velocity u_s. This shock wave is driven by

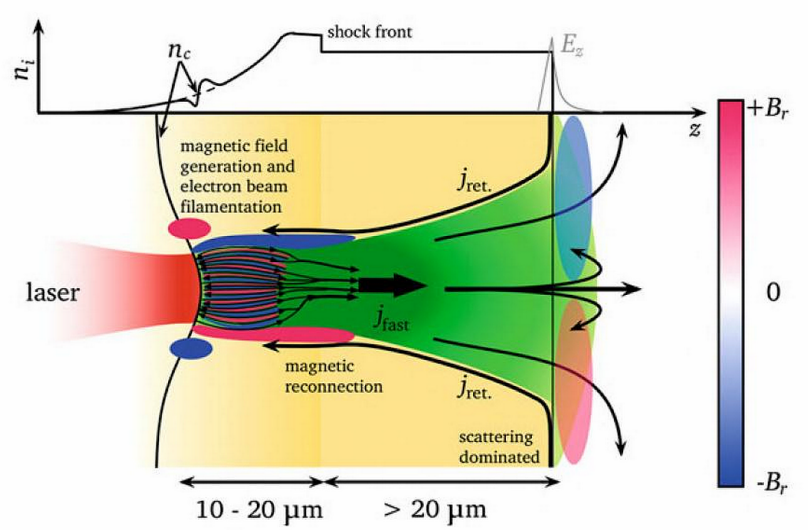

Figure 2.13: Diagram showing interaction between a laser pulse and a solid target. The laser is absorbed into the target up to a critical density. The expanding plasma drives a shock wave into the target with the shock front defined by a discontinuity in ion density. There exists a complex interaction between magnetic and electric fields with the dynamically evolving shock front. Figure reproduced from Ref. [167].

the surface moving at a velocity of u_p, typically represented by a piston. We define the pressure and density in the shocked region as p_s and ρ_s respectively and in the un-shocked region as p_0 and ρ_0 respectively. The first conservation law to consider is mass conservation. In a time t the shock front has moved forward a distance of $u_s t$ and thus compressed a volume $A u_s t$. Simultaneously the free surface has moved forward a distance of $u_p t$, hence the amount of new shocked material is given by $A(u_s - u_p)t$. Since the total mass of material must be the same before and after this time we can multiply by the respective densities and equate the two volumes,

$$\rho_s A(u_s - u_p)t = \rho_0 A u_s t \,, \tag{2.53}$$

which gives the first *Rankine-Hugoniot* relation,

$$\rho_s(u_s - u_p) = \rho_0 u_s \,. \tag{2.54}$$

The second equation comes from considering momentum conservation. The momentum gained by the shocked material, given simply by mass multiplied by velocity, is $\rho_0 u_s A t u_p$. This additional momentum must be equated to the impulse generated at the shock front, $(p_s - p_0)At$. The second equation is then,

$$\rho_0 u_s u_p = p_s - p_0 \,. \tag{2.55}$$

The third equation comes from energy conservation and states that the increase in internal and kinetic energy is equal to the work done on the system. It is expressed as,

$$\rho_0 u_s \left(\epsilon_s(\rho_s, p_s) - \epsilon_0(\rho_0, p_0) + \frac{u_p^2}{2} \right) = p_s u_p \,, \tag{2.56}$$

where ϵ_s and ϵ_0 are the specific internal energies of the shocked and un-shocked material. The left hand side of this equation is the increase in internal and kinetic energy while the right hand side is the work done on the material. However, in order to close the *Rankine-Hugoniot* relations the EOS must be known, i.e. the functional form of ϵ_s and ϵ_0.

For most materials of interest it is generally not possible to write down an analytical form of the EOS[11]. For solids the internal energy is made up of multiple contributions. The first of these comes from the elasticity of the material, that is as the increase in internal energy as the material is compressed due to the overlap of the repulsive electronic wave functions. The second contribution comes from the thermal energy associated with the system. In the absence of thermal vibrations (T=0 K) the compression of a solid is a reversible process, however a shock wave is an irreversible process, and the discontinuity at the shock front can be considered to heat the material and increase the thermal pressure. The EOS must include contributions from both this elastic and thermal pressures. Typically it is the elastic pressure that is most difficult to derive analytically as detailed knowledge of the inter-atomic potential must be known. As mentioned in section 2.3.3 this is not trivial across a wide range of densities and temperatures.

Shocks also differ in solids and fluids due to their ability to support shear strain. The *Rankine-Hugoniot* equations assume a hydrostatic condition where the off-diagonal components of the stress tensor are all zero. Therefore, a shock in a solid typically has a region of elastic response before hydrostatic conditions are reached. As material passes through the shock front it is compressed uniaxially into an elastic state, this state remains until the material has time to respond and enter a plastic state through

[11] In the case of the ideal gas with constant heat capacity the internal energy can be expressed as $\epsilon = \frac{1}{\gamma - 1} pV$ where γ is the ratio of specific heat capacity $\frac{c_p}{c_v}$. This allows the *Rankine-Hugoniot* equations to be expressed as $\frac{\rho_0}{\rho_s} = \frac{(\gamma-1)p_s + (\gamma+1)p_0}{(\gamma-1)p_0 + (\gamma+1)p_s}$.

defect transport and generation [44], this time leads to differing velocities for the elastic and plastic shock fronts [131]. The velocity of the plastic wave is related to the intensity of the shock, and so naturally two regimes are present, those with a plastic wave velocity below that of the elastic wave (weak shock regime) and those with a plastic wave velocity above that of the elastic wave (strong shock regime). Only in the weak case do we observe splitting of the wave into a faster elastic component and slower plastic wave. Typically, the pressures used in section 5 are in the strong shock regime.

However, a strong shock can induced a phase transition in a material altering the shock Hugoniot. As is standard in thermodynamics a phase transition is defined as a discontinuity in a thermodynamic variable or a derivative thereof. A first order phase transition is a discontinuity in the first derivative. Considering the Gibbs free energy, G, of a material,

$$dG = VdP - SdT\,, \tag{2.57}$$

where S is the entropy of the system. It follows that at constant temperature a change in the Gibbs free energy must be associated with a corresponding change in volume.

Finally, there a subtlety to shock wave formation in a material. In order to allow a shock wave to propagate through the sample there must be no dispersion of the shock. This is normally expressed by the condition that the high amplitude components travel faster than the low amplitude ones such that a stable shock front exists. The high pressure components of the shock travel faster than the low pressure components causing the shock front profile to steepen. This is expressed mathematically as,

$$\left(\frac{\partial^2 P}{\partial V^2}\right) > 0\,. \tag{2.58}$$

This condition means that the Hugoniot must be concave in order for a shock to propagate, this is typically true for most solid materials, including those covered in this work [92].

Chapter 3

Temperature Relaxation in Dense Plasmas

3.1 Introduction

On short time-scales, due to the preferential and rapid heating of one subsystem over the other (electrons or ions, depending on the details of the excitation mechanism), there is no guarantee that extreme states of matter created in the laboratory will be in thermodynamic equilibrium. Relatively few experimental results have attempted to measure such relaxation rates, and those that have seem to indicate relaxation times that are much longer than those predicted by ideal or nearly-ideal plasma models.

This behaviour, which essentially suggests a weak energy coupling between electrons and ions, has been attributed to the excitation of collective modes that screen the electron-ion potential, and thus reduce the energy transfer. Depending on the exact implementation of such coupled-mode theories, relaxation times between one and two orders of magnitude smaller than that produced by the ideal Spitzer-Brysk model have been predicted [47]. Experimental verification is thus essential, and, at the same time, knowledge of the times over which the energy relaxation processes occur is of fundamental importance in any WDM work.

This chapter is concerned with the experimental measurement of electron-ion, or rather electron-phonon, coupling in highly excited states of matter. It is based on three separate experiments looking at graphite heated with an intense proton beam [209], graphite heated with an intense electron beam [206] and gold heated directly with laser illumination [207]. Although this chapter is about experimental measurement of electron-ion equilibration rates, a brief review of some of the models available for temperature relaxation is included.

3.2 Models for Temperature Relaxation

Describing electron-ion relaxation rates is a complex topic and many models have been produced over the years to describe this effect. The first of these was developed for a hot two-temperature plasma by Landau and Spitzer in 1936 [114, 183]. This approach assumes that the electrons and ions are in thermal equilibrium and hence can be assigned temperatures T_e and T_i respectively. It assumes the electrons and ions are weakly coupled and transfer energy only through small angle Coulomb scattering. The electrons travel in straight lines and the scattering event can be defined by an impact parameter b and the energy of the impact. By integrating over all possible impact parameters an equation for the energy transfer cross-section between an electron and an ion of charge Z is obtained [63, 66],

$$Q_{ei}(v) = \frac{4\pi Z e^4}{m_e v^4} \lambda_C \,, \tag{3.1}$$

where v is the relative velocity between the electron and ion and λ_C the Coulomb logarithm. The Coulomb logarithm is the logarithm of the ratio of maximum and minimum impact parameters in the sample. It is common in low density systems to take the Debye screening length ($\lambda_D = (k_B T_e / 4\pi e^2 n_e)^{\frac{1}{2}}$) and the distance of closest approach ($\rho_\perp = Z_i e^2 / m_e v_{th}^2$) for these two terms. Here, $v_{th} = (k_B T / m_e)^{\frac{1}{2}}$ is the thermal velocity of the electron. Additionally, a quadratic sum of the distance of closest approach and the deBroglie wave length ($\lambda_{dB} = \hbar / m_e v_{th}$) can be used to approximate quantum diffraction effects [63],

$$\lambda_C = \ln\left(\frac{b_{max}}{b_{min}}\right) = \ln\left(\frac{\lambda_D}{\sqrt{\rho_\perp^2 + \lambda_{dB}^2}}\right) . \tag{3.2}$$

These phenomenologically derived cut-offs are not exact derivations, but are however physically motivated. They are simply an educated guess towards a correct result [63]. This approach obviously fails in systems where $\lambda_C < 0$, such as in dense highly degenerate systems where the deBroglie wave length becomes larger than the screening length leading to non-physical (i.e. negative) results. Some success has been found in treating the electron orbits as hyperbolic where the Coulomb logarithm becomes [63],

$$\lambda_C = \frac{1}{2} \ln\left(1 + \frac{b_{max}^2}{b_{min}^2}\right) . \tag{3.3}$$

From these results the electron-ion relaxation time, the quantity discussed throughout this chapter, can be shown to be,

$$\tau_{LS} = \frac{3m_e m_i}{8\sqrt{2\pi} n_i Z_i^2 e^4 \lambda_C} \left(\frac{k_B T_e}{m_e} + \frac{k_B T_i}{m_i} \right)^{3/2} . \tag{3.4}$$

Going beyond this model are extensions to degenerate systems by Brysk in 1974 [29], the use of quantum kinetic theory over the classical kinetic equations by Gericke *et al.* in 2002 [65] and, most relevant to this work, the description of energy transfer through coupled collective modes by Dharma-wadana and Perrot [47, 48, 77] in 1998[1].

One problem with the Landau-Spitzer method is that it considers the electrons and ions as separate particles that interact purely through binary collisions. Collective behaviour in the electrons (plasmons) or ions (phonons, ion acoustic waves) is not included. Of particular consequence to this is that when the collective behaviour is included in the theory the electron and ion modes can couple together, an effect which leads to dynamic screening and significantly reduced energy transfer rate when compared to binary collision models.

The formula developed by Dharma-wadana and Perrot is rather involved, however in the weak coupling limit an approach based around the Lenard-Balescu equations gives,

$$\begin{aligned} \frac{\mathrm{d}E_e}{\mathrm{d}t} = -4\hbar \int \frac{\mathrm{d}\mathbf{k}}{(2\pi)^3} \int \frac{\mathrm{d}\omega}{(2\pi)} \omega \left| \frac{V_{ei}(k)}{\epsilon(k,\omega)} \right|^2 \Im\mathrm{m}\chi_{ee}(k,\omega) \\ \times \Im\mathrm{m}\chi_{ii}(k,\omega) \left[n_B \left(\frac{\hbar\omega}{k_B T_e} \right) - n_B \left(\frac{\hbar\omega}{k_B T_i} \right) \right] , \end{aligned} \tag{3.5}$$

where in the Lenard-Balescu equations the dynamic response of the electrons are handled within the random phase approximation [63]. The rate of change of thermal energy in the electron subsystem E_e in Eq. (3.5) can be seen to depend on the electron-ion potential $V_{ei}(k)$, the full dielectric function $\epsilon(k,\omega)$, and the density response of the electrons χ_{ee} and ions χ_{ii}. Here, $n_B(x) = [\exp(x) - 1]^{-1}$ is the Bose function. This method includes degeneracy effects and, since the electrons and ions are treated within the same formula, the influence of electrons on the ions and the ions on the electrons is included from the start.

Inspecting carefully Eq. (3.5) the interaction between species V_{ei} is screened by the dielectric function, and as discussed earlier in section 2.1.3 and 2.2.3 the full dielectric function is related to the dynamic structure factor of the electrons (through

[1] A numerical approach to calculating electron-ion equilibration rates based on classical molecular dynamics has recently shown considerable success but requires the use of positive electrons to prevent the system collapsing due to coulomb attraction between the atoms and electrons. In addition, effects due to electron screening or coupled modes are not accessible through this method [49].

the fluctuation dissipation theorem) which in turn relies on knowledge of the electron and ion dynamics in a system. Hence, ion dynamics can have a significant impact on energy transfer rates.

In practice numerical evaluation of χ is difficult due to sharp peaks in both the numerator and denominator. Hence, often the numerator is set to unity (a method comparable to using Fermi's Golden Rule) or evaluated within the random phase approximation. Whichever method is used they come to the same conclusion; that is the energy transfer rates are significantly reduced. This can be seen in Fig. 3.1 reproduced from data given in Dharma-Wardana and Perrot, 1998 [47]. Depending on the exact implementation of such coupled-mode theories, relaxation times between one and two orders of magnitude smaller than those produced by the ideal Spitzer-Brysk model [29, 183] have been predicted.

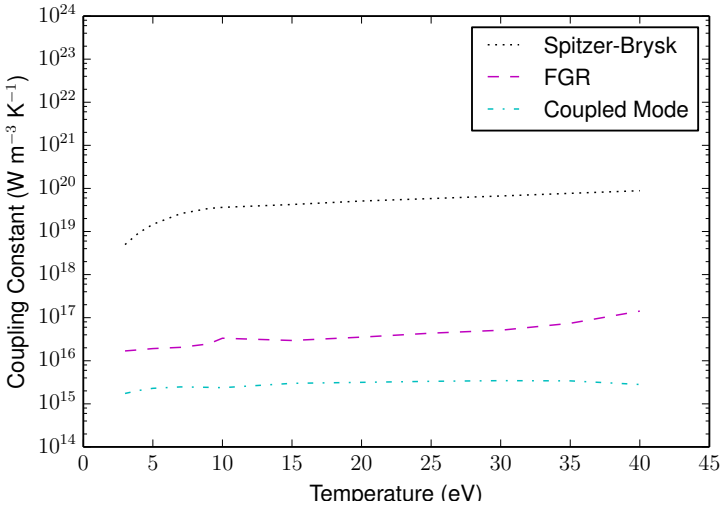

Figure 3.1: Electron-ion Relaxation rates calculated using Spitzer-Brysk, Fermi's golden rule and coupled mode theories for solid density Aluminium with an ion temperature of 946 K. This figure is reproduced from data in Dharma-Wardana and Perrot (1998) [47].

3.2.1 Temperature Relaxation in Metals

While the field of temperature relaxation in highly non-equilibrium and dense systems is a particularly new area of research, in condensed matter systems it has been studied for many decades and is better understood. The main difference between the two fields is that here the ion lattice is considered to remain cold (often T_{ion}=0 K) while the electron sub-system is heated.

Detailed calculations of the electron-phonon energy transfer rate have been performed by Lin *et al.* in 2008 [120]. These go beyond treating the electrons as a free electron gas and instead use rate equations first developed by Allen (1987) for electron-phonon collisions [6]. The result of this work is that the electron-phonon equilibration rate can be described by,

$$\frac{\mathrm{d}E_e}{\mathrm{d}t} = \frac{4\pi}{\hbar}\sum_{k,k'}\hbar\omega_q|M_{k,k'}|^2 S(k,k')\delta(\epsilon_k - \epsilon_{k'} + \hbar\omega_q)\,, \tag{3.6}$$

where k and q describe the electron and phonon fundamental quantum numbers, M is the electron-phonon scattering matrix describing the probability of scattering a photon in state k with energy ϵ_k to state k' with energy ϵ'_k by a photon with energy $\hbar\omega_q$. The term S is the equation is known as the thermal factor and is equal to $S(k,k') = (f_k - f_{k'})n_q - f_{k'}(1-f_k)$. This term describes the absorption and emission of phonons scattered within the sample in terms of the electron (f_k) and phonon (n_q) occupation numbers. Assuming that these occupation numbers can be described by Fermi-Dirac and Bose-Einstein functions and Taylor expanding the resulting equation to keep only terms where the scattering energy is small compared with the thermal energy Allen and Lin found,

$$\frac{\mathrm{d}E_e}{\mathrm{d}t} = \frac{\pi\hbar k_B\lambda\langle\omega^2\rangle}{g(\epsilon_F)}\int_{-\infty}^{\infty} g^2(\epsilon)\left(-\frac{\partial f}{\partial\epsilon}\right)\mathrm{d}\epsilon(T_i - T_e)\,. \tag{3.7}$$

The terms in this equation such as the electronic density of states (DOS) $g(\epsilon)$, the second moment of the phonon DOS $\langle\omega^2\rangle$ and the electron-phonon mass enhancement parameter λ can all be calculated from first principles DFT. For systems close to equilibrium this method has considerable success but fails to capture the complexity present in highly non-equilibrium systems or systems with a more difficult electronic structure such as semi-metals. Fig. 3.2 shows that the electron-ion coupling constant is approximately 2.5×10^{16} W m^{-3} K^{-1} in room temperature gold but rises rapidly above $\sim$3000 K.

3.2.2 Extreme States of Matter

Relatively few experiments have attempted to measure relaxation rates [33, 144, 163, 209], and those that do seem to indicate relaxation times that are much longer than those predicted by ideal or nearly-ideal plasma models [29, 114]. This behaviour, which essentially suggests a weak energy coupling between electrons and ions, has so far been attributed to the excitation of collective modes screening the electron-ion

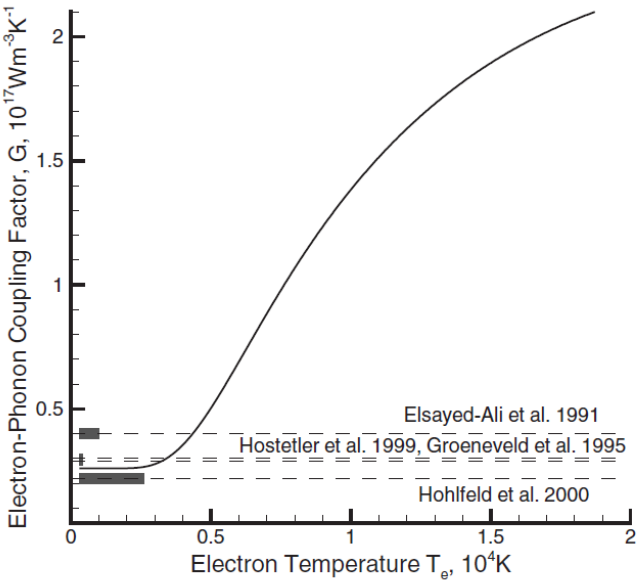

Figure 3.2: The electron temperature dependence of the electron-ion equilibration constant for gold calculated by Lin *et al.* (2008) [120]. Calculations were performed with the VASP DFT code. Also shown are commonly used experimental values with the temperature range accessed experimentally highlighted in bold. The ion temperature in this calculation is set to $T_i = 0$ K.

potential as discussed above. Experimental verification is thus essential, and, at the same time, knowledge of the time scales over which the energy relaxation processes occur is of fundamental importance in any WDM work.

The reason temperature relaxation rates are vital to understanding extreme states of matter is related to the creation of WDM states in the laboratory using lasers or pulsed power machines [162]. Generation of these states via these methods results in producing a system of highly coupled ionic liquids immersed in a partially degenerate electron sea. On short time-scales, due to the details of the heating mechanisms and slow energy transfer, there is no guarantee that the matter will be in thermodynamic equilibrium. Many codes that are used to model high power laser experiments, particularly those based on hydrodynamic descriptions, use the Spitzer model and hence vastly underestimate the time required to reach thermodynamic equilibrium.

Descriptions of electron-ion equilibration are often performed within a phenomenological model describing the energy flow between the electron and phonon subsystem known as the two-temperature model (TTM). Within this formalism the evolution of the temperatures of the two subsystem can be described by a pair of coupled differential equations [11],

$$C_{\text{ele}}\frac{\partial T_{\text{ele}}}{\partial t} = \nabla\cdot(K_{\text{ele}}\nabla T_{\text{ele}}) - g\,(T_{\text{ele}} - T_{\text{ion}}) + S_{source}(\mathbf{r},t)\,, \tag{3.8}$$

$$C_{\text{ion}}\frac{\partial T_{\text{ion}}}{\partial t} = \nabla\cdot(K_{\text{ion}}\nabla T_{\text{ion}}) - g\,(T_{\text{ele}} - T_{\text{ion}})\,, \tag{3.9}$$

where $C_{\text{ele/ion}}$ are the specific heat capacities of the electron and ion components respectively, $K_{\text{ele/ion}}$ the thermal conductivity[2] and g the electron-ion coupling coefficient. A solution to this equation requires an EOS model to relate the energy density to the temperature of each subsystem and, hence, calculate the heat capacities C_{ele} and C_{ion}. In the work presented later on graphite two different EOS models are used, PROPACEOS 4.2, which is based on a chemical model [124] and *ab-initio* DFT for the electrons coupled to classical molecular dynamics for the ions (see appendix E). The coupling coefficient itself is difficult to model from first principles as it depends on the interaction dynamics of the electron and phonon subsystems. However, it allows the complexity of the physical system to be contained within a single parameter.

3.3 Measuring Temperature Relaxation in Solids

The main method used throughout this chapter to measure the ion temperature in a non-equilibrium sample is time resolved X-ray diffraction. In section 2.2.2 the origin of the diffraction peaks is shown to be given by the Fourier transform of the atomic positions. For example, an infinite in extent perfect crystal will lead to a set of distinct diffraction lines (See the top panel of Fig. 3.3). Adding in finite size and temperature effects, panels 2 and 3, it can be seen that the height of this diffraction peak is given by the Fourier transform of a top hat function, representing the spatial extent of the sample, the position of the peak in reciprocal space and the thermal vibrations in the solid.

To show this mathematically the motion of the ions in a crystal can be decomposed into multiple terms, $\mathbf{R}_i$ which represents the equilibrium position of the ions in the lattice as well as $\mathbf{u}_{oi}(t)$ and $\mathbf{u}_{ti}(t)$ which represent the displacement of ions from these points via oscillatory and translational motion respectively. Following the derivation by Gregori *et al.* (2003) [79, 80] which is reproduced in appendix D we can derive a

[2]To estimate of the effects of thermal conduction we calculate the time it takes for the temperature to equilibrate throughout the sample. The equation $dE/dt = K\nabla^2 T$ can be approximated by $t \approx \left(\frac{K\Delta T}{L^2\epsilon_{3d}}\right)^{-1}$ which for a L=50 μm thick graphite (K=0.8 W/cm/K) target with energy density $\epsilon_{3d} = 10^{11}$ eV/μm^3 corresponding to ΔT = 1 eV ∼11000 K gives an equilibration time of ∼70 μs. This makes thermal conductivity negligible on time scales of the experiments performed here.

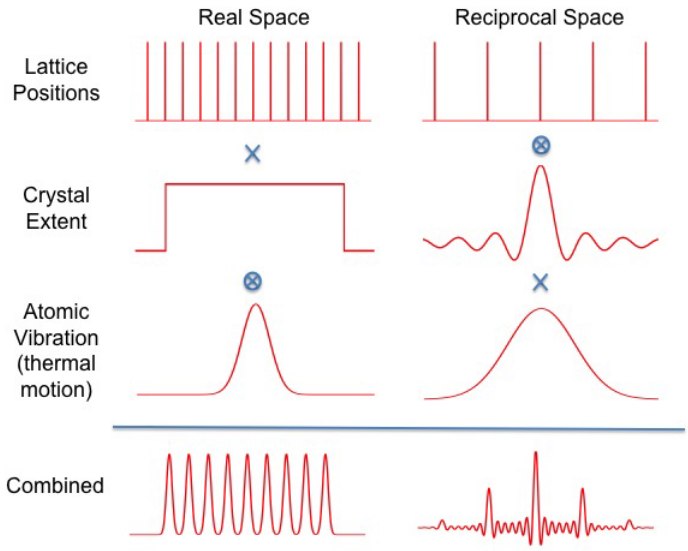

Figure 3.3: Origin of the shape of the static structure factor in a single crystal [108].

set of equations showing the temperature dependence of the ion-ion structure factor in a solid (note that the intensity of scattered X-rays is then proportional to the square of this term).

$$S(\mathbf{k},t) = F_t(\mathbf{k},t)\left(1 - e^{-2W} + e^{-2W}\, b(\mathbf{k})\right) , \tag{3.10}$$

where,

$$F_t(\mathbf{k},t) = \frac{1}{N}\sum_{i=1}^{N}\sum_{j=1}^{N}\langle e^{-i\mathbf{k}.[\hat{\mathbf{u}}_{ti}(0)-\hat{\mathbf{u}}_{tj}(t)]}\rangle_T , \tag{3.11}$$

and,

$$b(\mathbf{k}) = \frac{1}{N}\sum_{i=1}^{N}\sum_{j=1}^{N} e^{-i\mathbf{k}.[\mathbf{R}_i-\mathbf{R}_j]} . \tag{3.12}$$

Here $\langle ... \rangle_T$ denotes an ensemble average of N particles at temperature T. Eq. (3.11) can be thought of as a translational structure factor ($\approx N$ in a solid), and captures coherent motion in the sample; it is sometimes called thermal diffuse scattering and to first order represents the phonon spectrum of a crystal. Eq. (3.12) represents the Bragg peaks of a perfect crystal at T=0 K. Eq (3.10) describes, to first order, the reduction in coherent scattering as the parameter $2W = k^2\langle \mathbf{u}_{oi}^2 \rangle$ is increased. In the harmonic approximation [7, 139] the displacement of an atom from its equilibrium position can be related to the ion temperature T_i through,

$$2W = \frac{3k^2\hbar^2}{Mk_B\Theta_D}\left[\left(\frac{T_i}{\Theta_D}\right)^2 \int_0^{\frac{\Theta_D}{T_i}} \frac{udu}{e^u - 1} + \frac{1}{4}\right] . \tag{3.13}$$

This relation shows that there is a reduction in the scattered intensity due to increased thermal vibrations of the atoms around their equilibrium lattice sites [122]. However, as pointed out by Ernstorfer *et al.* [55] great care must be taken when using Eq. (3.13) in a highly non-equilibrium system. In such cases the electron excitation can impact the Debye temperature, Θ_D, dramatically and as such it should be treated as a function of electron temperature, $\Theta_D(T_e)$. A full *ab-initio* analysis of the phonon DOS at higher electron temperatures is necessary to calculate an exact value of the Debye temperature[3]. Furthermore, this analysis assumes that the atomic form factor does not change, an argument that holds if $T_{\text{ele}} < T_F$ where $T_F \sim 13.3$ eV. A Thomas-Fermi calculation of the average ionisation shows that between room temperature and 2 eV it changes by less than $\sim$2% [174].

This method assumes diffraction within the kinematic limit, i.e. as the sample is heated and the atoms vibrate around the lattice positions fewer X-rays are coherently diffracted from the sample. In a full dynamical calculation it can be easily seen that these X-rays that no longer diffract from the top layer of the target would thus be diffracted from the lattice deeper within the target. The graphite samples used in this work can be considered within the kinematic approximation due to their mosaic structure, provided the c-axis depth of each crystallite is less than the primary extinction length. The thin (200 nm) gold samples have a an extinction length (207 nm) comparable to the sample thickness, suggesting they cannot be treated fully within the kinematic limite. However, epitaxially grown films are known to have a high defect density [91], reducing the degree of perfection in the crystal and allowing the kinematic approximation to be used.

[3]In this work we have taken $\Theta_D = 800$ K for bulk graphite, this value agrees with previously published values and experimental measurements for a graphite lattice at room temperature [159]. In reality, as energy is deposited into the electron system by the proton beam, the potential landscape that surrounds the ions may undergo changes and the approximation of a constant Θ_D must be verified. By performing finite temperature DFT-MD simulations, we have found that $\langle u_\perp^2 \rangle = 0.020\,\text{Å}^2$ when $T_{\text{ion}} = T_{\text{ele}} = 300$ K and $\langle u_\perp^2 \rangle = 0.023\,\text{Å}^2$ when $T_{\text{ion}} = 300$ K, and $T_{\text{ele}} = 20,000$ K. These displacements correspond to $\Theta_D = 820\,\text{K}$ and $\Theta_D = 760\,\text{K}$, respectively. This indicates little variation of the out-of-plane Debye temperature with T_{ele}, and the approximation $\Theta_D = 800$ K seems entirely justified.

3.4 Temperature Relaxation in Graphite

Solid density carbon with pressures above one megabar and temperatures in the thousands of Kelvin lie in the WDM region, which sits between the traditional solid state and the high temperature plasma domains. Expansion techniques are no longer applicable and neither the kinetic nor the potential energy can be treated perturbatively; as such, the phase diagram of carbon is still largely unknown for both the highly excited solid [25] and fluid phases [150]. These extreme matter states are highly relevant to the understanding of the evolution and the structure of large planets and compact objects [40, 81, 98, 111, 171], as well as for ICF experiments [71, 127], EOS and opacity models [16].

Here we focus our work on graphite, a highly anisotropic semimetal that has proven to be a material with unique electronic [218] and phonon properties [101]. It has the highest electron mobility and thermal conductivity of any bulk material. Both features suggest unique behaviour in the electron-ion coupling and indeed it exhibits exceptionally low relaxation rates [101, 116, 117, 155, 177, 178, 188, 209, 215] that disagree with current theoretical models [117].

A large body of work exists studying the electron-ion energy transfer in both graphite and graphene. However, in the interpretation of the experimental data, uncertainties remain in disentangling the excitation mechanism with the relaxation pathways. Since nearly all studies used an optical pump to create a non-thermal distribution of the electrons within the first few tens of nanometres of the sample surface, inhomogeneities in the heating and direct coupling to optical phonons have been suggested as possible sources of uncertainty. While the overall energy transfer between electrons and ions is slow, a strong and almost instantaneous interaction between the excited electrons and high energy (200 meV) coupled optical phonons(COPs) was found.

The different channels of energy transfer in carbon act as a complicating factor when modelling electron-ion temperature relaxation within a simple TTM. Although previous experiments have investigated lattice temperature in weakly to moderately driven systems [122, 177] these utilised direct coupling of a pump laser to optical phonons (see, *e.g.*, Ref. [101]).

3.4.1 Proton Heated Graphite

Here we discuss the results of an experiment where a graphite sample has been heated to very high temperatures by an intense beam of protons, but the lattice remains

intact. This allows us to investigate electron-phonon coupling in the high-temperature limit, that is, near melting. Energy deposition by protons also avoids many issues related to laser heating of solids, *e.g.*, direct coupling of the laser light to phonon modes and inhomogeneous heating.

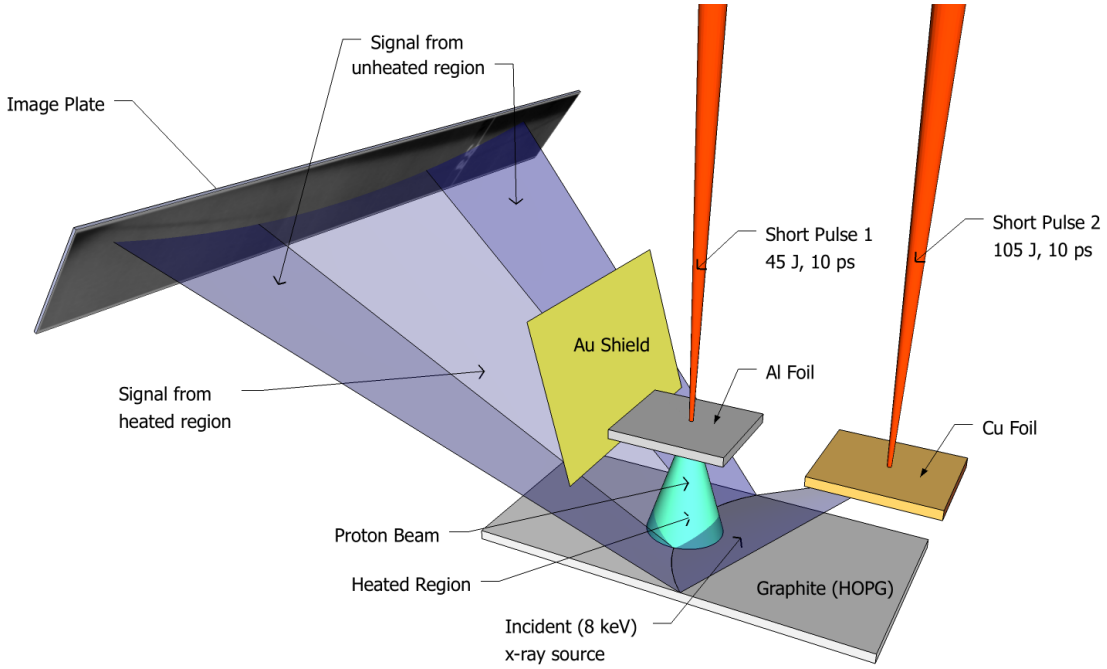

Figure 3.4: The experiment was performed on the Titan Laser at the Jupiter Laser Facility, Lawrence Livermore National Laboratory (USA). The 150 J, 10 ps Titan beam at the fundamental wavelength λ_0=1054 nm was split into two arms in a pump-probe configuration. To heat the graphite sample, 30% of the energy was delivered onto a thin aluminium foil with a 10 μm focal spot. The accelerated electrons create an electric field which drives an intense proton beam normal to the rear surface of the aluminium foil. The remaining energy was focused 225 ps later with a 10 μm focal spot onto a copper disk to generate Cu-K_α probe X-rays. The image plate detector was placed 300 mm away from the graphite sample at 27.4° to detect the Bragg diffracted light. The magnification of the set-up was 138. The proton beam forms a spot of diameter ∼1.0 mm on the sample. The sample consisted of 50 μm thick HOPG covered with 30 μm of polypropylene.

3.4.1.1 Experimental Set-up

The experiment was carried out on the Titan laser at the Jupiter Laser Facility, Lawrence Livermore National Laboratory (USA). Fig. 3.4 and its caption give a detailed description of the laser beams, diagnostics and sample set-up. We employed

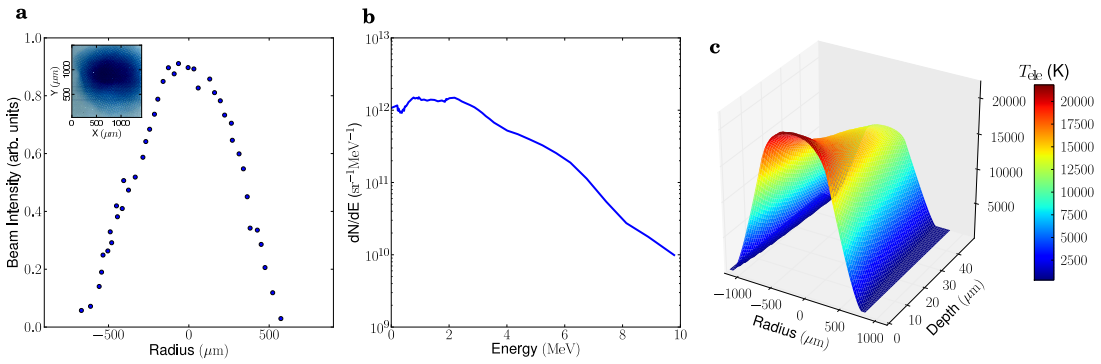

Figure 3.5: **a)** Measured spatial distribution of the proton intensity showing a ∼1 mm width at the position of the sample surface. The inset shows the radiochromic film data used to monitor the proton beam. **b)** Proton energy spectrum taken from the centre of the proton beam and plotted up to the maximum energy measured. **c)** Calculated electron temperature in the HOPG sample. A ray tracing simulation is used to follow the proton trajectories through the sample. The simulation uses the measured proton distributions in space and energy shown in panels a) and b). From the energy deposited by the proton beam and the specific heat of a given EOS model, the electron temperature throughout the sample can be inferred. Electron heat capacities from density functional simulations are used to obtain the temperature distribution shown.

proton beams created through the TNSA mechanism outlined in section 2.4. Protons with energies of up to 10 MeV were produced by high-intensity short-pulse irradiation of a 10 μm Al foil [164] (see Fig. 3.5a and Fig. 3.5b for the spatial and energy distributions measured). The protons emerge in a 60° cone from the rear surface of the foil, which was placed 1 mm from the highly orientated pyrolytic graphite (HOPG) sample, this leads to heating within a ∼1 mm diameter region after a time of flight on the order of $t \approx 100$ ps. A 30 μm plastic layer, placed between the proton beam and the HOPG target, was used to stop electrons, heavier ions and low energy protons, ensuring uniform and predictable heating of the sample. Additionally, the plastic layer acts as a tamper, effectively preventing any thermal expansion on the timescales probed in the experiment. The protons provide isochoric heating throughout the 50 μm thick HOPG. The heating due to the protons was calculated from measurements of the proton spectrum (see Fig. 3.5b) taken on shots where the HOPG sample was absent and scaled with laser intensity for shots where the sample was present [164]. The measured spectrum was used in a proton ray tracing simulation, in which the energy deposition was modelled using the known stopping power of protons in graphite [23]. Over 99% of the proton energy is deposited in the electron subsystem

(see appendix F) and the electron temperature accordingly rises to $T_{\text{ele}} \approx 17,000$ K (1.5 eV) on a picosecond time-scale, see Fig. 3.5c). Within the electron subsystem, thermalisation occurs on a femtosecond time-scale [54]. Subsequently, the electron-phonon energy exchange rate determines the temperature evolution of the electron and phonon subsystems.

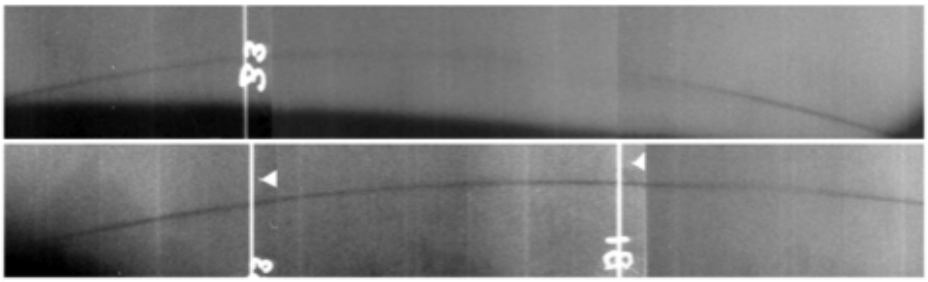

Figure 3.6: Raw Bragg scattering signal on image plate from proton heated (top) and unheated (bottom) graphite samples.

X-rays for probing the sample were generated by a second laser pulse, delayed by $t = 225$ ps with respect to the first pulse, which irradiated a copper foil and, thus, acted as a source of Cu-K_α line radiation of 8 keV. Simultaneously, the Bragg scattering of these X-rays was measured and the reduction in scattering intensity from the heated regions of the sample was observed. As mentioned before this reduction in intensity is related to increased thermal vibrations of the atoms around their equilibrium lattice sites. Fig. 3.6 shows a noticeable decrease apparent in the raw data when comparing the heated and unheated diffraction lines. Fig. 3.7 shows a line-out of the decreased intensity of X-rays scattered across the surface of the sample. A heated region of approximately 1 mm in width is apparent where the intensity drops to ∼30% compared with the scattering from the ambient region. With knowledge of the inter-atomic potential and the partial phonon DOS, the magnitude of thermal vibrations can be connected to the lattice temperature. More specifically, we relate the vibrations to the ratio of lattice and Debye temperatures, T_{ion}/Θ_D, where the Debye temperature characterises the lattice strength through the frequency of the DOS. $\Theta_D = 800$ K was extracted from density functional theory calculations and shown to have little variation with electron temperatures in the range considered in our experiment. Taking into account the effects of absorption and extinction within the sample[4], the analysis shows that a drop of around 70% in the Bragg intensity is

[4]When using the Debye-Waller equation to compare the predicted Bragg peak intensity ratio, I_T/I_{T_0}, to the experimental values, X-ray attenuation through the graphite sample must be taken into account. An X-ray scattered from a depth d into the sample must be weighted by a factor

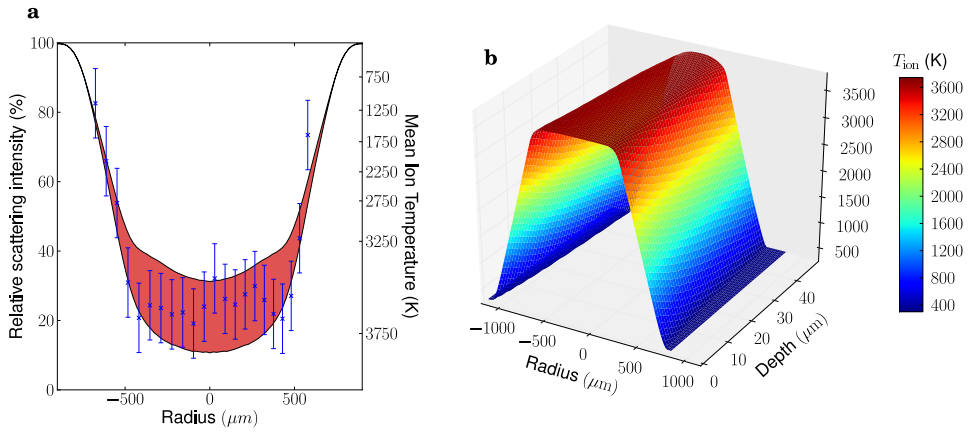

Figure 3.7: Intensity of scattered radiation and corresponding lattice temperature at t=225 ps. **a)** The measured Bragg peak intensity of the scattered radiation from across the sample surface. The values are plotted relative to the Bragg intensity without heating. This ratio is given by $I/I_0 = e^{-2W}$, where $2W = k^2\langle u_\perp^2\rangle$ is the Debye-Waller factor. Here, $k = 3.73$ Å^{-1} is the scattering wave number with its direction parallel to the c axis of the graphite lattice and $\langle u_\perp^2\rangle$ is the out-of-plane rms deviation from the equilibrium ion positions. Since $\langle u_\perp^2\rangle$ is a function of $T_{\mathrm{ion}}/\Theta_{\mathrm{D}}$ (see main text), we can calculate the ion temperature from the measured decrease in the Bragg scattering intensity, as reported on the right axis of the plot. The shaded region corresponds to ion temperatures obtained by solving the two-temperature model with an electron-phonon coupling constant of $g = 0.45 - 0.8 \times 10^{16}$ W K^{-1} m^{-3}. **b)** Calculated spatial distribution of the lattice temperature within the graphite sample based on the measured decrease in Bragg scattering.

consistent with a lattice temperature of around 3500 K.

3.4.1.2 Results

The average electron-phonon coupling during the experiment can now be obtained by solving the TTM discussed earlier using the initial electron temperature and the lattice temperature at $t = 225$ ps as boundary conditions. In this work, we use two different EOS models: PROPACEOS 4.2, which is based on a chemical model [124] and includes many adjustments based on experiments, and *ab-initio* DFT for the electrons coupled to classical molecular dynamics for the ions (see appendix E). The source term in the TTM was obtained from proton ray tracing simulations, $S_{proton}(\mathbf{r}, t) \approx S_{proton}(\mathbf{r}, t = 100\,\mathrm{ps})$. This provides the initial conditions, and the

$\exp(-d/\xi)$, where $\xi = 193\,\mu$m is the total extinction length. It accounts for absorption ($\xi_{abs} = 222\,\mu$m) and secondary extinction ($\xi_{ext} = 1487\,\mu$m). Primary extinction ($\xi_{pri} = 4\,\mu$m) within the sample is negligible due to the smaller c-axis depth of the mosaic crystallites. Since $\xi \gg 50$ μm (the depth the HOPG sample), the X-rays can be thus considered to probe the full volume of the sample.

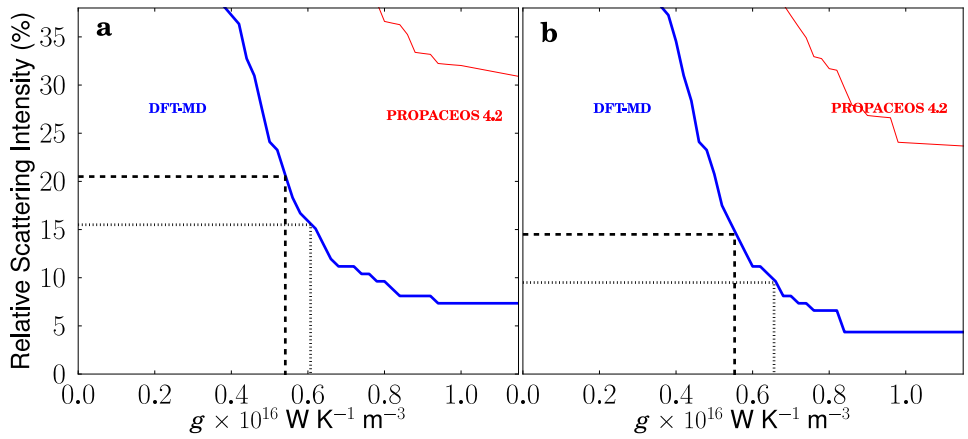

Figure 3.8: Relative Bragg scattering intensity at the centre of the graphite sample at $t = 225$ ps plotted against the electron-phonon coupling coefficient. The calculations are performed by solving the TTM with two different models for the EOS and heat capacities: PROPACEOS 4.2 (red line) and DFT-MD (blue line). The experimentally measured scattering intensity is shown by the dotted and dashed lines, where the error margin of 5% was estimated from the variation in intensity across unheated samples. The energy of the laser producing the proton beam is **a)** $E_{\text{laser}} = 39.3$ J and **b)** $E_{\text{laser}} = 46.5$ J.

energy relaxation then evolves according to the TTM. By scaling g the coupling constant to fit the observed lattice temperature at t=225 ps, we are able to infer its value from the experiment.

The results from the fitting procedure for g are shown in Fig. 3.8. The energy deposited by the proton beam heated the sample close to melting, but the lattice remained intact as we still observe Bragg scattering. The extracted electron-phonon coupling coefficient, averaged over the conditions in the first 225 ps of the temperature equilibration, is found to be in the range of $g = 0.54 - 0.66 \times 10^{16}$ W K^{-1} m^{-3}. The 5% error margin results from the variance in intensity on unheated shots. It is also evident from Fig. 3.8 that only calculations based on the EOS model from DFT-MD are able to match the experimental data at $t = 225$ ps. Indeed, it has previously been shown that chemical models for the EOS are not sufficiently accurate for describing warm dense graphite, primarily due to the exclusion of the latent heat [150]. As an example the time evolution of the electron and ion temperatures extracted from the TTM with the correct energy deposition and coupling parameter are shown in Fig 3.9.

In order to compare with previously published data in the lower temperature range, we transfer our measurements to the dimensionless parameter λ that is related

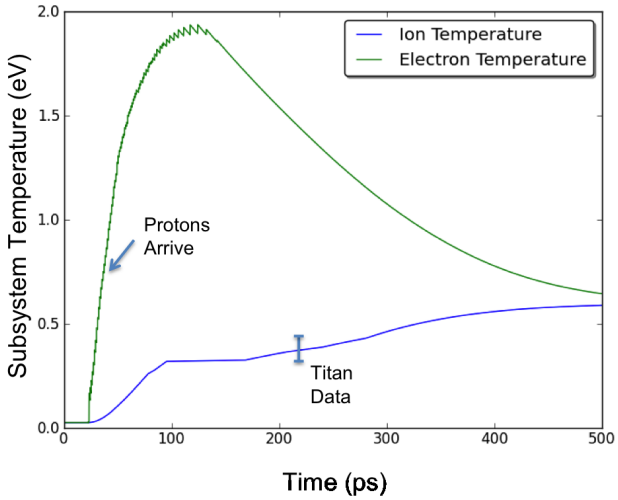

Figure 3.9: The time evolution of the mean electron and ion temperature in the proton heated graphite after irradiation by a high intensity proton beam. The data shown corresponds to a coupling parameter of 0.6×10^{16} W K^{-1} m^{-3}.

to the coupling coefficient by $g = 3\lambda\hbar C_{\text{ele}}\langle\omega^2\rangle/\pi k_B T_{\text{ele}}$, where $\langle\omega^2\rangle \approx \Theta_D^2/2$ is the second moment of the phonon DOS [28]. Converting our values for the coupling coefficient gives $\lambda \sim 0.06$. This is considerably lower than the value for typical metals, however previous work on weakly excited carbon have also found low coupling in room temperature graphite [101, 117] ($\lambda < 0.2$), and graphene [31] ($\lambda = 0.05 - 0.1$). These results have been attributed to a small DOS at the Fermi energy in semimetals, an argument that becomes highly questionable for the high electron temperatures present in our experiment.

3.4.2 Electron Heated Graphite

In an attempt to disentangle the energy relaxation pathways in graphite this section presents the results of an experiment similar in design to the previous section, however, in this case the graphite sample is heated to high temperatures by a fast electron beam as opposed to a proton beam. This again allows us to investigate electron-phonon coupling in the high-temperature limit, but as the energy deposition is driven by fast electrons it again avoids many issues related to laser heating of solids, *e.g.*, direct coupling of the laser light to phonon modes and inhomogeneous heating. Moreover, the electron heating occurs on times shorter than in the case of proton driven samples which helps to simplify the analysis. In the case of hot electrons the stopping power is

very different to protons and so the electron-ion equilibration can be further decoupled from the heating mechanism.

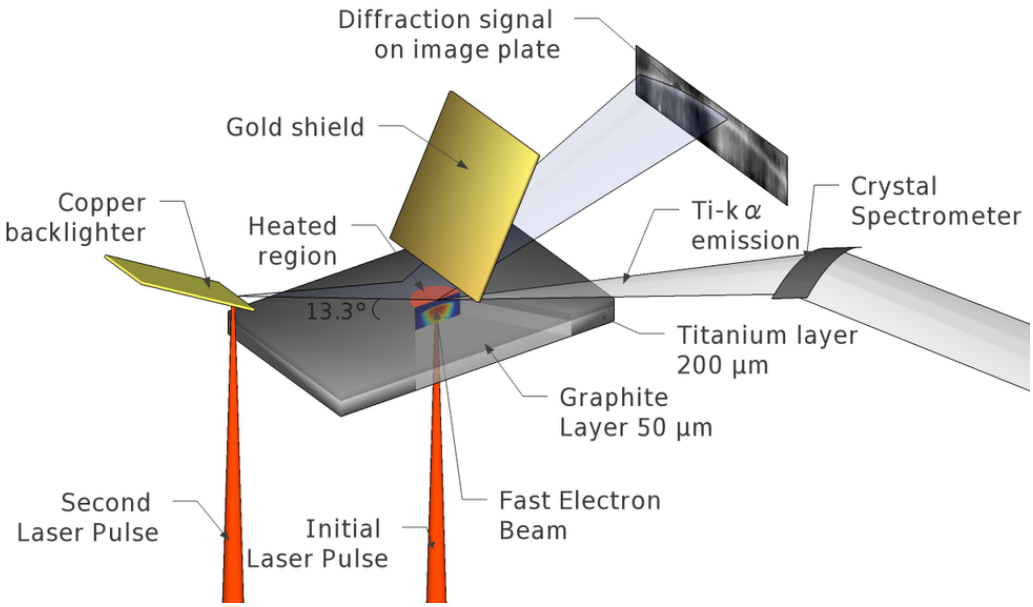

Figure 3.10: Schematic of the experimental set-up. The experiment was performed at the PHELIX Laser Facility, GSI Helmholtz Facility, Germany. The 80 J, 0.7 ps beam at the fundamental wavelength λ_0=1054 nm was split into two arms in a pump-probe configuration. To heat the graphite sample, 50% of the energy was delivered onto the titanium substrate with a 30 μm diameter focal spot. The fast electron distribution heats the graphite attached to the rear of the sample. The remaining energy was focused between 0 and 1000 ps later with a 30 μm diameter focal spot onto a copper foil to generate Cu-K$_\alpha$ probe X-rays. The copper foil is angled with respect to the target to reduce the source size. An image plate detector was placed 100 mm away from the graphite sample at 13.3° to detect the Bragg diffracted light.

3.4.2.1 Experimental Set-up

The experiment was carried out at the PHELIX Laser Facility, at the GSI Helmholtz Institute (Darmstadt, Germany). Fig. 3.10 shows the schematic of the experiment. A 0.7 ps long laser pulse delivering 80 J of energy was split into two equal arms, with one focused onto a 200 μm thick Ti substrate with the rear surface coated with a 50 μm thick HOPG layer. The presence of the Ti substrate enables the electrons to isochorically heat the graphite while preventing direct illumination from the laser. The interaction drives a non-thermal fast electron current through the target. These electrons are accelerated by the radiation field of the laser pulse and can reach energies

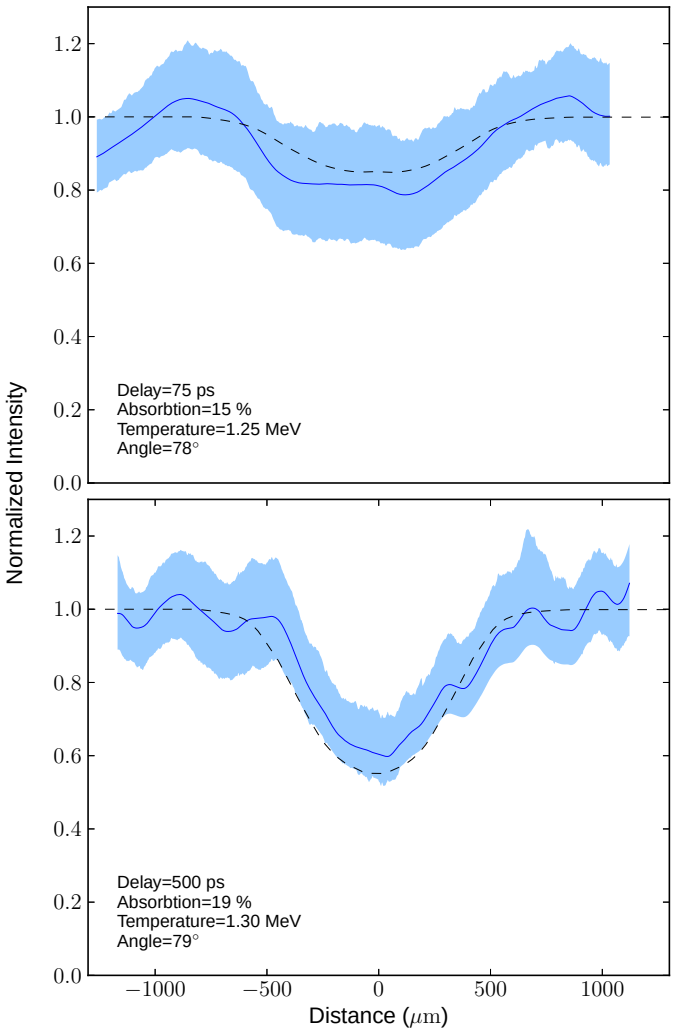

Figure 3.11: Experimental data showing the reduction in intensity of Bragg scattering from the surface of the graphite (solid lines) for two different delays of 75 and 500 ps. Experimental error bars are represented by the shaded region. The dashed line shows simulation results taken from the ZEPHYROS fast electron code applied to the two temperature model with a coupling constant of 0.2×10^{16} W K^{-1} m^{-3}. Also shown are the calculated absorption, temperature and divergence angle of the fast electron distribution through comparison with the emitted Ti K-shell line emission.

of the order of one keV to several MeV [210]. The background thermal electrons in the solid target respond to this fast electron current by setting up resistive electric fields and strong return currents. Through a process of collisions and ohmic heating the fast electron population loses energy to the surrounding material.

The second laser beam is delayed by a varying amount (0-1000 ps) with respect to the first and irradiates a copper foil acting as a short pulse source of 8 keV Cu-K$_\alpha$ line

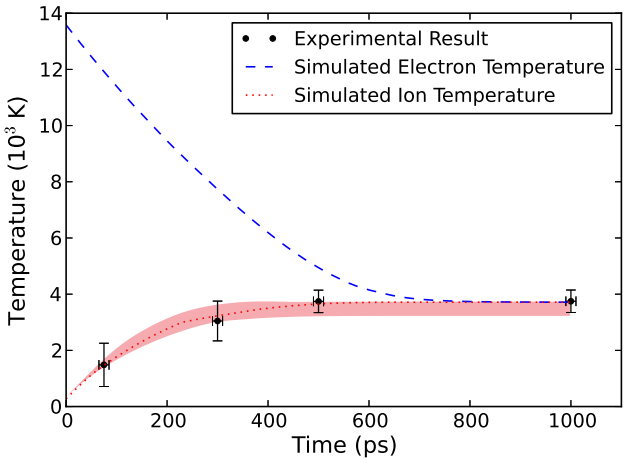

Figure 3.12: Time evolution of the electron (blue dashed line) and ion (red dotted line) temperatures using a coupling constant $g = 0.2 \times 10^{16}$ W K^{-1} m^{-3} and source term $S_e = 7$ J mm^{-3}. The points represent the experimentally measured ion temperature. The shaded region represents varying the source term from 6 and 8 J mm^{-3}.

radiation (see Fig. 3.10). The X-rays diffract off the graphite layer at a Bragg angle of 13.3° onto an image plate detector placed 100 mm away. The magnification of the set-up was 38. The copper foil is tilted edge-on with respect to the sample in order to reduce source broadening. As before, the temperature of the graphite ions is related to the intensity of the Bragg scattered X-rays via the Debye-Waller effect, see Eq. (3.3). Fig. 3.11 shows the decrease in the measured intensity of the scattered X-rays across the surface of the graphite sample for two different delays. As the electrons transfer their energy to the ions via ohmic heating, the ion temperature increases, and a more pronounced reduction in the diffracted intensity becomes apparent in the data.

3.4.2.2 Results

As before, the experimental data showing the increase in ion temperature over time can be fitted with a simple two temperature model. Again, the heat capacities of the electrons and ions were obtained from density functional theory calculations, see appendix E [150]. The transfer rate is set by the coupling constant g. This method allows the complexity of the physical system to be contained within a single parameter. The coupling constant is a quantity which is difficult to estimate from first principles as it depends on the interaction dynamics of the electron and phonon subsystems. Within the two temperature model, g and S_e are chosen as a fitting parameters such that the predicted ion temperature in the graphite sample reproduces

the measured reduction in the Bragg peak intensity. The best fit, by matching the ion temperature at the centre of the heated region, is found to be a coupling constant of $g = 0.15 - 0.25 \times 10^{16}$ W K^{-1} m^{-3} and a source energy of $S_e = 6 - 8$ J mm^{-3}, as shown in Fig. 3.12.

3.4.2.3 Fitting Data to Hybrid PIC Code

In addition to fitting the two temperature model to the experimental ion temperature the source term in the TTM can be calculated from the Ti K-shell emission. The high energy electrons that are accelerated through the solid target also produce intense X-ray and VUV emission, primarily through bremsstrahlung radiation and K-shell ionisation. The resulting Ti K-shell line emission was collected with an absolutely calibrated, toroidally bent spectrometer [132, 216] and used to infer the single shot properties (spectral temperature, angular divergence and absorbed laser energy) of the fast electron population [39, 76]. This on shot diagnostic was a significant improvement over the previous proton based experiment. The fast electron properties were achieved by modelling the energy deposition throughout the sample using the 3-D hybrid code ZEPHYROS [107]. The ZEPHYROS code is a 3D macroparticle based hybrid code developed by A. P. L. Robinson for the study of electron transport in dense plasmas. The fast electron population are treated as a collection of macro particles as is typical in a particle-in-cell code, while the background electron and ions are treated as a two temperature fluid. The code currently implements many features, such as Bremsstrahlung cooling of the background electrons, electron-ion energy exchange, creation and evolution of magnetic fields and various EOS models for both plasma and solid conditions. Recently, the ZEPHYROS code was upgraded to calculate the K_α photon emission rate due to fast-electron-induced K-shell excitation using the algorithm developed by A. G. R. Thomas [190]. The code currently outputs the rate of production of K_α photons for each element of the simulation in units of photon number per second per volume. By taking into account radiation transport, the detector solid angle and by integrating across both the depth of the sample and along a single spatial direction at the back of the target it is possible to obtain the linear intensity of photons on the detector. This number is directly comparable with experimental results obtained from an absolutely calibrated imaging spectrometer.

A 2.5×10^{18} W/cm^2 laser with a 30 μm radius flat-topped spot incident on a 200 micron Ti target for 0.7 ps was simulated within the ZEPHYROS code. The simulation contained 400,000 fast electron macroparticles distributed thermally at some characteristic temperature. The simulation was carried out in a 20x30x30 box

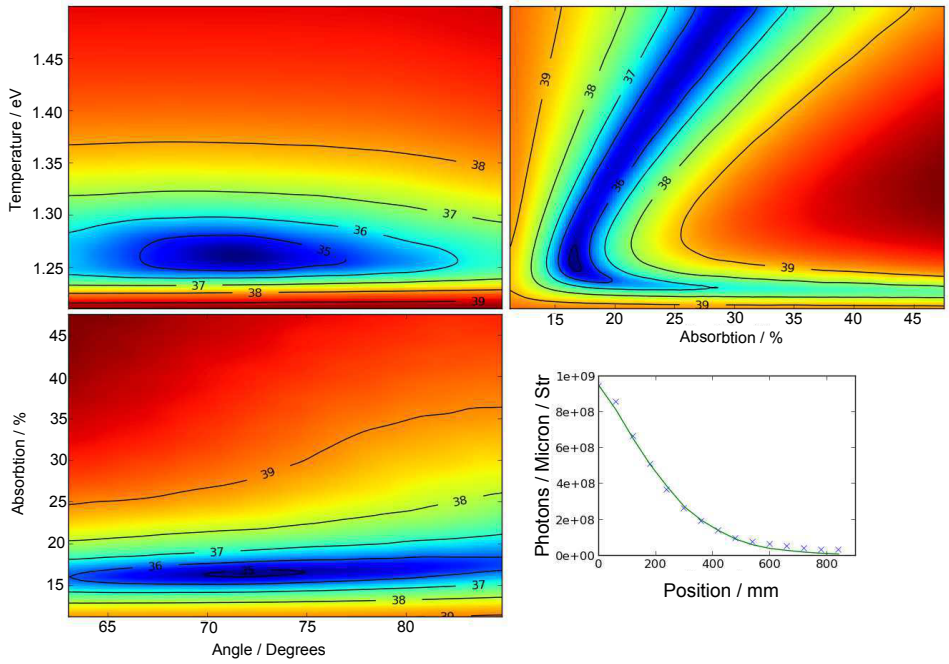

Figure 3.13: Comparison of linear K_α spectrum obtained from the ZEPHYROS hybrid code with the experimentally measured result. Plotted is the least-mean-squares fit against the fast electron angle, spectral temperature and total energy. The experimentally measured K_α spectrum is plotted along-side the output from ZEPHYROS for a 15%, 1.25 MeV fast electron spectrum with a divergence angle of 78°.

representing a 200x1800x1800 micron sample. It was run for a time of 6 ps and the K_α production was output at 0.2 ps steps. The resistivity is handled within a reduced Lee-Moore model [99]. Each simulation was run on the SCARF lexicon cluster operated by the central laser facility (CLF). A single run required a time of approximately 300 seconds, including post-processing, and operated on a single core. A total of 18,000 simulations were carried out representing a range of fast electron characteristics. This range covered a 3D parameter space of size 30x30x20 representing fast electron spectral temperature (1.2−1.5 keV), laser energy absorption (10−50 %) and FWHM divergence angle (63−86 degrees). The simulation result was then compared with the experimentally measured K_α spectrum.

The figure of merit used for comparison between the simulated spectra and the experimental spectra is achieved using a least mean squares fit between the experimental data and simulation. Here N is the number of experimental data points, x the position across the target surface and I the linear intensity of K_α photons hitting the detector. The minimum of this function represents the conditions where the

simulated spectra best matches that observed experimentally,

$$\phi = \frac{1}{N}\sum_{x}^{N}\left(I_{\text{simulation}}(x) - I_{\text{experiment}}(x)\right)^2 . \tag{3.14}$$

This function was minimised when the fast-electron temperature was set to ∼1.2 keV, the angle to ∼72 degrees and the absorption of laser light to ∼15%. Plotted in Fig. 3.13 is the log of this function plotted with one of the electron distribution variables held constant and the other two varied. It can clearly be seen that there exists a point in the three dimension space where the figure of merit is minimized. This suggests that these three variables are somewhat decoupled and that this measurement allows all three to be determined to within some degree of accuracy. Also shown in Fig. 3.13 is the experimentally measured K_α spectrum plotted alongside the output from ZEPHYROS for a 15%, 1.25 MeV fast electron spectrum with a divergence angle of 78°.

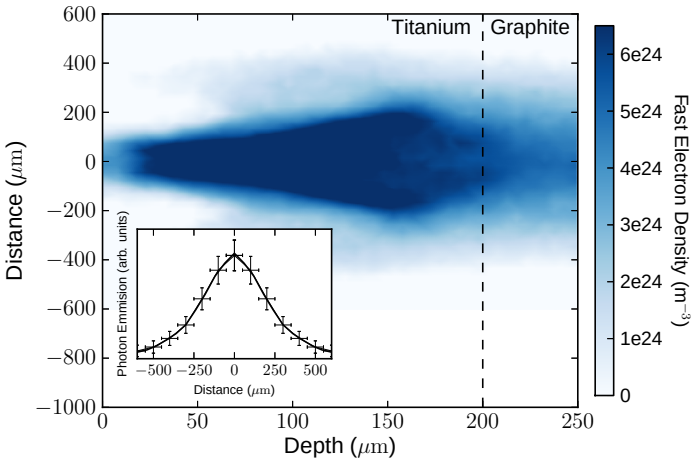

Figure 3.14: Simulation results showing the fast electrons from the laser interaction heating the graphite sample. These results are produced from the fast electron transport code ZEPHYROS. The fast electron density (units $1/m^3$) is shown at time=0.8 ps. The insert shows the Ti-K_α emission from the simulation and the experimental measurement using an absolutely calibrated imaging spectrometer.

In this way, the initial fast electron population is varied until the predicted K-shell emission from the simulation matches the experimental result. The source term for the two temperature model found through this method is $S_e = 6.9$ J/mm^3 which is in agreement with the value found though fitting the data directly. With this spatially dependent source term from ZEPHYROS we can plot the predicted intensity drop across the back surface at different times after heating, see Fig. 3.11. We find good

agreement between simulation and experiment for a coupling constant g=0.2 $\times 10^{16}$ W K^{-1} m^{-3}.

Because of the complexities associated with short pulse laser irradiation and fast electron transport, the assumption that the heating is uniform and instantaneous should be discussed. The intense fast electron current in the target produces large magnetic and electric fields that can complicate the analysis through magnetic focusing, the formation of resistive current loops, and large-scale instabilities arising from a varying resistance with temperature. As shown in appendix G, these effects remain small in our experiment, and thus the assumption of uniform and instantaneous heating is sound. This is supported by the measurement of the Ti-K_α emission from the rear surface of the sample, showing a smooth intensity distribution of the line emission across the transverse direction.

As before, in order to compare with previously published data, we use the dimensionless parameter λ. In this work a value of $\lambda \sim 0.03$ is obtained. Again this value is considerably closer to room temperature graphite [101, 117] ($\lambda \lesssim 0.2$) than to values reported for metals and plasmas. However, our result is almost an order of magnitude less, suggesting the relaxation pathway is inhibited by the highly non-equilibrium conditions. Near room temperature lower λ values in semimetals are attributed to a small DOS at the Fermi energy, an argument which does not hold here due to the high electron temperatures ($T_e \sim 15,000$ K). This suggests a more complex energy pathway in warm dense graphite which acts as a barrier to relaxation.

The results presented here are in good agreement with the energy relaxation timescale inferred from the proton heated experiments suggesting that energy equilibration rate measured here is independent on the details of the heating mechanism.

There is still much debate over the coupling rate in semimetal materials such as graphite. Current work focuses on the coupling between the electrons and COPs at frequencies of $\omega_{\mathrm{COP}} \approx 200$ meV. This pathway is believed to allow for a fast energy flow on time-scales less than 100 fs, although the decay of these excited phonons occur over significantly longer times. In experiments using laser heating, the possibility that these optical phonons are excited directly by the pump laser cannot be dismissed[101]. Through applying heating with an energetic proton or electron beam, we eliminate direct COP generation by the heating source. Additionally, we probe lower energy phonons with a component of motion out-of-plane through the measurement of the 002 Bragg peak intensity. As such we expect no contribution to intensity reduction from COPs [177]. While our method does not discriminate between direct coupling and

coupling via COPs, the low relaxation rates observed here suggest either saturation of the COP pathway or lower coupling via more direct pathways.

Due to the large electron temperature ($T_e \approx 15,000$ K) achieved, it may be interesting to compare the result found here with data obtained in other high temperature systems in the WDM region which might be particularly insightful as the coupling coefficient is expected to vary strongly with electron temperature [120]. The experimental difficulties in creating and measuring temperatures within highly non-equilibrium dense systems means that only a few data points exist; none prior to this work for graphite or carbon. However, experiments performed on warm dense silicon and aluminium samples also suggest a very low coupling parameter [33, 163] of the order of 10^{16} W K^{-1} m^{-3}. To explain these experiments, it was proposed that the effective electron-ion interaction is suppressed by virtue of a dynamical coupling of electron and ion modes discussed earlier. These coupled ion modes mainly occur at frequencies $\omega \ll k_e c_s \simeq 200$ meV, where k_e is the inverse of the Thomas-Fermi screening length and $c_s \sim (k_B T_{\mathrm{ele}}/M)^{1/2}$ is the isothermal sound speed (M here is the carbon ion mass) suggesting that very low frequency excitations have an important role in determining the pathway and the bottleneck in the energy relaxation. To interpret our experimental results, we have to assume that frequencies $\omega \ll \omega_{\mathrm{COP}}$ play the major role in the electron-phonon energy exchange. Such processes may thus be more general than previously believed and, as indicated by these experiments, occur in any strongly driven two-temperature system.

3.5 Temperature Relaxation in Gold

3.5.1 Introduction

This section moves away from investigating electron-ion equilibration in graphite and will describe experimental results that show the calculation of the electron-phonon equilibration rate in gold. In particular this section will describe a technique that can be performed on smaller table-top based laser systems and does not require the large-scale facilities discussed above. The electron-phonon coupling within gold is an important property that determines or modifies many electronic properties such as electronic and thermal conductivities (with superconductivity as the premier example [18]), the magnetic susceptibility, the available electron energies, and thus, the EOS [13]. Accordingly, this quantity is needed for a number of applications in nano-technology [109], material science [205], laser ablation [20], and energy production by means of ICF [14].

Exciting a thin metal foil with a short-pulse laser is a well-established procedure to create non-equilibrium systems in order to study equilibration rates. However, contrary to previous studies, we have combined this method with full MD simulations of the entirety of the system, at least in a single dimension. The value obtained agrees with values reported in similar experiments, but, crucially our analysis indicates that other factors may also determine the position of those peaks which are not directly related to the energy relaxation time. We therefore believe that our results give a more reliable estimate of the equilibration time than previous work. This result confirms that the energy relaxation in gold is a fast process in the bulk as well as on the surface of the sample. The fact that different experimental methods yield very similar values for the electron-phonon coupling constant strongly raises the confidence in this result at low excitations. The addition of the MD analysis suggests that this work could in the future be extended to cover the more difficult highly non-equilibrium regime mentioned earlier.

A direct way of investigating electron-phonon coupling, or more generally electron-ion energy transfer, is to set-up a non-equilibrium situation and observe the equilibration of the system towards a state with a common temperature. Since optical lasers can be considered to directly interact with only the electrons in the sample, the electron subsystem contains a greater amount of energy after the heating process. After an ultra-fast thermalisation within the electron subsystem [64, 140], the energy then flows into the lattice by excitation of phonons, and ultimately ion-acoustic waves that heat the background ions [145]. This process is relatively slow, and electron and ions may have unequal temperatures for times that long exceed the laser pulse duration [209]. The evolution of the electron and phonon temperatures is thus a complex process which depends on many factors such as initial temperatures, crystal structure, defects and scattering properties of the sample [8, 120].

Although energy relaxation between the electron and ion subsystems has been investigated in many studies both experimentally and theoretically, the process is not well understood. While experiments near to equilibrium [145] show good agreement with standard theoretical predictions [120], other experiments with high excitation densities or a more complex material structure have demonstrated large deviations with relaxation times longer than predicted [118, 209]. Such deviations are typical for strongly heated, fluid systems [33, 35, 144, 163, 206] where the energy transfer does not evolve through electron-phonon coupling but through direct two-particle scattering or ion acoustic modes. Although theoretical models considering the collective behaviour

of these coupled system show similar effects [47, 77, 200], the predictions do not agree with the small amount of experimental data available.

Here, we investigate electron-phonon coupling in weakly driven gold samples, adding more data for non-equilibrium systems with low excitations. Indeed, our systems are heated only slightly above room temperature requiring precise determination of the ion temperature. This is done through the determination of the response of the ion lattice via X-ray Bragg scattering. The time-dependent lattice constant obtained can then be related to the lattice temperature and, thus, the energy received from the electrons. This work differs from previous experiments by Nicoul *et al.* [145], where a similar experimental technique had been employed, through the utilisation of large scale non-equilibrium MD simulations to analyse the lattice response. These simulation contain up to ∼115,000 atoms and are able to model the full depth of the gold samples. It is this capability to fully capture the acoustic modes of the system which suggests that MD would be ideally suited to model systems with higher excitation densities.

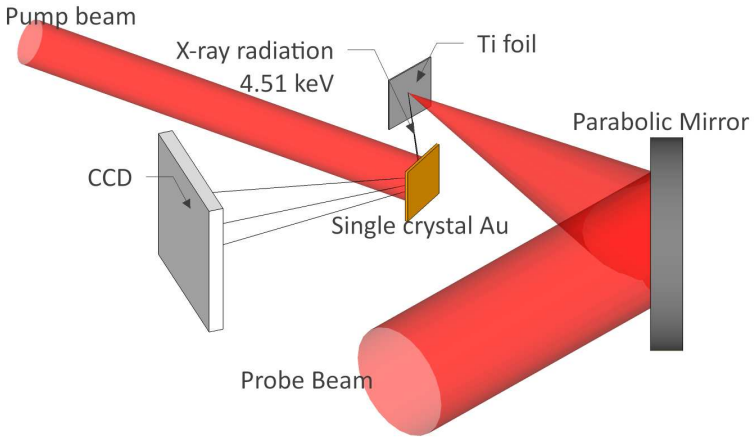

Figure 3.15: Schematic showing the experimental set-up. The 50 fs, 40 mJ, 800 nm laser is split into two arms. The first arm is focused onto the gold foil to rapidly heat the conduction electrons in the sample while the second arm passes through a delay stage and then drives the Ti-K_α transition in a thin Ti foil in order to probe the lattice parameter. The movement of the diffraction line due to the heating is imaged onto a CCD placed 10 cm away.

3.5.2 Experimental Set-up

The experiment was performed using an ultra-fast Ti:sapphire laser with wavelength centred at 800 nm, 50 fs duration, and delivering ∼40 mJ per pulse. The laser was

used in single shot mode, and split into two equal arms to achieve a pump-probe geometry, as shown in Fig. 3.15. The error on the delay stage was determined from the precision of the micrometer stage to be less than 1 ps. One arm (the pump) was focused to a spot size of approximately 3 mm onto a 200 nm thick gold nanofoil [5]. This set-up leads to a laser fluence incident on the sample of 0.28 J/cm^2. Taking into account the reflectivity of gold at 800 nm, we estimate the energy flux absorbed by the target to be $\sim$0.01 J/cm^2. This corresponds to an overall increase in the energy of the sample on the order of $\sim$1 eV/nm^3. The gold foil is grown on a mica substrate on the opposite side to the laser beam, whereas the laser side of the gold film only faces the vacuum and can expand freely.

The second arm (the probe) of the laser pulse was sent through a delay stage with difference in time of arrival of the two arms ranging from $\Delta t = -5$ ps to $\Delta t = 250$ ps (where negative values means that the probe was fired earlier than the pump beam on the gold foil). The probe beam was focused by a f/10 parabola to a spot size of 50 μm onto a 12.5 μm thick Ti foil to generate short pulse line radiation at 4.5 keV. Both the pump and probe lasers were incident normal to the foil and the X-rays intercepted the gold foil at the Bragg angle (θ_B=35.9°). A schematic of the experimental set-up is shown in Figure 3.15.

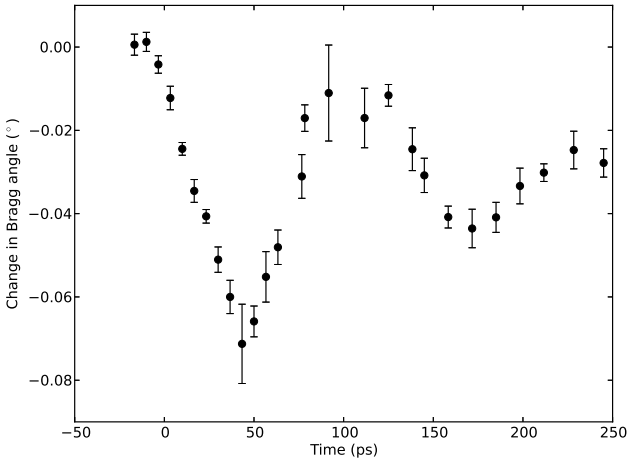

Figure 3.16: Change in diffraction angle from the gold nano-foil plotted against delay time. The data has been shifted in time to approximate the position of t=0 ps.

The X-ray line radiation was scattered coherently from the gold nano-foil and imaged onto a 2 cm × 2 cm charged coupled device (CCD) array with 13.5 μm pixel

[5]The gold foil is commercially available from PHASIS (Switzerland) and has been epitaxially grown onto a mica muscovite substrate.

size, placed at a distance of 10 cm from the sample. The diffraction angle, and hence the position of the line on the CCD chip, is related to the inter-planar distance in gold through Bragg's law. Thus, any movement of the atoms such as thermal expansion can be seen through translation of the diffraction line.

For each shot a Gaussian profile was fitted to the middle of the diffraction line and the centre used to calculate the diffraction angle. Multiple shots were taken for each pump-probe delay and the error bars were estimated using one standard deviation from the average. For delays between -5 ps and 40 ps each condition was repeated 12 times, for all other delays an average of 6 shots were used. The experimentally obtained change in diffraction angle including standard deviation in the error bars is shown in Fig. 3.16.

3.5.3 Modelling the Lattice Response

Again the TTM describing the energy flow between the electron and phonon subsystems is used. Given the large laser spot size compared with the thickness of the gold foil, we can treat the heating of the sample as being one dimensional. Furthermore, the source term in Eq. (3.8) does not depend on a spatial coordinate and, thus, does not take into account the finite penetration depth of the laser. This is due to the ballistic nature of the hot electrons which causes the target to equilibrate spatially across its depth within a picosecond after laser irradiation [27, 105, 187]. As the energy is transferred from the hot electron population to the ions forming the lattice, the crystal expands and the lattice parameter increases. From Bragg's law, the position of the diffraction line can be related to the expansion of the sample. If the equilibration rate is quick (less than a few 10s of picoseconds) the gold foil will rapidly expand and oscillate around some new mean lattice constant. If the rate is slower the sample will slowly expand until it reaches the new lattice constant. In our experiment we expect the former scenario to apply (see for example reference [166]).

The time-scale of temperature equilibration in this experiment is considerably faster than the proton and electron heated graphite experiments in sections 3.4.1 and 3.4.2. As such the applicability of the TTM must be evaluated. The TTM requires that both the electron and phonon subsystems are in local equilibrium, that is the electron-electron scattering maintains a Fermi-Dirac distribution with a characteristic temperature T_e and phonon-phonon scattering maintains a Bose-Einstein distribution with a characteristic temperature T_i [1]. The electron-electron thermalisation time can be estimated from the relation $\tau_e \approx \hbar E_F / 4\langle E \rangle^2$ where E_F is the Fermi energy and $\langle E \rangle$ the mean electron energy [54]. For the gold nanofoil used here, $E_F = 5.53$ eV.

For an average electron energy of $\langle E \rangle = 0.086$ eV, which corresponds to an electron temperature of 1000 K, the electron-electron thermalisation time is of the order of 0.25 ps. Given the laser fluence in this experiment we expect electron temperatures of 1000 K to be readily accessible [54]. The electron-electron energy equilibration, spatial equilibration and laser pulse duration are all much less than the time-scale of interest in this work and hence it is reasonable to approximate the source term in the TTM to be instantaneous, *i.e.*, $S_e(t) \approx S_e\delta(t)$. Indeed, in previous experiments on thin gold films of a similar thickness to those used here the electron distribution was found to be Fermi-Dirac-like after 0.8 ps [54]. Therefore, a full non-equilibrium treatment of the electron subsystem, which has been shown to modify the energy transfer to the lattice [140], is not necessary here and we can rely on temperature estimates.

On the contrary, the phonon-phonon thermalisation time for gold is much longer, and it has been estimated theoretically to be of the order of tens of picoseconds. Hence the phonon system is expected to be out of local-equilibrium on the time-scales probed here. However, since the change in phonon temperature found in our experiment remains small (*i.e.*, a 10% increase from 300 K to ∼330 K), we can still describe the phonon gas in terms of a Bose-Einstein distribution at 300 K plus a small number of out-of-equilibrium phonons [54], and assume that the additional excitation of the phonon system results in negligible changes of the energy transfer during equilibration. The evolution of the electron and ion temperatures in the sample is dominated by the electron-phonon coupling, and this occurs on time-scales of the order of a few picoseconds.

In order to understand the details of the equilibration process, we have modelled the gold foil in a classical MD simulation. Molecular dynamics is a powerful tool that has had considerable success in describing the lattice dynamics in numerous laser-solid target interactions [106]. Here, we vary the rate at which energy is transferred to the ions to match the experimental results. This is made possible by the one dimensional nature of the experiment. Classical molecular dynamics simulations are performed in the LAMMPS package [156] within a micro-canonical ensemble. The simulation used 114,916 atoms in a 3.98 nm × 2.30 nm × 218 nm box which is equal in size to 3 × 3 × 300 gold crystal unit cells. The small cross section preserves the one dimensional nature of the problem, but may not fully capture phonon modes with large transverse motion. The simulation box was split into 7 nm of vacuum and 211 nm of gold with the crystal lattice orientated along the (111) plane.

Each simulation was run with a 1 fs time step and the total number of time steps in each simulation was 300,000. The simulations were run for 50,000 time steps prior to the application of the laser heating to ensure that the crystal was initially at rest. A viscous damping factor, γ, is applied to the gold lattice in order to account for the energy loss to the mica substrate. This factor allows the adjustment of the speed with which the gold loses energy.

The gold atoms are modelled using an EAM potential as discussed in chapter 2.3.3. Details on the exact potential can be found in Ref. [182]. This potential accurately predicts the lattice constant and bulk modulus of gold to within 2% and we therefore expect to accurately capture the acoustic dynamics. The MD simulation was run by accounting for the energy relaxation between electrons and ions via the TTM. We utilise an exponential function as an approximate solution to the TTM (equations (3.8) and (3.9)) for a given initial electron temperature. That is, energy is deposited into the ion subsystem by exponentially decreasing amounts with a time constant equal to $\tau = C_e/g$, where g is the electron-phonon equilibration constant [94]. We take the electron heat capacity to have a value of $C_e = 67.6T_e$ J m^{-3} K^{-2} [120]. This solution to the TTM assumes that the electron and lattice thermal conductivities are low enough as to not transport heat laterally in the target over the time-scales of the experiment. For gold in 250 ps the characteristic length over which heat is conducted is $(Kt/C)^{\frac{1}{2}} = 200$ nm, considerably less than the 3 mm heated spot. Finally, the predicted diffraction line is obtained from the Fourier transform of the atom positions at each time-step. The peak position in reciprocal space is related to the diffraction angle by $k = 4\pi(E_0/hc)\sin(\theta/2)$ where E_0 is the energy of diffracted X-rays and k the scattering wave-number.

3.5.4 Fitting Parameters from Molecular Dynamics

As electrons are heated by the laser, a sound wave is launched into the bulk of the sample. The oscillations shown in the diffraction peak position for delay times $\Delta t \gtrsim 40$ ps are related to reverberation of the sound wave between the sides of the sample. This process occurs on time-scales longer than the energy equilibration between electron and ions ($\tau \lesssim 10$ ps), and it can thus be used in order to infer the long-term mechanical response of the gold due to the short-time perturbation caused by the laser heating.

There are four free parameters available in the numerical simulation which must be varied in order to fit the data for $\Delta t \gtrsim 40$ ps. These are the thickness of the gold, l, which is known with $\pm 20\%$ accuracy, the total energy absorbed into the

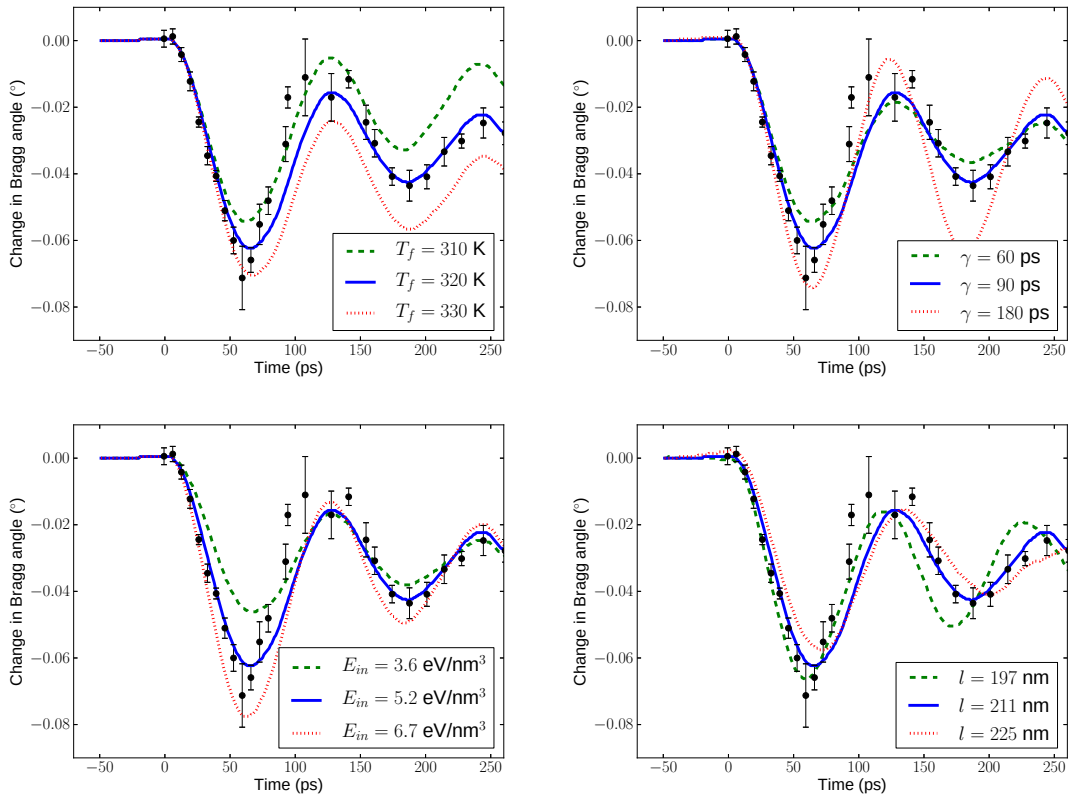

Figure 3.17: Change in diffraction angle from the gold nano-foil compared to results from MD simulations. The effect of changing the final temperature of the lattice (top-left); the damping coefficient (top-right); the energy absorbed by the lattice per nanometre cubed (bottom-left) and the thickness of the gold (bottom-right) on the diffraction angle plotted against time. The solid line represents the best fit, while the dashed and dotted lines are under and over-estimates, respectively.

gold target per nanometre cube, E_{in}, the final temperature of the lattice, T_f, and the damping coefficient, γ. Figure 3.17 shows the change in predicted behaviour associated with varying each of these parameters. The effect of the choice of a different final temperature is to change the equilibrium lattice spacing at late time, while the damping coefficient controls the time over which the lattice attains this new configuration. The energy absorbed determines primarily the depth of the first trough as well as the amount of ringing seen about the equilibrium lattice spacing. Lastly, the gold thickness alters the period of the oscillations. Our best fit values for these parameters are: $\gamma = 90$ ps, $T_f = 320$ K, $E_{in} = 5.2$ eV/nm^3 and $l = 211$ nm.

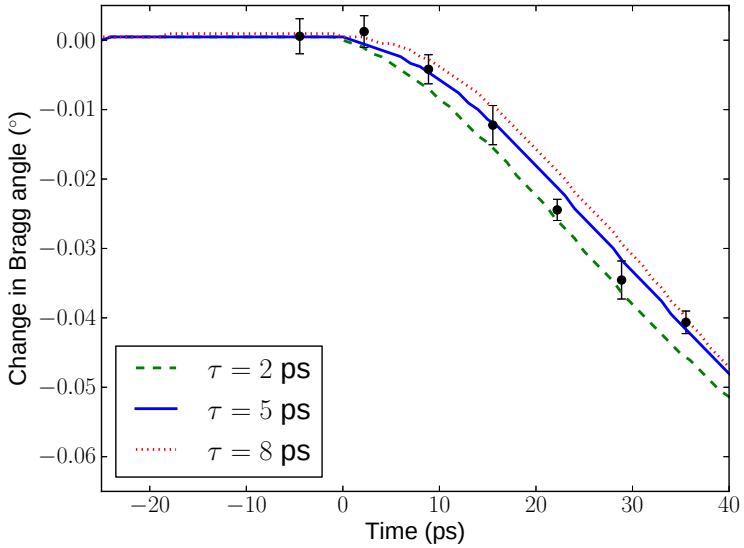

Figure 3.18: The variation of τ in the simulation. The solid line represents the best fit ($\tau = 5$ ps) while the dashed and dotted lines are under and over-estimates ($\tau =$ 2 ps, 8 ps) respectively. We have used $\gamma = 90$ ps, $T_f = 320$ K, $E_{in} = 5.2$ eV/nm^3 l = 211 nm in all cases.

3.5.5 Electron-Ion Coupling Constant

Once the long-time behaviour has been determined, the simulation is used to fit the short-time behaviour ($\Delta t < 40$ ps), which is strongly determined by the electron-phonon coupling parameter (g) in the TTM. In the simulations we have varied the energy relaxation time, τ, to best fit the data, as shown in Fig. 3.18. We find a value of $\tau = 5 \pm 3$ ps. This value agrees with reported data in a similar experiment [145] where it was inferred by observing the shift in position of the peaks due to acoustic reverberation in the sample. However, our analysis indicates that other factors (in particular the energy loss to the mica substrate) may also determine the position of those peaks which are not directly related to the energy relaxation time (see Fig. 3.17).

3.5.6 Conclusions

The determined value for τ leads to an electron-phonon equilibration constant of $g = 2 \pm 1.2 \times 10^{16}$ W m^{-3} K^{-1}, a value which is in close agreement with previous studies. Table 3.1 contains a comparison of electron-phonon coupling constants based on a variety of experimental and theoretical techniques. This result agrees well with previous values, confirming that the energy relaxation in gold is a fast process in the bulk as well as on the surface of the sample. The fact that different experimental

methods yield very similar values for the electron-phonon coupling constant strongly raises the confidence in this result at low excitations. This result agrees well with previous values, confirming that the energy relaxation in gold is a fast process in the bulk as well as on the surface of the sample. The fact that different experimental methods yield very similar values for the electron-phonon coupling constant strongly raises the confidence in this result at low excitations.

3.6 Conclusions on Temperature Relaxation

In conclusion electron-phonon equilibration rates in both gold and graphite samples have been measured experimentally. The graphite samples were subjected to higher excitation densities and showed significantly reduced electron-ion coupling compared with room temperature samples and with idealised plasma models. These experiments conclusively show the need for improved models for energy relaxation in this warm dense regime, either through theoretical models involving coupled ion modes or numerical modelling such as Monte Carlo or PIC simulations. Moreover, we can expect that such low equilibration times in dense plasmas could lead to changes in other other transport quantities such as the optical conductivity and opacities, which may have a number of important implications ranging from the laser processing of materials and ICF [143] to the cooling rates of white dwarf stars and neutron stars [40, 98].

Fig. 3.19 shows the results of the two experimental campaigns alongside the separate theories for temperatures relaxation. As discussed previously the results from the Landau-Spitzer technique, although seemingly correct, are based upon assumptions that are certainly invalid in this regime. Instead, it can be clearly seen that the coupled mode theory most closely matches the experimental data, predicting a

Exp. Method	τ	g $/10^{16}$	Reference
Bragg Peak Shift (MD)	5.0 ± 3	2.0 ± 1.2	this work
Bragg Peak Shift (Acoustic)	5.0 ± 0.3	1.6 ± 0.1†	[145]
Bragg Peak Intensity	4.7 ± 0.6	1.8 ± 0.2†	[119]
Surface Expansion	1.5 ± 1.0†	1.6 ± 0.6	[213]
Surface Reflectivity	4.0 ± 1.0†	2.2 ± 0.3	[94]
Ab-Initio Calculation		2.5	[120]

Table 3.1: Comparison of electron−phonon coupling times in gold reported in the literature together with the result from this work. The time constant τ is given in units of ps and the coupling constant g is given in units of W m^{-3} K^{-1}. Values marked with a † have been inferred from $\tau = C_e(T_e)/g$.

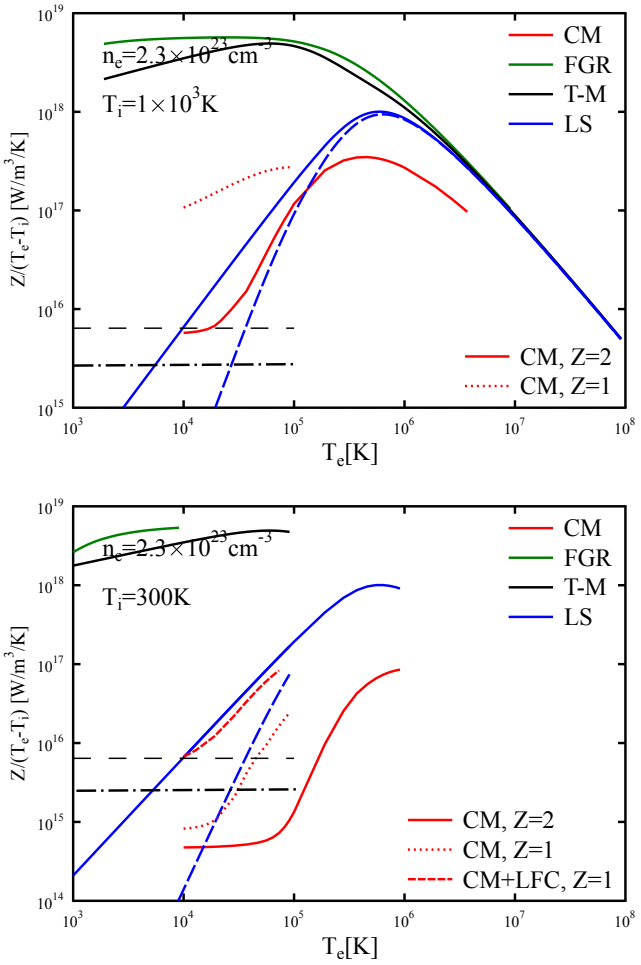

Figure 3.19: Theoretically obtained electron-ion relaxation rates in solid density graphite with ion temperature T_i=1000 K (top) and T_i=300 K (bottom). Shown are results from Landau-Spitzer (solid blue), Brysk (dashed blue), T-Matrix (solid black), Fermi's golden rule (solid green) and coupled mode with ionisation Z=1 (dotted red) and Z=2 (solid red) [196]. The experimental values measured in chapter 3 via proton heating (black dashed) and electron heating (black dashed-dotted) are also plotted for comparison.

lower energy transfer rate at lower temperatures. An interesting feature to note here is the reduction in equilibration rate between the subspecies as the ion temperature is reduced, this highlights further the effect of ion-ion structure and long-range order on equilibration rates. These two experiments contribute vital data points the few experimental measurements of temperature relaxation in the HEDP regime. This body of evidence demonstrates that extreme care must be taken when inferring quantities which depend on local thermodynamic equilibrium, such as temperature and pressure, when conducting a dynamic experiment. This is particularly true in graphite

where the ion-ion structure coupled with a highly non-equilibrium sample results in a bottle-neck that only the coupled mode theory comes close to correctly describing.

In the gold samples, which were closer to equilibrium, the results obtained were in agreement with those predicted from traditional solid state calculations. This finding, in combination with the discrepancies for higher energy input both for solids and fluids, further points towards changes in the relaxation behaviour in strongly driven systems. This work highlights the possibility to study energy relaxation processes in bulk samples through large-scale MD simulations and could be particularly successful at describing the complex ion-ion correlations [110, 123] which make experiments with higher excitation densities difficult to describe [77, 200].

Chapter 4

Density Functional Theory - Molecular Dynamics

4.1 Introduction

The experimental results from the highly non-equilibrium graphite created through heating with an intense proton beam (see section 3.4.1) and electron beam (see section 3.4.2) both suggest a very low coupling parameter of the order of 10^{16} W K^{-1} m^{-3}. To explain these experimental results, it was proposed that the effective electron-ion interaction is suppressed by virtue of a dynamical coupling of electron and ion modes [47, 48, 77, 200]. As discussed earlier, in the coupled mode theory of temperature relaxation the interaction potential between species V_{ei} is screened by the dielectric function which itself can be related to the dynamic structure factor of the electrons through the fluctuation dissipation theorem. Hence, ion dynamics and long range order have a significant impact on the subsystem energy transfer rates.

Models for the dynamic ion motion present in a dense plasma has been of enormous interest to the community for many decades and many now exist. In this chapter we present, for the first time, calculations of the ion-ion dynamic response that goes beyond approximate approaches used previously [78, 86, 98, 112]. While a number of different theoretical approaches have been proposed to describe $S_{ii}(k, \omega)$, where, in the case of an isotropic system, we can assume that the structure factors depend only on the absolute value $k \equiv |\mathbf{k}|$, none to date have used self-consistent quantum simulations. Additionally, the methods used here can describe large systems both spatially and temporally and hence capture accurately the low frequency ion response.

4.2 Density Functional Theory

The primary simulation technique used to calculate the ion component of the DSF for WDM is to to take the spatial and temporal Fourier transform of the ion positions taken from the output of a MD simulation. Appendix B contains a detailed description of the graphical code implemented in python that was used in this work to perform the large-scale Fourier transforms. However, many questions arise relating to the applicability of a classical simulation and standard pair potential[1] to describe a system where strong correlations and quantum degeneracy becomes important.

In order to go beyond classical mechanicals and traditional MD we utilise DFT to calculate the inter-atomic potential *on-the-fly*. DFT is a technique whereby an approximate solution to the ground state energy of a many body system can be found through solving the Schrödinger equation[2],

$$\hat{H}\phi = E\phi\,, \tag{4.1}$$

where the total energy operator can be written in terms of the kinetic energy, electron-nucleus and electron-electron energy operators respectively,

$$\hat{H} = \hat{T} + \hat{V_{ne}} + \hat{V_{ee}} = -\frac{1}{2}\sum_{i}^{N}\nabla_i^2 + V_{ne} + \sum_{i<j}^{N}\frac{1}{|\mathbf{r}_i - \mathbf{r}_j|}\,. \tag{4.2}$$

The average energy of a system in state ϕ can then be written as,

$$E[\phi] = \frac{\langle\phi|\hat{H}|\phi\rangle}{\langle\phi|\phi\rangle}\,, \tag{4.3}$$

where the ground state energy E_0 is that which minimises this value with respect to all allowed wave functions, $E_0 = \min_{\phi} E[\phi]$. Hence, the Schrödinger equation can equivalently be written in terms of the variational principle, $\delta E[\phi] = 0$, or if it is minimised with the normalisation constraint $\langle\phi|\phi\rangle = 1$ the minimisation becomes,

$$\delta[\langle\phi|\hat{H}|\phi\rangle - E\langle\phi|\phi\rangle] = 0\,, \tag{4.4}$$

where E is the Lagrange multiplier.

[1]Standard pair potential here is taken to mean a screened coulomb (Yukawa) with and without additional SRR effects. A potential of this type is typically used for describing weakly coupled plasmas.

[2]DFT began with solving the time independent, non relativistic Schrödinger equation within the Born Oppenheimer approximation. However, time dependent DFT is now commonly used when looking at electronic transitions in atoms.

While solving this equation is possible, it is exceptionally difficult for all but the simplest of systems. DFT is a theory which allows the complex N-electron wave function ϕ to be replaced with simply the electron density. Research began by investigating the trial system of a homogeneous electron gas by Thomas and Fermi in the 1920s. They were able to extract (for a system of non-interacting electrons) the dependence of the kinetic energy on the density of the system,

$$T_{tf}[\rho] = C_F \int \rho^{5/3}(\mathbf{r}) d\mathbf{r}\,, \tag{4.5}$$

and if only the classical electrostatic energies are taken into consideration the total energy functional can be written as,

$$E_{tf}[\rho] = C_F \int \rho^{5/3}(\mathbf{r}) d\mathbf{r} - Z \int \frac{\rho(\mathbf{r})}{\mathbf{r}} d\mathbf{r} + \frac{1}{2} \int \int \frac{\rho(\mathbf{r}_1)\rho(\mathbf{r}_2)}{|\mathbf{r}_1 - \mathbf{r}_2|} d\mathbf{r}_1 \mathbf{r}_2 \tag{4.6}$$

which under the constraint that $N = \int \rho(\mathbf{r}) d\mathbf{r}$ where N is the number of electrons in the system can be solved through the constrained minimisation of,

$$\delta\{E_{tf}[\rho] - \mu(\int \rho(\mathbf{r}) d\mathbf{r} - N)\} = 0\,. \tag{4.7}$$

The Lagrange multiplier μ can be expressed as $\mu = (5/3)C_F\rho^{2/3}(\mathbf{r}) - v(\mathbf{r})$ in which $v(\mathbf{r})$ is the electrostatic potential due to the atom and the electron distribution. These equations can be solved with relative ease to obtain the ground state energy of a system. However, a seminal paper by Hohenberg and Kohn published in 1964 showed that the Thomas-Fermi theory is merely an approximation to a more exact theory which they called *Density Functional Theory* or DFT.

The underlying premise of DFT is based upon two theorems proved by Hohenburg and Kohn in their seminal 1964 paper. The first of these states that;

> "The electron density can uniquely define the external potential for a system (within an additive constant)"

A simple proof of this theorem is given in appendix H. Hence, for a given electron density a unique Hamiltonian is also defined. From this Hamiltonian it would then be possible to find all the wave functions describing the electronic density and thus the material properties of the sample. It can be summarised by saying that the energy of a system is a functional of the electronic density, or equivalently $E = E[\rho]$ [87, 148]. However, this is now an exact formalism rather than the approximate Thomas-Fermi model discussed above.

The second theorem developed by Hohenburg and Kohn states that;

"For any positive definite trial density such that $\int \rho dr = N$ then $E[\rho] \geq E_0$"

Together the two statements lead to a constrained minimisation problem similar to (4.7) however now the Thomas-Fermi energy functional has been replaced with a more general energy functional which Hohenberg and Kohn wrote as,

$$E[\rho] = T[\rho] + V_{ext}[\rho] + V_{ee}[\rho] \tag{4.8}$$

with kinetic energy (T), the external potential (V_{ext}) and the electron-electron interactions (V_{ee}). Of these three terms the external potential is trivial and given by the coulomb potential surrounding the ions in a system, while the kinetic energy and electron-electron interaction energy are much more difficult. Although Hohenberg and Kohn have shown that these universal functionals exist their explicit form is unknown, and so one must resort to approximations such as the Thomas-Fermi model. However, in 1965 Kohn and Sham developed a method to go beyond these simple approximations by introducing orbitals. They begin by writing the kinetic energy as,

$$T = \sum_{i}^{N} n_i \langle \Phi_i | -\frac{1}{2}\nabla^2 | \Phi_i \rangle \,, \tag{4.9}$$

where Φ_i and n_i are the spin orbitals and their respective occupation numbers. Hohenberg-Kohn theory states that the kinetic energy must be a functional of electronic density,

$$\rho(\mathbf{r}) = \sum_{i}^{N} n_i \sum_{s=1,2} |\Phi_I(\mathbf{r}, s)|^2 \,. \tag{4.10}$$

However, for an interacting system there are an infinite number of terms in these two equations. What Kohn and Sham did was to use two simpler forms of these equations. Namely setting $n_i = 1$. This gives the kinetic energy for a system of N non-interacting electrons which we will define as T_s.

The energy functional is re-written,

$$E[\rho] = T_s[\rho] + V_{ext}[\rho] + V_H[\rho] + E_{ec}[\rho] \tag{4.11}$$

where the functional E_{ec} is the exchange and correlation (XC) functional equal to $E_{ec} = (T[\rho] - T_s[\rho]) + (V_{ee}[\rho] - V_H[\rho])$. Here, V_H is the classical coulomb interaction between particles (known as the Hartree energy) while T_s is the energy associated with a system of non-interacting electrons. The E_{ec} term hence contains the 'difficult' part

of the calculation in that it contains the deviation from a non-interacting system of electrons.

This formalism gives rise to three Kohn-Sham orbital equations,

$$[-\frac{1}{2}\nabla^2 + v_{eff}]\Phi_i = \epsilon\Phi_i \,, \tag{4.12}$$

$$v_{eff}(\mathbf{r}) = v(\mathbf{r}) + v_H(\mathbf{r}) + v_{xc}(\mathbf{r}) \,, \tag{4.13}$$

$$\rho(\mathbf{r}) = 2\sum_{i}^{N/2}\sum_{s} |\Phi_i(\mathbf{r}, s)|^2 \,. \tag{4.14}$$

Kohn and Sham thus solve the Hamiltonian corresponding to a non-interacting reference system with an effective potential v_{eff}, in which the first term is the real external potential, the second term a purely coulomb potential and the final term the XC correction to the potential. As before this is a constrained minimisation problem, however the Lagrange multiplier is no longer the chemical potential but the effective potential. This set of equations is usually solved iteratively in a process known as *self consistent field calculation* during modern DFT calculations.

The kinetic energy term T_s is known as the Kohn-Sham kinetic energy and is defined exactly as,

$$T_s[\rho] = \min_{\Phi\to\rho} T[\Phi] \,, \tag{4.15}$$

where

$$T[\Phi] = \langle\Phi|\hat{T}^N|\Phi\rangle = 2\sum_{i}^{N/2}\langle\phi_i|\hat{T}|\phi_i\rangle \,, \tag{4.16}$$

and the minimisation occurs over the fictitious N-electron wave-function which itself consists of the sum of single electron wave functions.

This approach pioneered by Kohn and Sham shows there is an exact relationship between the density and ground state energy of a system of non-interacting electrons (represented by the N-electron wave function) and the real many-body problem. However, this relationship between energy and density only holds if the exact functional (i.e. the XC term E_{ec}) is known. Hence, the success of DFT often relies on the model used for exchange and correlation.

4.2.1 Exchange and Correlation Functionals

Searching for approximations for XC functionals is still a rapidly expanding area of research [87]. However, returning to the trial system of a homogeneous electron gas by Thomas and Fermi in the 1920s we can use the Thomas-Fermi formalism solely for the exchange part of the energy functional. This reduces the dependence of the calculation on the less accurate Thomas-Fermi theory. Hence, we can write the XC term as,

$$E_{xc}[\rho] \approx \int \rho(\mathbf{r})\epsilon_{xc}(\rho(\mathbf{r}))d\mathbf{r}\,, \tag{4.17}$$

where ϵ_{xc} in the *local density approximation* is a function of only the local electron density. Separating this term into two $\epsilon_{xc}(\rho) = \epsilon_x(\rho)+\epsilon_c(\rho)$ the Dirac form of exchange can be used here (i.e. $\epsilon_x(\rho) = C\rho^{1/3}$ where C has been used to introduce greater applicability). For the correlation term ϵ_c results from Monte-Carlo simulations which themselves yield numerically exact results are used [34]. These terms are collectively known as the local density approximation (LDA). The LDA functional has shown significant success in modelling certain systems. However, the LDA approximation is known to contain errors and a large part of the success of this method is due to a fortuitous cancellation of errors [87].

Additional functionals for XC that go beyond LDA have now been developed. The first can be considered to be a first order correction of the the zeroth order LDA approximation. This method known as generalised gradient approximation (GGA) expands the functional that depends on both the density and gradient of the density.

$$E_{xc}[\rho] \approx \int \rho(\mathbf{r})\epsilon_{xc}(\rho, \nabla\rho)d\mathbf{r}\,. \tag{4.18}$$

The GGA improves on the LDA method greatly in certain situations such as the binding energy of molecules, which has lead to it being widely adopted in quantum chemistry. However, for solids it is often still the case that the LDA method reproduces known physical constants such as the lattice parameter or bulk modulus far better. Numerous functionals now exist for describing particular physical systems such as hybrid models that straddle the LDA and GGA functionals and Meta-GGA functionals that depend on the Laplacian of the density, however these are outside the scope of this work. A review of the various functionals and their success in both quantum chemistry and condensed matter systems can be found in the work by Kurth, Perdew and Blaha [113].

4.3 Orbital-Free Density Functional Theory

Since an accurate calculation of the DSF[3] requires ensemble averages over a large number of particles and long time scales, full Kohn-Sham DFT (KS-DFT) is computationally expensive in the WDM regime and becomes impossible at temperatures above a few tens of eV. The computational expense is due to the finite temperature treatment of electronic orbitals; these are filled according to the Fermi-Dirac distribution, which becomes smoother and broader as the temperature increases. Therefore, to capture the behaviour of all thermally excited electrons requires a considerable number of partially filled states to be orthogonalised, a task that grows as the cube of the system size, N. In order to take advantage of the largest possible number of particles in the simulation volume and maximize the computational speed, here we have instead adopted an orbital-free DFT (OF-DFT) approach. In this technique the electron energy functional is described entirely in terms of the electron density, without the need to solve for the wave-functions in the system. Akin to reverting to the earlier Thomas-Fermi approach. The XC terms are still present in DFT calculations, and as such the results remain more sophisticated than traditional Thomas-Fermi calculations. The inclusion of LDA and GGA functionals are analogous to including the Dirac and Dirac-Weizsacker corrections respectively.

4.3.1 Non-Local and Local Pseudopotentials

Typically, in KS-DFT the wave-functions within a program are stored as plane-waves. Plane-waves are particularly successful at describing the density between atoms but the rapidly varying spherical wave-functions surrounding the atoms require increasingly larger number of plane-waves to accurately capture the physics. The pseudopotential concept was introduced in 1970 by V. Heine [89] to remove the core states from the Hamiltonian and construct a pseudo-Hamiltonian containing only the outer shell of electrons. These softer potentials reduce the number of electrons in the calculation and produce smoother wave functions vastly reducing computational costs. Also, since most atomic processes involve only the outer shell of electrons the physics of most systems can still be easily captured by this process. Pseudopotentials for most elements are now commonly available and give the potentials for these atoms in terms of atomic orbitals (s,p,d,f . .), hence they are given the name 'non-local'.

[3]Calculations of the SSF through full Kohn-Sham DFT is currently possible on a desktop computer as the constraints on simulation length and time-scale required to obtain accurate results is considerably reduced for static properties.

Moving from full Kohn-Sham DFT to an orbital free representation is relatively easy to implement within a modern day DFT code, and this functionality exists in the ABINIT software which was used for this work [74]. However, as is typical with all molecular dynamics problems the main difficulty is associated with obtaining a physically accurate potential. As the name suggests the orbital free method is particularly inadequate at describing atomic orbitals and so it is wise to 'freeze' the inner electrons out of the calculation, as in standard DFT. However, the wide variety of 'tested' pseudopotentials that exist for full DFT are non-local. In order to perform orbital free DFT a so called local pseudopotential is needed as no orbitals exist onto which the angular momentum states can be projected. This local potential is still a pseudopotential (i.e. the inner most electrons are not treated explicitly in the calculation) but is a function only of position relative to the atom.

The first attempts to develop these potentials involved fitting to analytic forms of the potential to obtain physical parameters, similar to the method used to calculate classical potentials in MD. More accurate methods involved calculating an electron density using full Kohn-Sham DFT and inverting the Hohnberg-Kohn equations (including kinetic energy terms) to obtain a local potential. However, the accuracy of these methods has been disputed as they rely on the accuracy of the kinetic energy operator, which, as mentioned earlier, is still one of the biggest discrepancies in the Hohnberg-Kohn formulism[96].

The most successful methods involve inverting the Kohn-Sham equations as opposed to the Hohnberg-Kohn equations. This allows the calculation to be performed with the exact non-interacting kinetic energy instead. This effective Kohn-Sham potential must then have the XC and coulomb interaction terms removed to obtain the actual local ion potential. This can be done for a single atom, or as has been shown to be more transferable, for an atom embedded within a crystal structure. This type of potential is known as a bulk local pseudopotential (BLPS). This work utilizes a BLPS developed in this way.

4.3.2 Inverting The Kohn-Sham Equations

Following the implementation by Zhou *et al.* [217] we have implemented an iterative method to create this local pseudopotential. Beginning by defining a new functional W as follows [214],

$$W[v_{eff}] = T_s[v_{eff}(\mathbf{r})] + \int (\rho(\mathbf{r}) - \rho_{in}(\mathbf{r}))v_{eff}(\mathbf{r})d\mathbf{r}\,. \tag{4.19}$$

where ρ_0 is a target electron density calculated with Kohn-Sham DFT, v_{eff} a trial local potential and T_s and ρ the resulting kinetic energy and electron density obtained after solving the Kohn-Sham equations for an identical system. Wu *et al.* have shown that at the constrained minimum of T_s this functional also must be stationary with respect to variation in the potential $v_{eff}(\mathbf{r})$. That is,

$$\frac{\delta W[v_{eff}]}{\delta v_{eff}(\mathbf{r})} = 0\,, \tag{4.20}$$

and hence,

$$\rho(\mathbf{r}) - \rho_{in}(\mathbf{r}) = 0\,. \tag{4.21}$$

In addition to this they showed that this stationary point is a maximum. Thus the value of v_{eff} that maximises this functional will be the potential which reproduces the target electron density v_{in}. This functional contains only the Kohn-Sham kinetic energy terms and the external potential and so the potential that is returned will be the Kohn-Sham potential, v_{eff}. The Hartree and XC terms must be subtracted as in Eq. (4.12) to obtain the real local potential that can be input into subsequent orbital-free calculations.

4.3.2.1 Representation of Local Potentials

In this work the local pseudopotential is represented in Fourier space with the coulombic part of the potential subtracted to avoid the potential diverging at the origin, this non-coulombic part of the potential is then represented on an orthogonal basis set based on the zeroth order Fourier-Bessel series. It is defined such that,

$$V_{nc}(q) = \sum_{i=1}^{L} A_i J_0(q\alpha_i)\,, \tag{4.22}$$

where L is the number of functions in the series, A_i Bessel function coefficients, J_0 the zeroth order Bessel function of the first kind and α_i the positive roots of the zeroth order Bessel function. If the potential is known then the coefficients can be reverse calculated from,

$$A_i = \frac{2}{[J_1(\alpha_i)]^2} \int_0^1 q V_{nc}(q) J_0(q\alpha_i) dq\,. \tag{4.23}$$

This series based on the zeroth order Bessel functions of the first kind was chosen as the shape is similar to the non-coulombic part of the local potential and hence with only a few coefficients the entire potential can be accurately represented, see Fig. 4.1.

It is important to note that this Bessel series is only defined over the range $0 \rightarrow 1$ and so in practice the variable q must be supplemented by a dummy variable $q' = q/q_{max}$, in which q_{max} is chosen *a-priori* and the potential is smoothed to zero beyond this point. Carter *et al.* note that a cut-off function with the form $f(q) = exp(-[q/q_{max}]^6)$ greatly increases the computational efficiency of the work without effecting the quality of the potential.

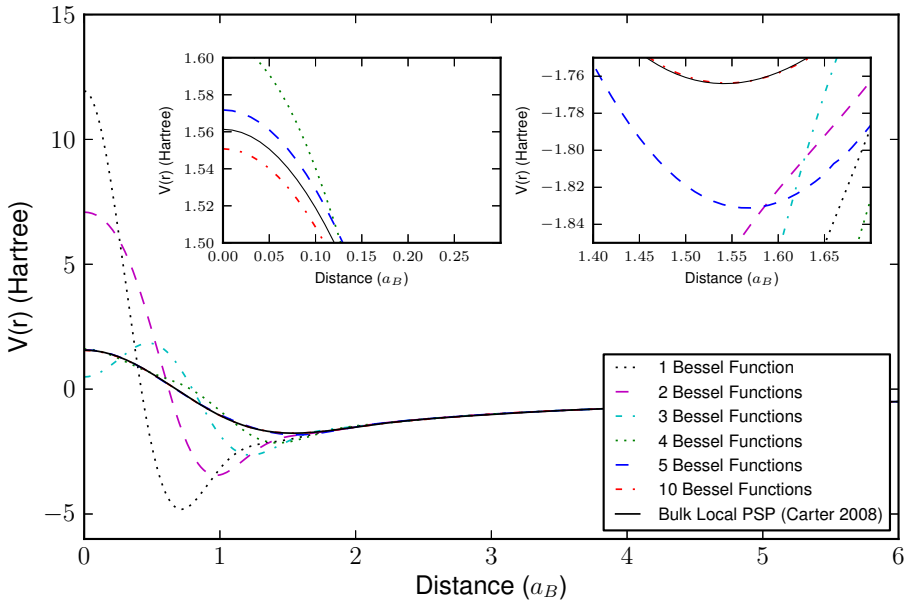

Figure 4.1: Representation of the local pseudopotential of Al using varying number of Bessel functions. A potential from Carter *et al.* [96] is shown for comparison.

With this framework in place a *wrapper* program was written in python to minimise the negative of the Wu functional given in Eq (4.19) with respect to the Bessel function coefficients. This steps of this program are outlined below,

1. Run a complete Kohn-Sham DFT calculation on a trial system to obtain the 'correct' electron density.

2. Create a trial local pseudopotential either from random coefficients A_i or an initial guess.

3. Run a DFT calculation without *self consistent field calculations* and calculate the Wu functional.

4. Update the pseudopotential coefficients using a minimisation routine to minimise the negative Wu functional.

5. Repeat steps 3 and 4 until convergence in the minimisation routine.

The benefit of this wrapper formalism over integrated methods that other groups have implemented is two-fold. Firstly, it can be used with different DFT codes with minimal effort, or with updated versions of the same code. Secondly, the minimisation routine used can be easily varied. Initially two routines were chosen - the *downhill simplex* method and the *conjugate gradient* method. These two standard minimisation routines can be found in the *numpy* numerical library and are covered in great detail in Ref. [158]. Both these routines are essentially serial in that that try a single potential at any one time and then update the results, and although the ABINIT software package is parallelised the time to convergence is often slow taking many days on a typical desktop. Furthermore, this method is particularly sensitive to initial conditions and cannot always find the global minimum, instead producing potentials with non-physical oscillations.

The latest iteration of the software utilises a genetic algorithm (GA) approach implemented within the open source 'pyevolve' framework. A genetic algorithm is a stochastic machine learning code that takes a different approach to function minimisation. Crucially, it is trivially parallelised and exceptionally good at locating global minima. Appendix C contains details of the minimisation code.

Using this method we have created potentials for a variety of atomic elements including aluminium, silicon, magnesium and carbon. Work is on going with these potentials, however we have performed an in-depth study on aluminium as this is the typical test case for HEDP problems. Furthermore, we have compared the results calculated through OF-DFT with KS-DFT and with classical MD. Crucially, the results presented here are compared with experimental X-ray scattering data in chapter 5.

4.4 Simulation Details

The KS-DFT simulations were performed using the projected augmented wave (PAW) framework [24]. To evolve the ion trajectories, we performed molecular dynamics simulations using a 108 ion cubic supercell in the isokinetic ensemble, with periodic boundary conditions applied. The kinetic energy was maintained constant through the use of a Gaussian thermostat. The cell was evolved to a simulation length up to 1 ps and in time-steps of 2 fs. In each time-step the DFT equations for the electrons are solved in the Born-Oppenheimer approximation; ion positions are then updated classically according to the electrostatic forces computed from the known ion positions and the 'frozen' electron charge density. The system is modelled in

full thermodynamic equilibrium, with equal electron and ion temperatures. Brillouin zone sampling was performed at the mean value point [17]. XC was treated within the GGA framework of Perdew, Burke and Ernzerhof [151]; electron interactions were described using a three valence electron PAW pseudopotential. The plane wave and augmentation cut-off energies were 952 eV and 2720 eV, respectively, ensuring convergence in the electronic DOS.

In OF-DFT the absence of electron wave-functions requires that the kinetic energy must be a functional of electron density only. Our simulations were carried out using the Thomas-Fermi module of ABINIT with the XC terms treated within the LDA. The LDA and GGA approximations have shown remarkable agreement in describing the properties of bulk aluminium [185] and are not expected to make significant differences to the dynamic or thermodynamic properties of the system. Replacing the kinetic energy functional introduces an error at lower temperatures where the system is dominated by bound electrons; we expect the error introduced to diminish with increasing temperature [75]. The OF-DFT simulations contained 500 atoms and utilized a bulk-derived local pseudopotential. This pseudopotential was checked for accuracy by reproducing the electron density within a bulk material as discussed earlier.

Trajectories were evolved over a simulation length of 5 ps, using a time-step of 0.25 fs. The time-step was chosen to ensure energy conservation within the ion subsystem while the simulation length was chosen to give high resolution DSF data. The DSF was then calculated using the final 1.5 ps of the simulation. Performing these calculations to the necessary accuracy requires considerable computational effort. Both the KS-DFT and OF-DFT simulations were performed using the massively-parallel AWE supercomputer, Blackthorn.

4.5 Calculation of Pressure

Fig. 4.2 compares the pressures calculated with both KS-DFT and OF-DFT over a range of temperatures, and demonstrates that OF-DFT reproduces well the KS-DFT thermodynamic pressure above ≈ 2 eV. Also shown are OF-DFT results that have not been corrected for XC. The relatively poor agreement of this data compared with the KS-DFT calculations indicates the importance of including the XC term as shown previously by Danel *et al.* [41]. Fig. 4.3 also shows agreement between OF-DFT and KS-DFT in the SSF. Validation of the orbital-free approach through comparison with the static and thermodynamic properties has shown similar agreement in dense

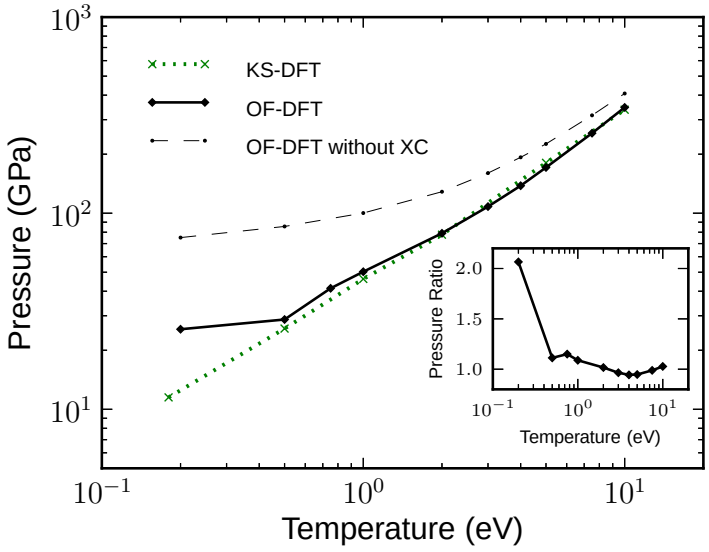

Figure 4.2: Pressure of warm dense aluminium at solid density extracted from KS-DFT (dotted) and OF-DFT (solid). The two methods converge for $T \gtrsim 2$ eV. The convergence is highlighted by the inset, which shows the ratio between the OF-DFT and KS-DFT pressures. The dashed line represents OF-DFT calculations performed without treating XC, indicating the importance of these terms in this temperature regime.

hydrogen plasmas [161] and liquid aluminium [12], but here is shown explicitly for the WDM region of phase space.

4.6 Calculation of the Static Structure Factor

In addition to the DFT simulations, we have also considered a hybrid approach where the structure factor is extracted from a classical MD simulation with an effective ion-ion potential given by [197],

$$V_{ii}^{\text{eff}}(r) = \left[\frac{Z^2\mathrm{e}^2}{r} + \frac{(Z_c^2 - Z^2)\mathrm{e}^2}{r}e^{-br}\right] e^{-\kappa r}, \tag{4.24}$$

where $Z_c = 13$ is the atomic number for aluminium, $Z = 3$ is the charge state, and κ is the Thomas-Fermi screening length. The parameter b represents the effect of increased nuclear repulsion when there is interpenetration of the bound electron charge clouds around each nucleus. It determines the onset of the short range repulsion (SRR). Setting $b \to \infty$ gives the usual Yukawa potential. The classical MD simulations were again run with 864 atoms in 0.2 fs time steps for a simulation time of 1.5 ps. We used

the LAMMPS package [156] with a micro-canonical ensemble and a velocity rescaling thermostat.

As discussed in the work by Vorberger *et al.* [171, 197], the parameter b can be determined by the requirement that the SSF obtained via classical MD simulations reproduce the KS-DFT SSF. This is shown in Fig. 4.3. Classical MD simulations with the simpler Yukawa potential underestimate the correlation in the system when compared with the other methods. In Ref. [197] it was argued that it is indeed necessary to include the SRR term in the ion-ion potential in order for classical MD to match DFT simulations. In our situation, this is achieved by taking the parameter b to be $0.7\,a_B^{-1}$ and $1.12\,a_B^{-1}$ for $T = 0.5$ and $T = 5$ eV, respectively. On the other hand, OF-DFT SSF compare very well with KS-DFT results, without the need to introduce any adjustable parameters.

Vorberger *et al.* also suggested that the agreement between classical MD with a Yukawa+SRR potential and KS-DFT in the SSF implies that MD simulations can then be used to calculate the DSF. However, while this approach does represent a significant step forward, compared with various semi-analytical methods, it may not capture the response for the case of a time-dependent ion-ion interaction screened by a dynamical electron background. This is relevant to situations where the electron oscillations couple with ion acoustic modes, as described through the plasmon-pole approximation [13, 19].

Our OF-DFT approach is instead able to include such effects in a consistent way, as the electron response is continuously updated in time throughout the simulation. Recent work by Rüter and Redmer showed that KS-DFT is able to reproduce experimentally measured SSFs in aluminium samples at densities of 8.1 g/cm^3 and at temperatures of 10 eV [169], well within the WDM regime.

4.7 Calculation of the Dynamic Structure Factor

We have calculated the DSF $S(k, \omega)$ at three different values of k, to span the hydrodynamic ($k = 0.24\,a_B^{-1}$), generalized hydrodynamics ($k = 0.51\,a_B^{-1}$) and single particle ($k = 2.0\,a_B^{-1}$) regimes [136]. The results of our calculations performed using OF-DFT and classical MD simulations with both Yukawa and Yukawa+SRR are presented in Fig. 4.4. In the large k regime, all models converge to the ideal gas result. However, at smaller values of k, the differences between the calculations are substantial. While classical MD simulations with a Yukawa+SRR potential agree better with OF-DFT, there is still an important difference in the position of the ion acoustic resonance. It is

informative to plot the position of the peak of the resonance against the wave-number, to yield the dispersion relation for these different models, as shown in Fig. 4.5. Differences in the dispersion relation result in different estimates to the sound speed, given by $d\omega/dk|_{k\to 0}$. The dispersion relation is assumed to be linear below $k = 0.2a_B^{-1}$.

It is clear that for small k the MD Yukawa+SRR matches well the OF-DFT results. This regime corresponds to modes that have spatial correlations larger than the scale associated to SRR, here we expect the fluctuation modes to be insensitive to the degree of SRR. However, as k increases and the correlation scale is reduced below that of the repulsion, and the dispersion curves diverge suggesting that the SRR correction is no longer adequate to describe the particle dynamics. At higher k still the methods converge towards the single-particle regime, which is less sensitive to the specific form of the potential.

4.8 Conclusions and KS-DFT calculations of the DSF

Although there is reasonable agreement between classical MD simulation with a Yukawa+SRR potential and the OF-DFT for warm dense aluminium, the applicability of the classical method is limited by the fact that the ion-ion potential must be known *a priori*. The proposed Yukawa form is not always reasonable, such as for metallized hydrogen [204] or molecular plasmas. Our OF-DFT quantum simulations of the ion-ion structure factor provides a unique platform where dense plasma theory can be tested with high accuracy.

As computational power increases, particularly with massively parallel computing, the ability to calculate structure factors using the more expensive Kohn-Sham method has become a possibility. One of the most important steps towards validating this method is comparison between OF-DFT and KS-DFT. Recently performed KS-DFT simulations performed by S. Hamel at the Livermore National Laboratory were run for 10ps (2 fs steps), 1000 atoms, for solid density aluminium at a temperature of 0.5 eV [85], i.e. the conditions of the colder systems studied in this work. The results of these have been added to Fig. 4.4 and labelled as KSDFT-MD. There are some differences between the OF-DFT and KS-DFT as can been seen in the top three panels of the figure. Whether this is to do with finite size effects (our simulations used 500 atoms) or a fundamental difference between the OF-DFT and KS-DFT methodologies is to be investigated further. It should be noted, however, that at these low temperatures it is not unlikely the differences are inherent to the method

(i.e. KS-DFT will form bound states). We expect the orbital free theory to struggle as orbitals become increasingly important. Encouragingly, the OF-DFT results are closer to the KS-DFT results than the SRR method.

Recently the DSF of aluminium at a higher temperature (3.5 eV) and density (5.2 g/cm^3) have been completed by Rüter and Redmer (2014) [169]. A similar increase in the sound velocity with temperature was seen, in agreement with this work. The paper by Rüter and Redmer represents the latest in KS-DFT calculations that can be performed and contained 256 atoms and were run for 3.08 ps. In contrast the simulations performed in this work contained 500 atoms and were run for 5 ps. As computational power increases and becomes more accessible the regimes that can only currently be covered by classical MD will begin to be accessed using the OF-DFT method and likewise the regime accessible to the OF-DFT method with be available to the KS-DFT methods. However, currently the calculation of ion waves in warm dense matter that have the possibility to be accessed through X-ray scattering techniques, discussed in the following chapter, can only be completed using OF-DFT methods without requiring an expensive super-computer. A further advantage that should be mentioned is the possibility with OF-DFT to run multiple simulations across a range of temperatures and densities and use the predictive power of an *ab-initio* tool to measure experimentally the temperature and density through fitting the results. This technique would be computationally prohibitive in the Kohn-Sham method, even with the large super-computers available to national laboratories.

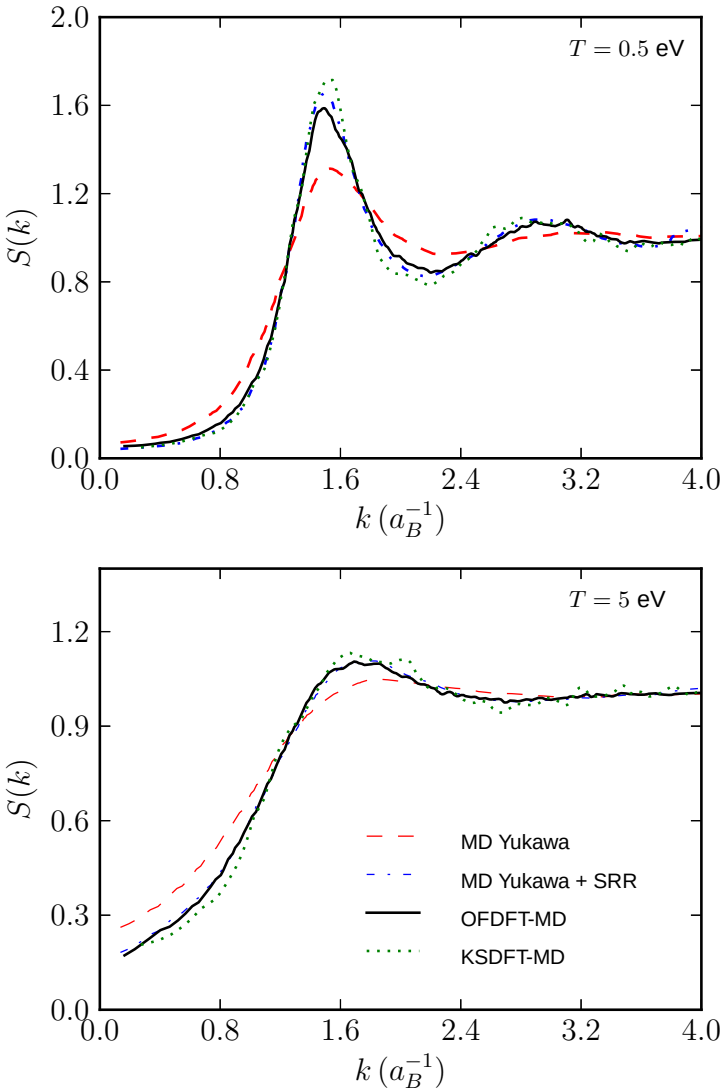

Figure 4.3: The SSF for warm dense aluminium calculated from MD with Yukawa potential (dashed), Yukawa+SRR (dotted-dashed), OF-DFT (solid), and full KS-DFT (dotted). Shown here for $T = 0.5$ eV (top panel) and $T = 5$ eV (bottom panel)

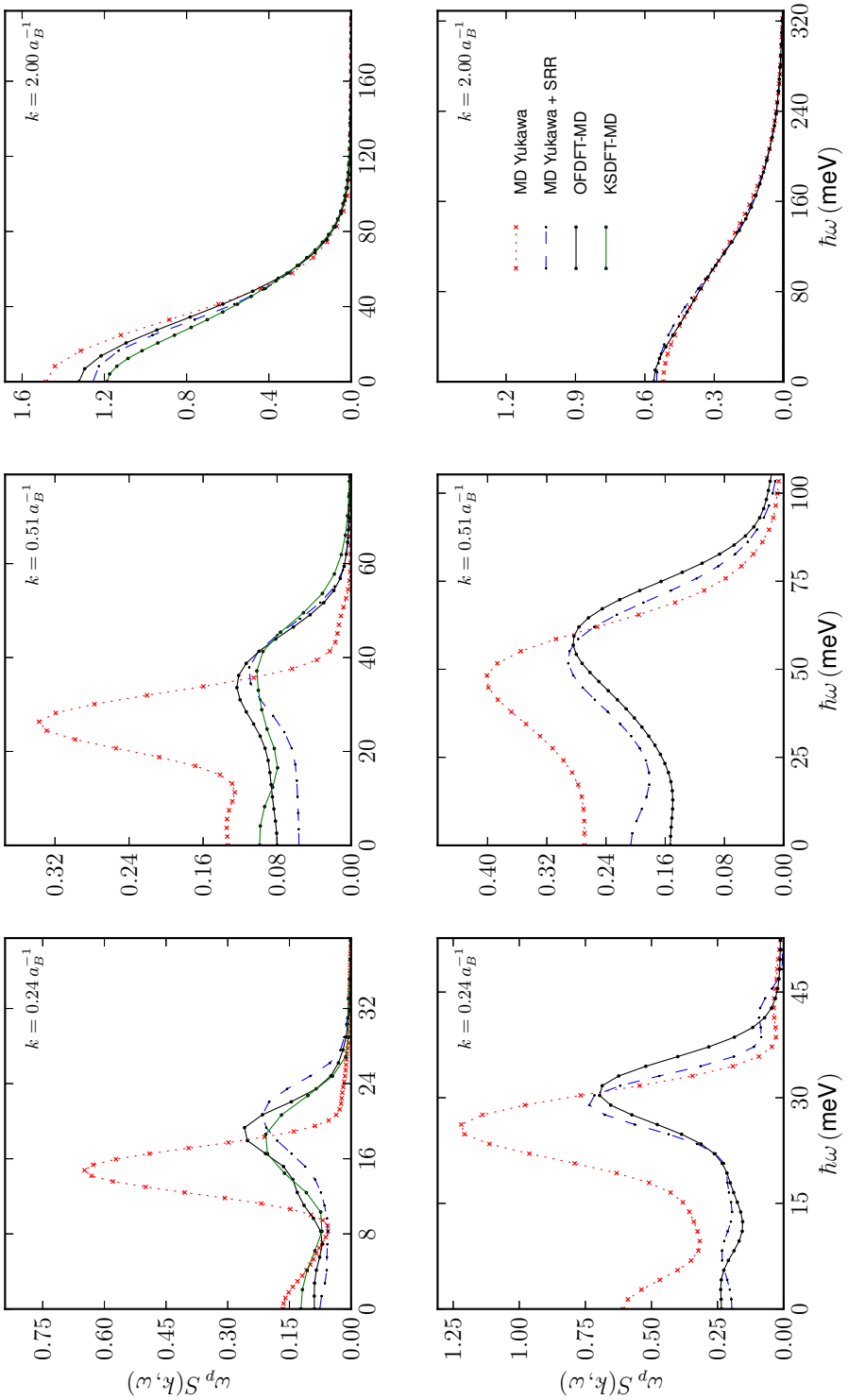

Figure 4.4: The DSF for warm dense aluminium calculated from MD with Yukawa potential (dotted), Yukawa+SRR (dashed), and OF-DFT (solid). Shown here for $T = 0.5$ eV (top panels) and $T = 5$ eV (bottom panels). The 0.5 eV case has results from a full Kohn-Sham calculation overlay in green [85].

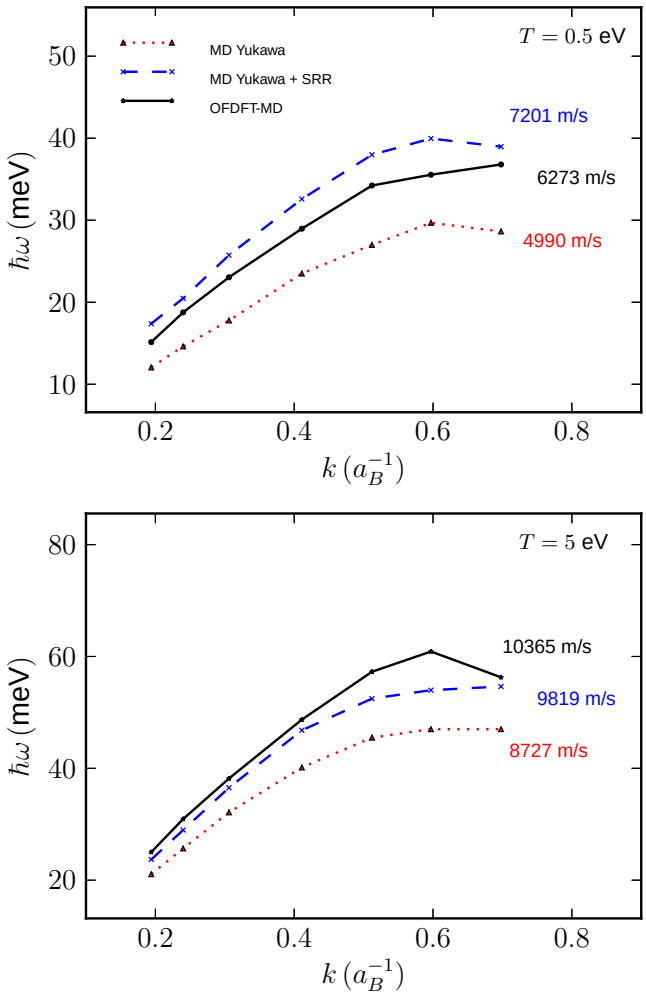

Figure 4.5: The dispersion relation for warm dense aluminium calculated using OF-DFT (solid), MD with Yukawa potential (dotted), and MD with Yukawa+SRR (dashed). Results shown here are for $T = 0.5$ eV (top panel) and $T = 5$ eV (bottom panel). Also shown are the resulting sound speeds for each condition.

Chapter 5

Experimental Measurement of Acoustic Ion Waves in a Dense Plasma

5.1 Ion Acoustic Waves

As detailed in section 2.2.3 the complete DSF contains terms from both the high frequency electronic response and the low frequency ion motion. Up to now experiments have been performed which measure the electronic components of the DSF ($S_{ee}(k,\omega)$), that is the plasmonic and bound-free contributions, which typically gives rise to energy transfers of the order of tens of eV in the scattered radiation [58, 72]. These scattering experiments performed in the WDM regime have allowed the electronic properties, including collision damping and relaxation processes, to be compared with theoretical models. Measurements of the low frequency ion component of the DSF $S_{ii}(k,\omega)$ have so far remained elusive due to the strict requirements on photon number and bandwidth, the peaks in $S_{ii}(k,\omega)$ are separated by just a few hundred meV. Numerous theoretical approaches have been proposed to describe these ion acoustic waves, including the formalism developed in chapter 4, however experimental validation is now crucial.

Measurement of the ion component of the DSF will finally allow the entire spectrum to be measured experimentally and provide an enormous wealth of information on the so far poorly understood transport properties including energy equilibration. With the advent of 4th generation light sources, based on FEL technology, experiments that require extremely high photon flux in a narrow bandwidth have become possible. The upgrade of the LCLS FEL at Stanford, California to operate in a

self-seeded mode with an unprecedented narrow bandwidth have allowed a proof-of-principle experiment to measure the ion waves in a dense optically opaque plasma to be performed.

5.2 Linac Coherent Light Source

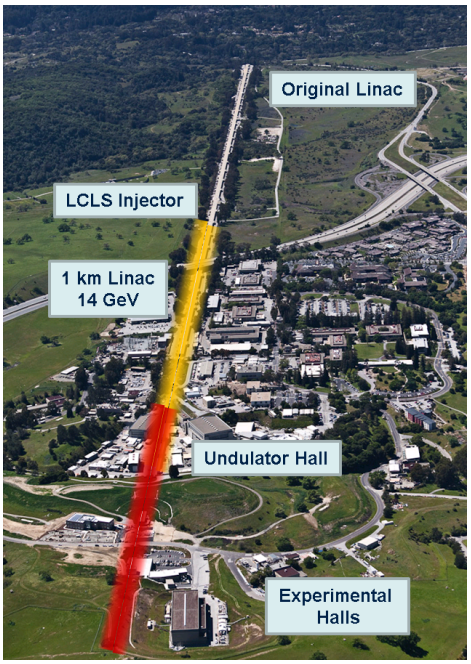

Figure 5.1: An aerial view of the Linear Coherent Light Source with major sections of the accelerator highlighted. The experiment was performed at the matter in extreme conditions (MEC) end-station located within the experimental halls at the bottom of the photo.

The LCLS is a FEL at the SLAC National Accelerator Laboratory located in Menlo Park, California. It was built from 2006-2009 and utilises the last 1/3 of the original linear accelerator. LCLS uses the high energy electron bunch from the accelerator and passes these electrons through an undulator, a periodic alternating arrangement of magnetic fields. As electrons wiggle in the undulator they emit incoherent but monochromatic synchrotron radiation. However, the emitted radiation interacts with the electrons as they travel along the length of the undulator causing the electrons to move into micro-bunches. These micro-bunches are separated by a distance equal to one wavelength of light and leads to coherent radiation being emitted. This mode of operation is known as self-amplified stimulated emission (SASE).

The constructive and destructive interference of the emitted light leads to high coherence, high intensities and low divergent beams of X-rays, hence the name X-ray laser. FEL technology represents the highest brilliance on the planet with $\sim 10^{25}$ ph/s/mrad^2/mm^2/0.1% BW average and $\sim 10^{34}$ ph/s/mrad^2/mm^2/0.1% BW peak brilliance [211].

One of the crucial advancements in the performance of LCLS, that has in fact allowed the following experiment to be performed, is the introduction of a self-seeding mode. One of the problems with SASE is that the initial seeding takes a finite time to occur and hence temporal coherence can be lost. Hence, a noisy spectrum is quite typical of a SASE beam from a FEL. This can be overcome by instead seeding the FEL with a laser tuned to the resonance of the undulator. However, true X-ray lasers are not currently at the stage where they can be used for such a purpose meaning that a seeded X-ray FELs was not possible. This changed in 2012 when LCLS began operating a self-seeded mode, utilising two undulators in sequence. The radiation from the first undulator was used to seed the X-ray beam in a second undulator. A diamond monochromator placed between the two undulators filters the spectrum of the seeding radiation. Since the radiation travels *marginally* faster than the accelerated electrons the radiation is delayed before entering the second undulator in a Bragg chicane. The beam spectral quality was improved considerably and at 8 keV the bandwidth was reduced from around 20 eV to just 1 eV [10].

5.3 Experimental Set-up

The experimental set-up is relatively simple. A 50 μm thick aluminium target is coated with 2 μm of plastic to act as a tamper [189]. Two optical lasers each with approximately 5 J of energy in 3 ns are focused to a spot of 50 μm on the target to create a two converging shocks. A continuous phase plate is used to impose a spatially flat-top profile onto the optical lasers. The experimentally measured pulse shapes both temporally and spatially are given in Figs. 5.3 and 5.4 respectively.

A 1-D hydrodynamic calculation of the laser interaction with the aluminium sample was performed to help define the time required between the optical lasers incident on the target and the X-ray beam. This was achieved using the commercial 1-D hydrodynamic code Helios [124]. Although 1-D hydrodynamic codes are known to overestimate the shock velocity, the shock coalesce time should be found to within a few nanoseconds. Fig. 5.5 shows a mass-density 2-D plot output from the hydrodynamic code Helios. The predicted convergence time of the two shock-waves in a

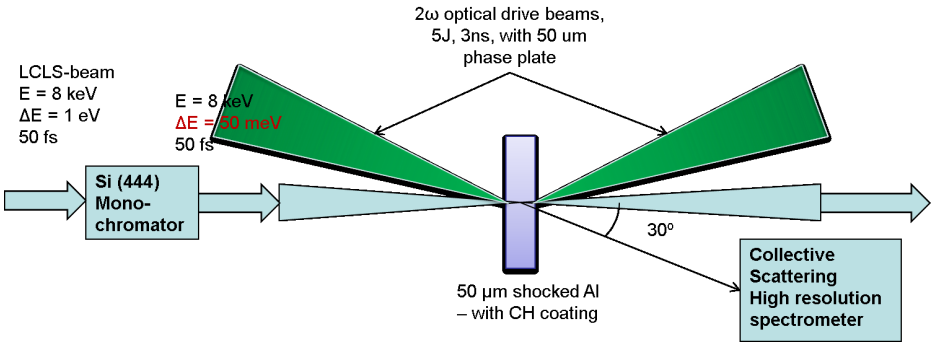

Figure 5.2: Schematic of the experimental set-up. Two long-pulse optical lasers working at 532 nm with 5 J of energy in 3 ns are focused through a phase plate to produce a spot size of 50 μm diameter on a 50 μm thick aluminium target coated with a 5 μm CH tamper. The seeded LCLS beam is delayed with respect to the optical beam and passed through a Si (444) crystal monochromator to reduce the bandwidth of the incoming X-rays further. The scattered X-rays are collected and spectrally resolved by a high resolution crystal spectrometer covering a large solid angle at approximately 30°. The experiment was performed at the matter in extreme conditions (MEC) end station at the LCLS.

50 μm aluminium sample, with a 5 μm CH tamper layer on each side, is approximately 1.5 ns after laser irradiation. This time-scale was used as an estimate to allow the actual shock coalescence time to be found during the experiment.

The X-ray beam was delayed with respect to the heating beam by 2 ns, and is focussed through a beryllium compound refractive lens to a spot a few microns in diameter. The spot was positioned spatially at the centre of the heated region. Since one-dimensional hydrodynamic codes are known to over-predict the shock velocity, and hence the convergence time, a time somewhat longer than that predicted was used to ensure a warm dense state was probed. In the self-seeded mode the 8 keV the X-ray beam contains approximately 10^{12} photons and has a spectral resolution of $\Delta E/E = 10^{-4}$ and a temporal resolution of approximately 50 fs [10]. However, even with these parameters the ion waves could not be resolved in the scattered spectrum as they have an energy of just a few hundred meV. Therefore a high resolution crystal monochromator is used to further reduce the bandwidth of the beam.

The high-resolution channel-cut Si (444) monochromator shown in Fig. 5.6 was used at a Bragg angle near 90°. Due to the narrow rocking curve of this crystal the bandwidth of the X-ray beam is significantly reduced to approximately 50 meV. However, the downside of this reduced bandwidth is that the number of photons incident on the target is also reduced by an order of magnitude.

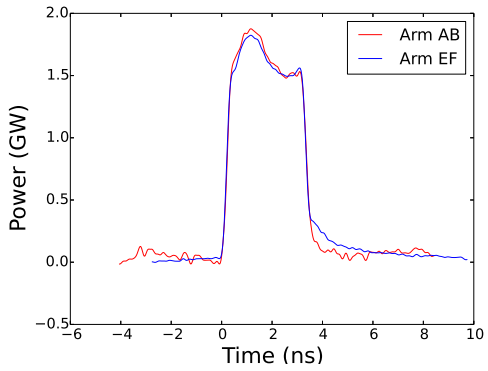

Figure 5.3: Temporal profiles for the two long-pulse lasers used to create the dense plasma state at LCLS. Arm AB and EF correspond to the beams incident on each side of the aluminium target.

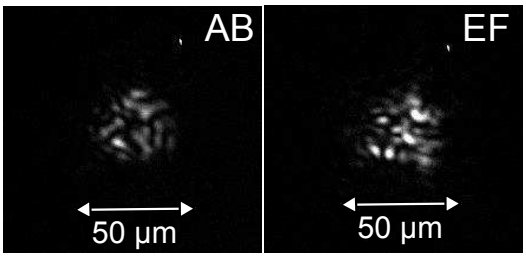

Figure 5.4: Spatial profile of the laser AB (left) and EF (right) used to drive the system to a WDM state. The speckle pattern is due to the phase plates which create a more 'flat-top' beam profile as opposed to a more standard Gaussian or super-Gaussian profile.

As mentioned in section 2.2 the scattering cross section is extremely low for Thomson scattering and so a large area detector is used to increase the signal. The larger the solid angle that a detector covers the more photons that are collected, however the downside of this is the k-vector blurring due to collecting scattered X-rays simultaneously from a large spread of angles. For this experiment a spherical diced Si (444) crystal, shown in Fig. 5.7, was used in Johann geometry, i.e. the sample and detector are both on the Rowland circle [97]. The crystal was placed 1 m away from the target giving a maximum bandwidth that could be measured experimentally of just 300 meV. Therefore, in order to obtain both the up-shifted and down-shifted spectra it was necessary to rotate the crystal analyser by 0.02° through the X-ray axis. The two spectra could then be 'stitched' together during post-processing. The diced crystal is made up of many 0.7 mm square single crystals to give a total diameter of 10 cm. These single crystals overcome the spectral loss in resolution associated with traditional bent crystals. In this set-up each of the crystallites produces an identical spectrum that overlap on the detector, thus increasing the efficiency beyond that of a single perfect crystal.

An initial measurement of the instrument function was achieved using the seeded LCLS beam with the monochromator and high resolution crystal analyser. A cold CH target was used in the sample location. Since the structure factor for a cold poly-crystal outside of the Bragg peak is many orders of magnitude less than that for

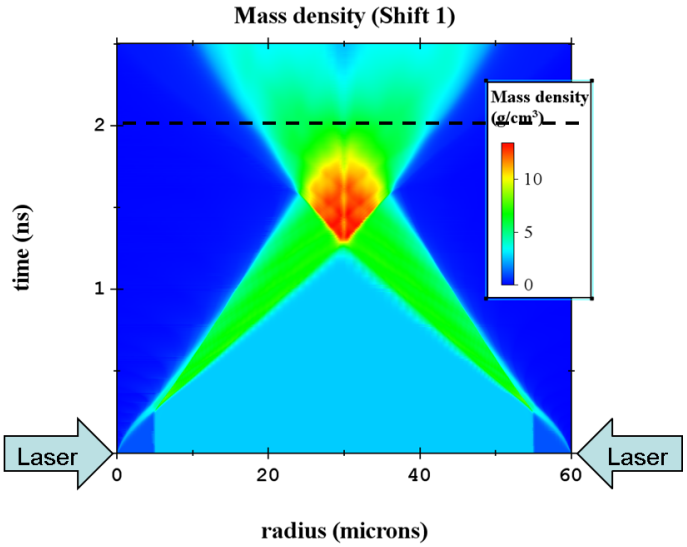

Figure 5.5: Mass density plot performed with the 1-d hydrodynamic code Helios showing the convergence of two shock-waves in a 50 μm aluminium sample with a 5 μm CH tamper on each side. The dashed line indicates the arrival of the X-ray probe beam.

a liquid or dense plasma state the signal was obtained by integrating over 5000 shots. With this set-up the total instrumentation function was measured to be approximately 100 meV, see Fig. 5.8. With this resolution we expect to be able to observe any additional peaks that appear in the scattered spectrum due to the ion-acoustic waves.

5.3.1 Photometrics

One of the most significant challenges associated with this experiment is the low number of photons collected by the detector, a product of the small Thomson scattering cross-section, sample volume and interaction time. An estimate of the number of photons expected can be calculated using the photometric equation,

$$N_d = N_{ph}\eta_{mono}|f(k)+q(k)|^2 S_{ii}(k) n_i \sigma_T L \frac{\theta_{crystal} R_{crystal} \eta_{detector}}{4\pi} \tag{5.1}$$

where $N_{ph} \approx 10^{11}$ is the number of photons in the seeded beam, $\eta_{mono} \approx 0.05$ is the efficiency of the monochromator (a combination of bandwidth and reflectivity), $|f(k)+q(k)|^2 = 146$ the atomic form factors from bound and free electrons, $S_{ii} = 0.3$ is the SSF estimated from DFT, $n_i = 1.85 \times 10^{23}$ cm^{-3} the ion density, σ_T the scattering cross-section, $L = 5\mu m$ the interaction length estimated from hydrodynamics,

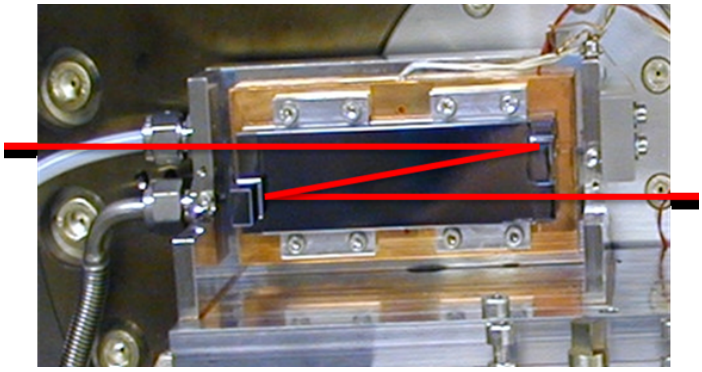

Figure 5.6: Photograph of the high resolution monochromator used to reduce the bandwidth of the LCLS seeded beam. Two high-resolution channel-cut Si (444) crystals used at a Bragg angle near 90° is used to reduce the bandwidth by over an order of magnitude.

$\theta_{crystal} = 0.08$ rad the acceptance angle of the crystal analyser, $R_{crystal} = 2^{-5}$ rad the integrated reflectivity of the crystal, and $\eta_{detector} = 70\%$ the detector quantum efficiency [147]. The result of this calculation is that we obtain ∼50 photons per shot on the detector. Each pixel on the detector covers a range of 23 meV, of the total 300 meV covered, and as such, approximately 5 photons per pixel per shot are expected. In order to obtain high quality data a large number of shots will need to be integrated over to achieve a reasonable level of signal-to-noise.

To maximise the chances of success it is important to choose a low noise detector that is capable of single photon counting. For the experiment covered here we utilised a Cornell-SLAC pixel array detector (CSpad). Each pad contains 2.3 M pixels in a 20.3×44.0 mm area, can read out at a rate of 120 Hz, and each pixel is 110 μm wide. In high gain mode the system has a S/N ratio of 6, vital for low flux experiments such as this [88]. In this mode the CSpad is able to detect single photons and can be used to obtain absolute photon numbers.

5.4 Experimental Results

Fig. 5.9 shows the collected scattered spectrum. The spectrum has been averaged across the spatial direction and is plotted against energy where 0 meV represents the energy of the incident beam. Although the CSpad detectors allow for an absolutely calibrated signal to be extracted, i.e. a precise photon number, this work is currently on-going. As such, the intensity on the left hand scale is arbitrary. The spectrum taken at these thermodynamic conditions are a summation of sixteen spectra (eight

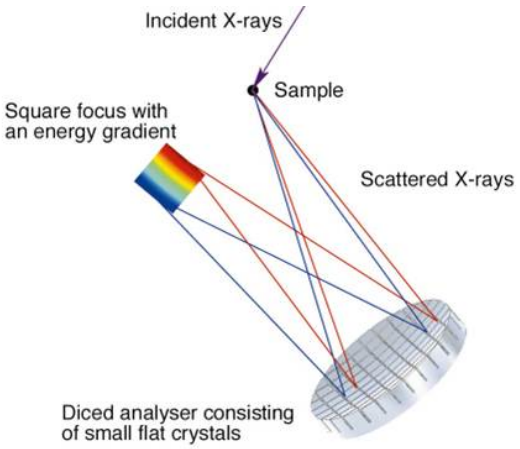

Figure 5.7: A schematic diagram of the spherical diced Si (444) analyser crystal used to obtain high resolution spectrally resolved scattering data. The crystal is made from 12000 of perfect crystals each 0.7 mm square and 3 mm deep, each operating in Johann geometry when the analyser is located 1 m from the target. The spectra from each individual crystal lie on top of one another on the detector increasing efficiency. Traditional bent crystals introduce strain in the analyser and reduce the resolution that can be achieved below that required in this work.

up-shifted and eight down-shifted) taken over an eight hour shift. The spectra were then stitched together to give the result shown.

Two peaks either side of the instrumentation function can be seen at $\pm$ 150 meV, these peaks correspond to the ion-acoustic waves. This data represents the first experimental measurement of ion acoustic waves in the WDM regime.

5.5 Comparison With Orbital-Free DFT

The next step is to compare the scattered spectrum with that predicted using the OF-DFT technique as developed in chapter 4. For the conditions measured here the temperature and density was not measured separately on the shot. Hence, the temperature and density from the hydrodynamic model must be utilised as inputs into the OF-DFT code. In this case they are taken to be 5 eV and 7 g/cm^3 respectively. However, there are questions regarding the accuracy of this method, particularly with the use of a one dimensional code. To further support this claim results taken from a similar experiment carried out at the matter in extreme conditions end station of LCLS two months prior will be compared. In this experiment identical laser parameters were used to drive a shock in identical targets, however, scattering was performed

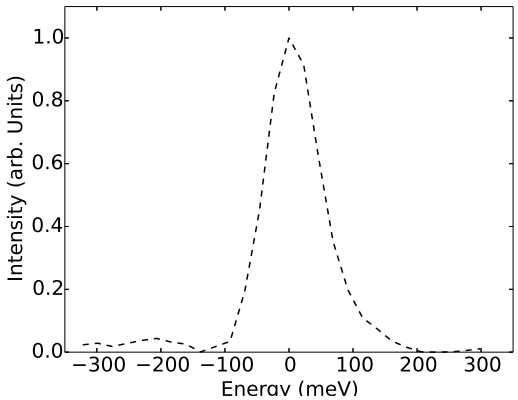

Figure 5.8: Instrumentation function measured using the seeded LCLS beam with monochromator and high resolution crystal analyser. The spectrum was obtained by scattering from a cold CH target and integrating over 5000 shots.

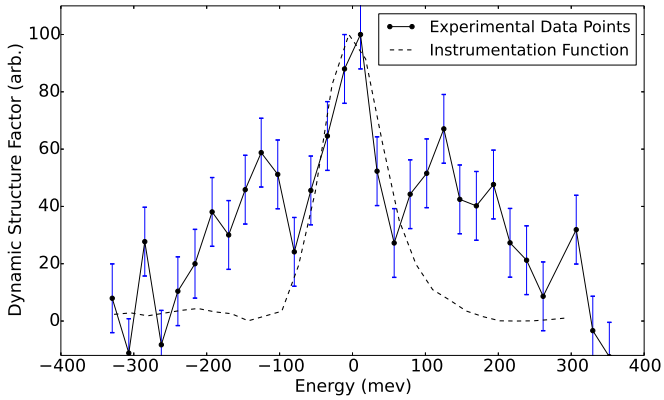

Figure 5.9: Energy resolved scattered X-rays for warm dense aluminium measured using the diced crystal analyser corresponding to the laser pulse shape shown in Fig 5.3 and 5.4. The dotted line shows the instrument function of the set-up giving a resolution of $\approx$ 100 meV

without the self-seeding and monochromator used in this work. The much higher X-ray flux (at a cost of bandwidth) allowed a direct image of the SSF to be obtained. Values for a temperature of 3 eV and a density of 6.3 g/cm^3 were obtained [2]. These results, although different, are close to those used in this work. In particular the density, which primarily defines the position of the ion-acoustic peaks, is similar. Therefore for the remaining work the values of 5 eV and 7 g/cm^3 will be used.

By running the OF-DFT code described in chapter 4 the DSF shown in Fig. 5.10 is obtained. Since we currently do not have access to absolute scattering intensities

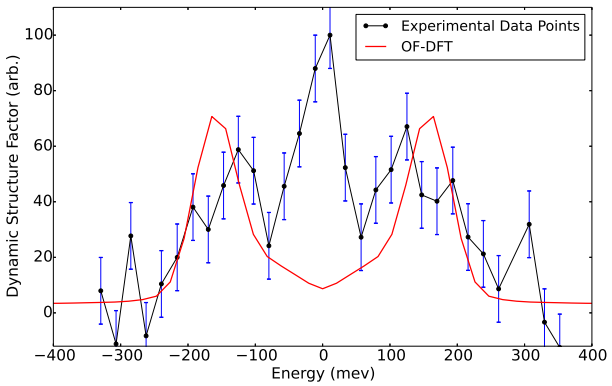

Figure 5.10: A comparison between the inelastic scattering data obtain the LCLS scattering experiment and the DSF for aluminium at a temperature of 5 eV and a density of 7 g/cm^3 taken at the corresponding k point. The simulated DSF has been scaled to match the experimental data.

the simulated spectrum has been scaled to fit the experimental spectrum. Although the error on these points is large, primarily due to low photon flux, it is clear through comparison of the experimental data with the simulation that the position of the two peaks is captured well by the orbital-free method. Certainly within the error associated with the temperature and density conditions used. Capturing the position of the peaks accurately suggests that the sound speed obtained from OF-DFT is relatively accurate, however additional experiments at multiple scattering angles, and therefore k points would allow the full dispersion curve to be mapped out.

There is, however, a large discrepancy between the experimental data and simulation, that is the presence of the central quasi-elastic peak. It should be noted here that the central peak is *not* simply the scattered X-rays from cold un-shocked material[1]. Indeed, a quasi-elastic peak or entropy peak as shown here is often present in scattering from liquid metals [181]. It can be related to temperature (entropy) fluctuations within the sample and as will be shown in section 5.6 is related to the viscosity of the plasma.

Currently there are a few different ideas as to why the central peak is missing in the simulated data. Firstly, and quite simply, the middle peak may be impossible

[1]This can be demonstrated by considering scattering from unheated material, the signal from cold material is approximately three orders of magnitude smaller than from shocked material. This is due to the value of the SSF for a polycrystal, outside of a Debye-Scherrer ring the value of the SSF is exceptionally low. This was demonstrated experimentally by the need to integrate the signal from 5000 shots in order to determine the bandwidth of the system. For the data shown in Fig. 5.9 only 16 shots were used.

to capture in a MD simulation. The DSF is obtained through the Fourier transform of the particle positions in time and space, therefore just like the SSF cannot be calculated for $k = 0$ due to the need for an infinitely sized simulation, it seems obvious that to calculate the $\omega = 0$, i.e. low frequency component of the DSF, necessitates an infinitely long simulation. Appendix B details the process of obtaining the DSF from a MD simulation. In this process the long time behaviour of the intermediate scattering function is filtered to remove noise towards the end. The long time and hence low frequency behaviour could be lost within the noise in these relatively short simulations. Future work will investigate the effects of simulation length on the calculated DSF.

Secondly, the absence of the entropy peak in the QMD simulations may simply be related to the simulations being performed in the wrong ensemble, or utilising a non-physical thermostat. The simulations were performed in the iso-kinetic ensemble and utilised a Nose-Hoover thermostat. The Nose-Hoover thermostat is a deterministic way in which the kinetic energy of the system can be maintained at a constant level. In this way, the atomic motion of the system is limited to a particular surface in phase space that may not be representative of the true characteristics of the system. To explore this idea a second simulation was run with identical characteristics, with the exception of the thermostat was altered from Nose-Hoover to Langevin (also known as Gaussian) thermostat. The Langevin thermostat is a stochastic model that applies a *'kick'* to each of the atoms giving a random component to their motion. Once these random fluctuations have been Fourier transformed they appear as a central peak in the DSF. The strength of these random fluctuations is determined by the *friction* parameter in ABINIT and by altering this number the height of the middle peak can be changed. By setting it to a value of 0.003 atomic friction units ($\mathrm{Ha}/\hbar \approx 4.13 \times 10^{16}$ s^{-1}) a central peak that fits the experimental results is found, see Fig. 5.11. Through Stoke's law[2] this can be shown to be approximately equal to a dynamic viscosity of 2.36 mPa s. However, despite this success, it remains unclear whether the forced inclusion of random oscillations is physical.

Finally, it cannot be ruled out that the central peak is an experimental artefact not related to the ion dynamics. Although scattering from cold matter has been dismissed, the intensity of the X-ray beam at LCLS is so high that scattering from elsewhere in the vacuum chamber could be possible. The analysis of the data and

[2]Stoke's law can be shown to be equal to $\gamma = 6\pi\eta a/m$, where m=27 a.m.u. is the mass of an aluminium ion, a=0.125 nm is an approximate radius of an aluminium ion, $\gamma = 1.24 \times 10^{14}$ s^{-1} is the friction coefficient and η the dynamic viscosity which is equal to 2.36 mPa s.

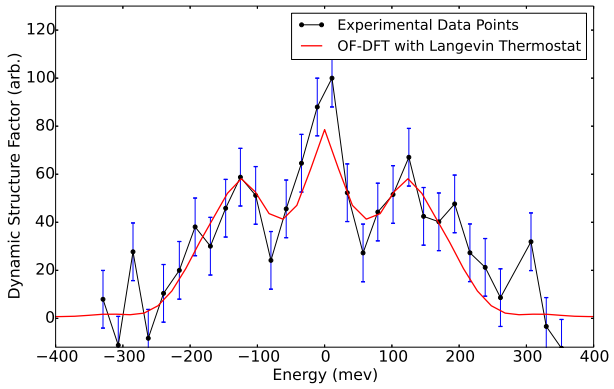

Figure 5.11: A comparison between the inelastic scattering data obtain the LCLS scattering experiment and the DSF for aluminium at a temperature of 5 eV and a density of 7 g/cm^3 taken at the corresponding k point. The simulated DSF has been scaled to match the experimental data. In this case the simulation was run using a stochastic Langevin thermostat to force the appearance of the central peak.

comparison with MD is on-going and it is not yet clear whether the central peak should be expected in the MD work or not. This result is a clear example of why experimental results are vital to help benchmark and validate theoretical models.

5.6 Analysis with Generalised Hydrodynamics

In addition to the atomistic based MD work a form of the DSF based on a continuous treatment is possible. Interpreting the experimental spectra within a hydrodynamic model can provide a valuable insight into the origin of the central peak, as well as a method to ascertain thermodynamic and transport coefficients. A hydrodynamic description has been shown to reproduce certain features of the DSF for strongly coupled liquids across a range of conditions. Mithen *et al.* (2011) [136] showed that a pure hydrodynamic description is valid for scattering wave-vectors less than $k < 0.43 * \kappa$ where κ is the inverse screening length. For the conditions relevant here, i.e. an aluminium plasma at 7 g/cc^3 and 5 eV with an ionisation level of Z=1.5, calculated from Thomas-Fermi theory, $\kappa = 2.14$ Å^{-1}. The scattering wave-vector for 8 keV X-rays at 30° is 2.1 Å^{-1} thus k/κ is approximately unity. Hence, a pure hydrodynamic description would fail. However, Mithen *et al.* noted a dramatic improvement in the range over which the hydrodynamic description could be used through the use of generalised hydrodynamics.

A generalised hydrodynamic model based on the Yukawa description of the potential includes the effects of the electrons on the ions through the screening parameter, i.e. the electrons are not explicitly treated. As such corrections must be made to some terms in the hydrodynamic model to account for the presence of a neutralising electronic background. A clear example of this is the correction to the isothermal compressibility, set out in appendix I, which without the added effect of the electrons becomes negative. The inclusion of a 'mean field' or background term is usually neglected because the length scales over which the dynamics are being probed are longer than the range of the potential. The addition of this term does not effect the dynamics of the ion-waves (height or width) but only changes the position [136, 172].

The benefit of the hydrodynamic description is that it is based on a much simpler physical picture than QMD and the origin the shape of the DSF can be more easily related to thermodynamic and transport properties. Schmidt *et al.* (2012) [179] develop from the classical hydrodynamic equations a quantum hydrodynamic description of a plasma and derive the following expression for the DSF,

$$\begin{aligned}\frac{S(k,\omega)}{S(k)/2\pi} = \frac{\gamma-1}{\gamma}\frac{c_s^2k^2}{c_s^2k^2+\omega_{p_{scr}}^2}\frac{2\epsilon_Q a k^2}{\omega^2+(\epsilon_Q a k^2)^2} + \\ \frac{\gamma^{-1}c_s^2k^2+\omega_{p_{scr}}^2}{c_s^2k^2+\omega_{p_{scr}}^2}\left[\frac{\Gamma k^2}{(\omega+c_q)^2+(\Gamma k^2)^2}+\frac{\Gamma k^2}{(\omega-c_q)^2+(\Gamma k^2)^2}\right]\end{aligned} \tag{5.2}$$

where the contribution explicitly from the quantum terms ($\propto \hbar^2/m^2$) have been neglected for the ion-ion description. Within this description the square of the peak position in the DSF is given by,

$$c_q^2 = \omega_{p_{scr}}^2 + c_s^2k^2 - \frac{\omega_p^2k^2}{\kappa^2}\,, \tag{5.3}$$

where the final term accounts for the neutralising background effect of the electrons not included in the description. The plasma frequency is replaced by the screened plasma frequency, again a consequence of the electron screening,

$$\omega_{p_{scr}} = \omega_p \times \frac{k^2}{k^2+\kappa^2}\,. \tag{5.4}$$

The final two terms which control the width of the central and side peaks, i.e. determine the transport coefficients, and are given by,

$$\epsilon_Q = (\omega_{p_{scr}}^2 + \gamma^{-1}c_s^2k^2)/c_q^2 \tag{5.5}$$

$$\Gamma = [(1 - \epsilon_Q)a + b]/2 \tag{5.6}$$

where we have defined $a = D_T\gamma$ and[3] $b = (\frac{4}{3}\eta + \zeta)/\rho$. Each of the terms in this equation is defined in table 5.6. For the case of a one-component liquid (i.e. Z=0) the plasma frequency becomes zero and Eq. 5.2 reduces to the standard classical description [179], with the peak position simply being a linear function of sound speed, $c_q = c_s k$. Furthermore, for an isothermal system ($\gamma = 1$), which is often observed in Yukawa simulations with similar screening lengths and coupling parameters used here, the widths of the three peaks take on the same form as in the classical description.

Variable	Symbol
Bulk density	ρ =7 g/cm^3
Plasma frequency	ω_p =0.15 fs^{-1}
Screened plasma frequency	ω_{p-scr} =0.10 fs^{-1}
Inverse screening length	κ =2.14 Å^{-1}
Sound speed	c_s
Ratio of heat capacities	γ
Sound attenuation coefficient	Γ
Thermal diffusivity	D_T
Shear viscosity	η
Bulk viscosity	ζ

Table 5.1: Names of the thermodynamic and transport coefficients used in the hydrodynamic model of the DSF.

The hydrodynamic DSF is then fit to the experimentally obtained spectrum utilising a non-linear least mean squares fitting algorithm in Matlab to obtain the thermodynamic and transport properties, see Fig. 5.12. The results of the fitting procedure are given in Table 5.2 along with estimates for the 95% confidence interval for each property. Given the large spread of data points due to low photon flux each variable has considerable uncertainty. It is highly interesting to note that the value obtained for the shear viscosity earlier through use of the friction parameter in the Langevin thermostat (2.36 mPa s) falls within the 95% confidence interval of the value obtained through fitting the hydrodynamic model to the experimental data.

Throughout this thesis the phrase thermodynamic and transport properties has often been used. However, at this stage it is interesting to differentiate between the two. Quantities such as the sound speed and heat capacity ratio are thermodynamic

[3]It was shown by Salin (2003) [173] that for all coupling parameters and screening lengths the bulk viscosity ζ in a Yukawa description is negligible when compared with the shear viscosity η. Therefore in this work the bulk viscosity is neglected allowing η to be calculated from b.

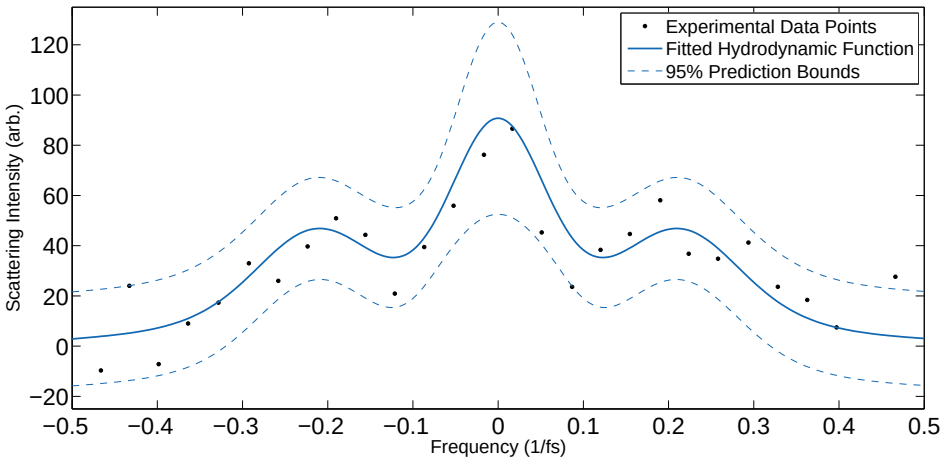

Figure 5.12: Fitting of generalised hydrodynamic structure factor to scattering spectrum performed using a non-linear least squares fit in Matlab. The upper and lower dashed lines mark the 95% confidence bounds on the fitted function.

	Units	Fitted Result	95% Confidence	Classical MD Results
k	Å^{-1}	2.1		
γ		1.79	1.18 − 2.39	1.08*, ∼1†
D_T	m^2/s	0.021	0.003 − 0.040	1.01×10^{-6} [50], 0.7×10^{-6} [146]
c_s	km/s	11.21	10.26 − 12.3	6.54*, 9.67†
η	mPa s	1.71	0.61 − 2.65	2.97 [170], 1.16 [175]

Table 5.2: Thermodynamic and transport properties of an aluminium plasma calculated by fitting the low frequency component of the scattered spectrum to a generalised hydrodynamic model of the DSF. Data shows the 95% confidence levels for each extracted property. The final column gives similar parameters extracted from parametrised EOS models based on MD simulations. Results marked (∗) use the Hamaguchi EOS for the internal energy and the derivation for thermodynamic properties given in Ref. [133] and appendix I. Results marked (†) are taken from direct numerical simulation by Mithen (2012) [133]. The transport coefficients are taken from the references given.

coefficients, that is they depend on equilibrium quantities such as the isothermal compressibility and heat capacity (see appendix I). The other two coefficients discussed in this work are the bulk viscosity η and the the thermal diffusivity D_T. These quantities are known as transport coefficients and are determined by the rate at which a non-equilibrium macroscopic quantity equilibrates throughout the system. They can be determined through investigation of current correlation functions, i.e. correlation functions that depend on particle velocity as opposed to density.

A huge number of MD calculations based on the classical Yukawa potential have

been performed in the past [50, 83, 84, 133, 146, 170, 173, 175] and both thermodynamic coefficients and transport coefficients extracted. The coefficients extracted from the numerical simulations are parametrised through the ion-ion coupling parameter and the screening length. Therefore, without explicitly running an MD simulation the values for the coefficients can be determined from these parameterisations, details are given in appendix I. The thermodynamic coefficients are parametrised through the internal energy while the transport coefficients have been parametrised directly. Since these simulations use a Yukawa potential, as opposed to a potential containing short-range repulsion, we can immediately hypothesis that not all the terms will be correct. However, the existence of this body of work coupled with the hydrodynamic model gives a complete analytical form of the DSF, a fact that could have huge implications for the planning and analysis of scattering experiments.

The rightmost column in Table 5.2 contains the parametrised values obtained from MD simulations. Beginning with the thermodynamic coefficients we see that both c_s and γ, marked with $*$, differ considerably from the fitted results. These coefficients depend strongly on the parameterisation of excess internal energy developed by Ohta and Hamaguchi (2000) [146]. It has, however, been noted previously that this EOS model does not reproduce the sound speed found in classical MD data above $\kappa = 1$. Therefore, also included are the results extracted directly from numerical evaluation, marked with †. This numerically based result is significantly closer to the value obtained by fitting the experimental data, thus suggesting an error in the parametrisation of internal energy by Hamaguchi. The difference between the numerical and fitted results is now similar to the difference observed in chapter 4 through the neglection of the SRR. One could therefore expect that a parametrisation of the sound speed based on results from a classical Yukawa with SRR could accurately predict the measured sound speed. The ratio of heat capacities from the Hamaguchi model agrees well with the numerical MD simulations, in so far that no middle peak is visible in the data. Both disagree strongly with the fitted experimental value. However, a lower value for γ than seen experimentally is yet again a statement that when comparing MD simulations with scattering signals the central peak is missing. As before, whether this is related to ensemble choice, thermostat choice, the long time-scale behaviour of the intermediate scattering function or simply an experimental feature remains to be seen.

The final two terms are the shear viscosity η and the thermal diffusivity D_T. The shear viscosity term is calculated from parametrisations given by Saigo and Hamaguchi (2002) [170] and Sanbonmatsu and Murillo (2007) [175]. The the thermal

diffusivity term is calculated from Ohta and Hamaguchi (2000) [146] and Donkó and Hartmann (2004) [50] where in the latter case, D_T is converted from values for the thermal conductivity λ through $D_T = \lambda/c_p$, in which c_p the volumetric heat capacity at constant pressure. The value obtained for D_T is around four orders of magnitude larger than the value obtained from the MD fit. Comparing the value obtained from the fit with typical metals it is clear that this number is grossly overestimated in the fitting procedure. Investigating the hydrodynamic description, Eq 5.2, the thermal diffusivity is related the the width of the central peak. Fig. 5.9 demonstrates clearly that the width of this peak is very close to that of the instrumentation function. Therefore, given the current experimental limits it is probably not possible to extract this number from the current data, on the other hand, the shear viscosity is determined primarily by the width of the ion-acoustic peaks. In this case the width of these peaks is wider than the instrumentation function and correspondingly a value can be obtained from the fit. It is of the same order of magnitude as the that from MD, thus suggesting the shear viscosity is captured accurately in the numerical simulations.

For the shear viscosity term the agreement between the extraction and MD parameterisation is important as a minimum bound on the shear viscosity is predicted from these simulations. This minimum bound occurs at $\hat{\eta}\sim 0.09$ for $\kappa^* \sim 0, \Gamma_{ii} \sim 5$ and falls to $\hat{\eta}\sim 0.02$ for $\kappa^* \sim 2, \Gamma_{ii} \sim 80$. Here, $\hat{\eta}$ is the reduced viscosity given by $\eta = \hat{\eta} m n_i \omega_p a^2$ which is given by $\eta = \hat{\eta} \times 14$ mPa s [175]. This puts the limits on the shear viscosity mentioned before at 1.26 mPa s and 0.28 mPa s, respectively. Unfortunately this experiment is far from the regime of the minimum bound on shear viscosity having a reduced screening parameter of $\kappa^* = 2$ and an ion-ion coupling parameter of $\Gamma_{ii} = 5.6$. However, now that a measure of the shear viscosity in a dense plasma has been demonstrated, this lower bound suggests a particularly interesting region of temperature−density phase space that could be accessed in future experiments.

5.7 Conclusions

In this chapter the results of an inelastic X-ray scattering experiment performed at the matter in extreme conditions (MEC) end-station at the LCLS FEL have been presented. Utilising the self-seeded mode of the laser a set-up containing a Si (444) crystal monochromator and a diced crystal analyser placed at a 30° scattering angle measured the spectrum to an unprecedented resolution of 100 meV. With this ultra-high resolution the inelastic components of the scattered light from the low frequency ion modes in an opaque sample were resolved for the first time. A direct comparison

between the experimentally measured spectrum and the ion component of the DSF calculated in chapter 4 was performed. The data collected during this experiment will act as a useful guide for the OF-DFT work, giving confidence in the calculation of the sound speed (through correct estimation of the peak position) but highlighting a discrepancy in the prediction of the middle peak. Work is currently on-going to determine why this feature is not seen in the models and focussing on the behaviour of the ensemble, thermostat settings, as well as the long time behaviour of the intermediate scattering function. However, at this stage it cannot be ruled out as an experimental feature.

An analytic approach to interpreting the data was performed through the generalised hydrodynamic model. The fitting of the data demonstrates the power of this technique and the possibility to provide an analytic model for the DSF, at least one that requires some parameterisation from numerical MD simulations. This technique was used to provide the first measure of shear viscosity in a dense plasma and paves the way for future experiments. Comparison between the fitted data and the numerical data suggested that the parameterisation of sound speed and shear viscosity from the simulations would be successful, but again a discrepancy in the heat capacity ratio was found. This finding adds weight to the suggestion that if a central peak should be present in the spectrum it is missing not just from the OF-DFT work but also the classical simulations utilising a Yukawa potential.

The low number of photons collected during this experiment, a consequence of the small Thomson cross-section and low value of SSF, led to a large number of shots being required to obtain the total scattered spectrum. This factor, coupled with the low repetition rate of the optical laser ($\sim$10 minutes) and the relatively time consuming process of correctly seeding the FEL meant that only two scattering spectra were obtained in a full 5 day campaign. Now that the concept of measuring inelastic scattering from low frequency ion modes in WDM has now been demonstrated experimentally, future work will concentrate on measuring the full dispersion curve at high accuracy necessary for a direct comparison with theoretical models. Future proposals hope to take advantage of multiple crystal analysers to measure the scattering spectrum at multiple k points simultaneously. In addition, simultaneous measurement of the SSF with measurements of the DSF would allow the temperature and density of the samples to be obtained via a separate technique, and hence input into the OF-DFT code. They would no longer need to be inferred from hydrodynamic models which may be incorrect due to dimensional effects or poor laser-absorption models.

Chapter 6

Conclusions and Future Work

This thesis has detailed the investigation of the low frequency ion dynamics in the warm dense matter regime, a regime defined by temperatures of a few electron volts and densities comparable with solids. A complete description of the WDM regime is important for describing many physical phenomena ranging from phase transitions within the interior of large astrophysical objects [40] to temperature relaxation rates during the internal processes of ICF [127]. Efforts to describe the structural dynamics of the cores of these so called exoplanets, as well as those within our solar system are an area of intense scientific interest.

Chapter 3 details three different experiments, each employing time-resolved X-ray scattering techniques, to directly measure temperature relaxation in a bulk sample after heating with an intense proton beam, electron beam or direct laser illumination. These experiments are vital as they not only aid our understanding of experiments designed to create the WDM states but also provide an insight into fundamental internal processes such as electron-ion coupling. The first two experiments on graphite samples occur at large excitation densities, i.e. they are strongly heated, and an inhibited electron-ion coupling was found. For the proton heated samples an electron-ion equilibration constant of $g = 0.45 - 0.8 \times 10^{16}$ W K^{-1} m^{-3} was found, while in the samples heated with a high intensity electron beam a constant of $g = 0.2 \times 10^{16}$ W K^{-1} m^{-3} was found. Both these results are lower than those expected from simple metal or ideal plasma models, and although close to values found in room temperature graphite and graphene systems they are still somewhat lower. The typical explanation as to why graphite exhibits long temperature relaxation times revolves around the low carrier number in semi-metals, an explanation that does not hold at the high electron temperatures present in these experiments. Instead, it was proposed that the effective electron-ion interaction is suppressed by virtue of a dynamical coupling of electron

and ion modes, an idea first detailed by Dharma-Wardana and Perrot in 1998 [47]. However, it should be noted that the coupling constant is in fact not constant and is predicted to vary with both electron and ion temperature, more experiments are needed to probe how this constant varies and further guide the choice of equilibration model.

The final section of chapter 3 continues to investigate temperature relaxation, but in a lower energy density regime. A 200 nm single crystal gold sample was heated through direct laser illumination. The resultant electron-ion equilibration was found to occur on a picosecond time-scale and was diagnosed through comparison of the time-resolved diffraction signal with large scale molecular dynamics simulation. The determined value for τ leads to an electron-phonon equilibration constant of $g = 2 \pm 1.2 \times 10^{16}$ W m $^{-3}$ K^{-1}, a value which is in close agreement with previous studies. The accuracy of this method, through comparison with previous results for gold, demonstrates the capability of large-scale molecular dynamics simulations to accurately capture the dynamics in a non-equilibrium system. Although in this case it was utilised for samples near to equilibrium, future work will involve highly non-equilibrium samples excited to large energy densities. This is crucially important when looked at in light of the preceding experiments when the low frequency ion motion and long-range structure strongly effect equilibration rates. The ability to perform simulations that can capture this long wavelength ion motion in a dynamically evolving sample is essential to evaluate equilibration rates within the coupled mode formalism. This work highlights the possibility to study energy relaxation processes in bulk samples through large-scale MD simulations and could be particularly successful at describing the complex ion-ion correlations [110, 123] which make experiments with higher excitation densities difficult to describe [77, 200].

In chapter 4 a method of calculating the ion dynamics in a dense plasma through a reduced DFT description was described. By utilising this orbital-free technique the computational time associated with the more accurate Kohn-Sham molecular dynamics is significantly reduced. This reduction allows calculations involving large systems with many thousands of atoms to be simulated for long time-scales of many picoseconds. Both static and dynamic properties for a trial system of a solid density aluminium plasma at 0.5 eV and 5 eV were calculated. The orbital free approach reproduces well the KS-DFT thermodynamic pressure above $\approx$ 2 eV and also reproduces the static structure factor of the 5 eV test case, i.e. it works well in systems where atomic orbitals becomes less important. This work is the first confirmation that the orbital-free technique can be used to extract dynamic plasma properties

in the WDM region of phase space. The density-density autocorrelation function, also known as the ion-ion dynamic structure factor, was then computed for classical, orbital-free and, in the 0.5 eV case, Kohn-Sham techniques. The DSF is an important quantity with direct relevance to interpreting X-ray scattering experiments. The classical simulations based on pure classical Yukawa potential are unable to describe the dynamics of the aluminium systems, while there is good qualitative agreement between the Yukawa+SRR potential and the OF-DFT. However, the applicability of the classical method is limited by the fact that the ion-ion potential must be known *a-priori*. Finally, a full KS-DFT calculation was compared with the OF-DFT results for the 0.5 eV test case and shown to qualitatively agree, however, at these low temperatures the differences can be attributed to the lack of atomic orbitals in this method. In the future, as computational power increases and KS-DFT can access higher temperature and density states, OF-DFT will always be able to access larger regions of phase space, or run many more simulations, than the more complete KS-DFT theory.

The DSF is an important quantity as it feeds into many theoretical models for thermodynamic and transport properties of dense plasmas, crucially the coupled mode formalism for temperature relaxation depends on the ion dynamics through this function. While a number of different theoretical approaches have been proposed to describe the DSF, none to date have used self-consistent quantum simulations. Additionally, the methods used here can describe large systems both spatially and temporally, i.e. it can capture accurately the low frequency ion response. This is important when attempting to describe or even predict the low wave-number small angle X-ray scattering from a target. The results obtained in this thesis agree well with the more accurate Kohn-Sham method in regimes where both can be calculated, i.e. at lower temperatures or in the static response, however experimental verification was necessary.

The proof-of-principle experiment outlined in chapter 5 represents the first ever experimental measurement of ion waves in the WDM regime. Although the data is relatively noisy due to low photon flux, the qualitative agreement between the OF-DFT peak position and the experimentally measured spectrum is promising. This suggests that the orbital-free method accurately describes the low frequency ion waves and accurately captures the sound speed within the sample. However, the absence of a middle peak in the simulations raises concerns over the applicability of MD and future work should concentrate on investigating the effect of changing ensemble,

thermostat settings as well as the long time behaviour of the intermediate scattering function. However, at this stage it cannot be ruled out as an experimental feature.

A continuous, as opposed to an atomistic model, of the DSF was obtained from generalised hydrodynamics and used to fit the scattered spectrum. The thermodynamic properties, sound speed and heat capacity ratio, were determined to a high level of accuracy, as they are given by the relative height and position of the peaks. The transport coefficients which are given through the width of the peaks were also determined and a value for the shear viscosity was found, however the thermal diffusivity was unable to be extracted due to poor experimental resolution. Combining the generalised hydrodynamic structure factor with parametrised values of the thermodynamic and transport functions from classical MD provides an analytic form of DSF which would be a powerful tool in interpreting experimental data. For the conditions considered here the MD results were shown to agree well with the sound speed and shear viscosity. The thermal diffusivity was again unable to be reliably compared. However, the heat capacity ratio disagreed considerably. This again points to a fundamental flaw in the MD simulations or misinterpretation of the experimental results.

The success of this experiment paves the way for future low frequency scattering experiments to be performed at the LCLS. This work should concentrate on measuring multiple scattering angles to obtain the dispersion relation to high accuracy, thus helping to discriminate between theoretical models. Additionally, achieving a higher resolution on the experiment would reveal the width of the middle peak and allow the thermal diffusivity to be determined. In addition to this, improved laser stability, faster self-seeding, increased bandwidth and on-shot temperature and density diagnostics would considerably improve the experiment. Finally, an area of temperature-density space exhibiting a lower bound on shear viscosity was identified as a possible area to probe in future experiments.

A central theme running throughout this work has been the interplay between experimental work and computer simulation. Both where simulations have helped to inform and interpret experimental results (chapter 3) and where experimental results were needed to help validate a new theoretical model (chapters 4 and chapter 5). This interplay is nothing new in physics, and can perhaps be thought of as a core component of modern day scientific method, but with rapid growth in computational power and advancement of fourth generation light sources we have reached a crucial point where comparable temporal and spatial length scales relevant to HEDP can be accessed both experimentally and in computational simulations. By implementing

these techniques it should be possible to improve the quality of both the experimental data to help distinguish between differing theoretical models, an important stepping stone towards the goal of a complete description of WDM.

Appendix A

Scattering of X-rays from a Bound Electron

This appendix will derive the form of the Thomson scattering cross section as detailed in [30]. To begin with we define the electric field of an electromagnetic wave as,

$$\mathbf{E}(\mathbf{r},t) = \mathbf{e_i} E e^{i(\mathbf{k}\cdot\mathbf{r}-\omega t)}\,, \tag{A.1}$$

where $\mathbf{e_i}$ is the polarization vector[1]. The electromagnetic wave excites an electron of mass m_e, the equation of motion of this electron is that of a forced dipole oscillator,

$$m_e\ddot{x} + m_e\omega_r^2 x - m_e\gamma\dot{x} = e\mathbf{E}(t)\,, \tag{A.2}$$

where γ is a damping constant and ω the eigenfrequency of the electron. The solution to this equation describes forced damped oscillations,

$$\mathbf{s}(t) = \frac{e}{m_e}\frac{1}{\omega_r^2-\omega^2-i\gamma\omega}\cdot\mathbf{E}(t)\,. \tag{A.3}$$

The electron oscillation has an electric dipole moment given by,

$$\mathbf{p}(t) = e\mathbf{s}(t) = \alpha(\omega)\mathbf{E}(t)\,, \tag{A.4}$$

where $\alpha(\omega)$ is the polarisability,

$$\alpha(\omega) = \frac{e^2}{m_e}\frac{1}{\omega_r^2-\omega^2-i\gamma\omega}\,. \tag{A.5}$$

The oscillating electron emits its own electromagnetic field which at large distances from the emitter is given by[102],

[1]For a transverse wave $\mathbf{e}_i\cdot\mathbf{k}=0$ is true.

$$\mathbf{E}_d(\mathbf{r},t) = -\frac{1}{c^2}\frac{1}{r}(\ddot{\mathbf{p}}(t) - (\mathbf{p}\cdot\mathbf{e}_r)\mathbf{e}_r)\,. \tag{A.6}$$

The ratio of outgoing electric field to incoming electric field can be expressed as,

$$\left|\frac{\mathbf{E_d}}{E_i}\right| = \frac{1}{r^2}\frac{\omega^4}{c^4}|\alpha(\omega)|^2|\mathbf{e}_i - (\mathbf{e}_i\cot\mathbf{e}_r)\mathbf{e}_r|^2 = \frac{1}{r^2}|f(\Omega)|^2\,. \tag{A.7}$$

Simplifying $|\mathbf{e}_i-(\mathbf{e}_i\cot\mathbf{e}_r)\mathbf{e}_r|^2$ to $(1+\cos^2\theta)$ which holds for unpolarized radiation allows the average of all polarization directions to be calculated. This gives the total scattering cross section,

$$\frac{d\sigma}{d\Omega} = |f(\theta\omega)|^2 = \frac{1}{2}(1+\cos^2\theta)\frac{\omega^4}{c^4}|\alpha(\omega)|^2\,. \tag{A.8}$$

Depending on the frequency of the incoming electromagnetic radiation compared to the eigenfrequency of the electron, three distinct regimes of interaction can be identified.

- Rayleigh scattering,

$$\omega << \omega_r: \quad |\alpha(\omega)| \approx \frac{e^4}{m_e^2\omega_r^4} \tag{A.9}$$

- Resonance scattering,

$$\omega <\sim \omega_r: \quad |\alpha(\omega)| \approx \frac{e^4}{m_e^2\gamma^2\omega_r^2} \tag{A.10}$$

- Thomson scattering,

$$\omega >> \omega_r: \quad |\alpha(\omega)| \approx \frac{e^4}{m_e^2\omega^4} \tag{A.11}$$

For X-rays above a few keV (known as hard X-rays) the frequency of the incoming radiation is much higher than any resonance frequency of the electron and hence the cross section tends towards the frequency independent value of,

$$\left(\frac{d\sigma}{d\Omega}\right)_{Th} == \frac{1}{2}r_e^2(1+cos^2\theta) \tag{A.12}$$

where $r_e = \frac{1}{4\pi\epsilon_0}e^2/mc^2 = 2.8\times10^{-15}$ m.

Appendix B

Structure Factor Calculation Software

As discussed in detail in chapter 2.2 the relationship between scattered radiation and the microstate of the system is given by the DSF. The DSF is the spatial and temporal Fourier transform of the dynamic electron density-density auto-correlation function. It is essentially the Fourier transform of the atom positions in both time and space. Therefore, predicting the direction of scattered radiation (diffraction pattern) and the scattering spectrum from a MD simulation requires performing large three dimensional Fourier transforms. Mathematically this relates to transforming a large (number of time steps in the simulation) number of $3 \times N$ arrays.

In one dimension the Fourier transform can be written as,

$$f(\mu) = \int_{-\infty}^{\infty} f(t)\ e^{-2\pi i \mu t}\, dt, \tag{B.1}$$

where t represents the real space variable and μ the reciprocal variable. Obviously the data obtained from MD is discrete in nature, and we must perform a discrete Fourier transform as given by,

$$F_n = \sum_{n=0}^{N-1} f_k e^{-2\pi i n k/N}. \tag{B.2}$$

Just like the continuous version of the Fourier transform the discrete Fourier transform reveals the strength of the frequency components associated with the input data. However, some care must be taken when analysing discrete Fourier transforms. Firstly, if the input list is a set of real numbers the output will be a set of complex numbers of the same length. Additionally, the list will contain both positive and negative frequency components.

To enable fast and simple calculation of the static and dynamic structure factors a graphical software program (skcalc.py) was written in the python scripting language. This software allows output files from various MD programs to be loaded and the Fourier transform of the data to be calculated and output as standard text files. At the time of writing the software is able to accept inputs in the standard xyz file format and the output directly from the LAMMPS software program. In addition to this the atom locations can be read directly from the hard drive during the processing or loaded first into random access memory (RAM). While loading the data into RAM expedites the analysis, for large simulations the size of the dump file can make this prohibitively expensive.

Once the atom positions have been parsed into an array of size $3 \times T$ where T is the number of time-steps in the simulation the next step necessary to perform the Fourier transform is to calculate the allowed k-vectors that are commensurate with the simulation size. That is the k-vectors which obey the relation,

$$\mathbf{k} = \frac{2\pi}{L}(n_x, n_y, n_z)\,, \quad |\mathbf{k}| \leq k_{max}, \tag{B.3}$$

where $n_{x,y,z}$ are natural integers and k_{max} some predefined maximum for the calculation[1].

The second step in the software is to calculate the Fourier transform of the atom positions at each time step according to Eq. (B.4),

$$\hat{\rho}(\mathbf{k}, t) = \sum_{i=1}^{N} e^{-i\mathbf{k}.\hat{\mathbf{r}}_i(t)}. \tag{B.4}$$

The results are stored in a $T \times N_k$ array where T is the total number of time-steps and N_k the number of k-vectors to be analysed. A typical simulation will contain of the order of 10^3 time-steps and a similar number of atoms. This typically leads to a box size of the order of 10 Å, and for a k_{max} of 10 Å^{-1} this leads to around 10^4 k-vectors. Therefore, this calculation can take many hours to run on a typical desktop pc. To prevent this calculation needing to be run on each simulation every time a new DSF is required this array is saved to the hard drive at this stage in the calculation, the size of this file is typically of the order of 100 Mb. Metadata concerning the details of the calculation are saved alongside this file such that the

[1]The skcalc.py software allows the user to choose the dimension of the calculation. For example it can be run with the k-vectors spanning either 1, 2 or 3 dimensions. This can be used to significantly speed up the software with a corresponding reduction in the k-space fidelity of the results. In addition this feature allows the structure factors to be calculated along a single direction for non-isotropic materials and non-cubic simulations.

software can open this data without requiring the original dump file from the MD software.

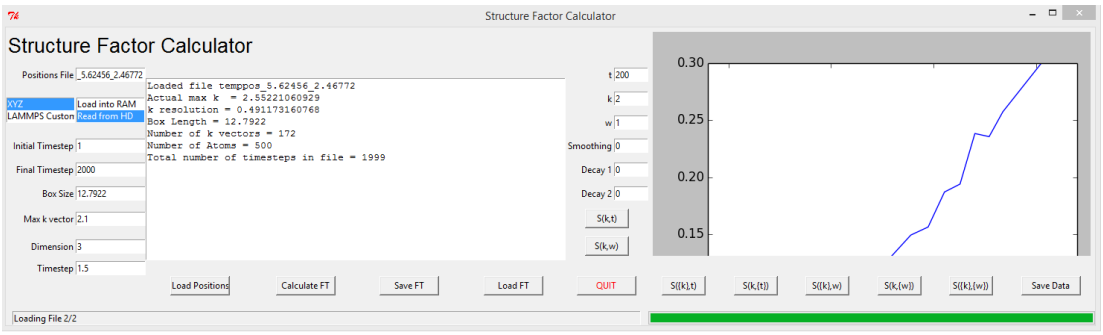

Figure B.1: Screenshot of software for calculating the static or dynamic structure factor from a molecular dynamics simulation.

The final stage in the calculation is to choose which function to calculate, either the static or dynamic structure factor. However, all calculations start by calculating the intermediate scattering function (ISF) given by,

$$F(\mathbf{k},t) = \int_{-\infty}^{\infty} G(\mathbf{r},t)e^{-i\mathbf{k}.\mathbf{r}}\,\mathrm{d}\mathbf{r} = \frac{1}{N}\langle\hat{\rho}(\mathbf{k},0)\hat{\rho}(-\mathbf{k},t)\rangle_T. \tag{B.5}$$

At this stage of the calculation an isotropic simulation is assumed and results from k-vectors with equal magnitude are loaded from the hard drive and averaged to enable the calculation of the ISF. The effect of averaging the k-vectors at this stage greatly reduces the statistical noise present in the data as up to 16 k-vectors can be used for a single calculation.

Typically there exists numerical noise towards the end of the ISF and it is common practice to filter this noise before further analysis. It has been shown previously by Mithen *et al.* [133] that this filtering does not effect the final result but acts as a high frequency filter on the data. Once the ISF has been obtained a fast Fourier transform algorithm is used to obtain the DSF and from this the SSF can be obtained through integration. The benefit of this software is that once the initial, and time consuming, Fourier transform has taken place any of the other calculations can be performed instantly allowing for greater flexibility when analysing the data.

Appendix C

Orbital-Free Pseudopotential Development Wrapper

This appendix provides details of calculating a local pseudopotential from a non-local pseudopotential using the method outlined in section 4.3.2.1. This method minimises the negative of the Wu functional in a bulk sample to obtain the local-potential. By performing these calculations in a bulk sample the returned pseudopotential has been shown to give greater transferability, principally due to getting the exchange and correlation correct. The Wu functional as described in the main text is given by,

$$W[v_{eff}] = T_s[v_{eff}(\mathbf{r})] + \int (\rho(\mathbf{r}) - \rho_{in}(\mathbf{r}))v_{eff}(\mathbf{r})d\mathbf{r}\,. \tag{C.1}$$

where ρ_0 is a target electron density calculated with Kohn-Sham DFT, v_{eff} a trial local potential and T_s and ρ the resulting kinetic energy and electron density obtained after solving the Kohn-Sham equations for an identical system. The core of the program is a GA which can minimise the negative of the Wu functional with respect to the trial potential described by a sum of zeroth order Bessel functions of the first kind,

$$V_{nc}(q) = \sum_{i=1}^{L} A_i J_0(q\alpha_i)\,. \tag{C.2}$$

In this formalism L is the number of functions in the series, A_i are the Bessel function coefficients to be minimised, J_0 the zeroth order Bessel function of the first kind and α_i the positive roots of the zeroth order Bessel function.

The base element in a GA is the chromosome. In biology a chromosome defines the characteristics of an organism, in this case it defines the characteristics of a particular

solution to the problem. Hence, the chromosome here is the list of Bessel function coefficients, A_i, that together describe the potential. A group of chromosomes is known as a population. The function to be minimised, known as the evaluator function, is then calculated for each chromosome in the population and a fitness function converts this into a number between 0 and 1 representing the 'fitness' of each individual. The evaluator function in this case is the negative of the Wu functional.

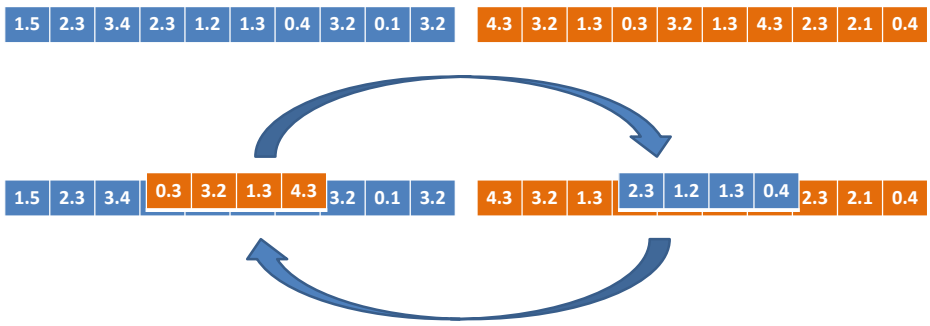

Figure C.1: Schematic of crossover breeding in a genetic algorithm. Shown are two parent chromosomes which are subjected to a two point crossover.

At this stage the next generation of individuals can be created from the preceding generation using selection rules, the two most common are *rank selection*, in which the chromosomes with the highest fitness function are selected, and *roulette wheel* in which individuals are chosen randomly with a probability proportional to the value of the fitness function. These chosen chromosomes, called the parent chromosomes, are then bred to produce the next generation of solutions by choosing components from each of the parents in a process known as crossover. This takes two or more chromosomes and swaps together sections of them as shown in Fig. C.1. Finally, the new generation is subjected to an amount of random mutation, it is this ability which allows the GA to search new areas of phase space for further solutions and prevents the algorithm getting stuck in a local minima.

The actual program is written in fully object orientated python and acts as a wrapper to the open source DFT software *ABINIT*. Below is an example input deck from the program which allows the user to change to parameters associated with the DFT and the GA.

```
################ GA_deck.py ##############################
#Abinit Options
```

```
acell = 5.0675                  #Or 7.5275 for fcc lattice
ecut = 25.0                     #Gives < 0.1meV convergence for this potential
kpts = 20                       #Equivalent to Carter
kspotfile = '13al.pspnc'        #Non-Local pseudo-potential to use
XCtype = 'GGA'                  #Type of exchange and correlation
crystaltype='sc'                #'sc' ;'fcc' ; 'bcc' are currently implemented
fullrun = True                  #Turn 'On'=True or 'Off'=False minimisation


#Create Potential Options
from potential import bess_pot as functype    # sets basis: only "bess_pot" is currently
    implemented
Z_val = 3.0                     #Number of electrons in nonlocal-pseudopotential
Z_full = 13.0                   #Atomic number
qc = 5.60                       #Apply function that smooths to 0 in reciprocal space
rc = 6.5                        #Apply function that smooths to 0 in real space at this cutoff
penlambda=0                     #Smoothing function to help minimisation (unused)
intfact = 160                   #Number of points for quadrature integration
ncoef = 14                      #Number of coefficients for potential
autoqc = True                   #Turn 'On'=True or 'Off'=False minimisation vs coefs and qc

#GA options
populationsize = 16             #Population size. Make a multiple of number of cores
crossoverrate = 0.8             #Cross over rate for genetic algorithm
mutationrate = 0.2              #Mutation rate for genetic algorithm
numgenerations = 3              #Max number of generations
gauss_fwhm = 0.05               #Max amount of broadening of mutations


from numpy import array
weighting = array((15,15,15,10,10,10,5,5,5,2,2,2,2,2,10),dtype='float64')
exedir = '/path/to/executables'
```

The first step in the program is to create the ABINIT input deck using the variables from the GA input deck and run a single time-step of a full Kohn-Sham calculation. This is done for a trial solid system, however the specific crystal structure used has no effect on the resulting potential [96]. The electronic density output from the simulation is saved to a file. The next step is to create the first generation of chromosomes, this is done by randomly choosing the Bessel function coefficients but scaling them to approximately the correct shape using the weighting coefficients at the bottom of the input deck. While this step is not necessary there is a resulting speed up finding the correct solution. This generation of local pseudo-potentials are then each used to perform an ABINIT run that differs from the first in two ways. Firstly, the self-consistent field calculation is not needed since the correct electronic density is known *a-priori* and can be read from the full calculation. Secondly, the calculation of kinetic energy is performed using the Thomas-Fermi functional as in the orbital free calculations described in the main text. Each of these calculations are performed on a separate core of the machine and hence the calculation is trivially parallelisable. The number of chromosomes in each population should be a multiple of the number of processors for the most efficient parallelisation.

For each of the calculations the Wu functional is calculated. An exponential evaluator function and rank selector algorithm creates the next generation of potentials and the process is repeated. Potentials that match those found in the literature are generally found within a few hours, see Fig. 4.1 in chapter 4.

Appendix D

Derivation of the Debye-Waller Theory

From chapter 2 we can define the microscopic density operator as,

$$\hat{\rho}(\mathbf{r},t) = \sum_{i=1}^{N} \delta(\mathbf{r} - \hat{\mathbf{r}}_i(t)) \,. \tag{D.1}$$

The van Hove function or dynamic density-density auto-correlation function can be defined as,

$$G(\mathbf{r},t) = \frac{1}{N} \int \langle \hat{\rho}(\mathbf{r}' + \mathbf{r}, t) \hat{\rho}(\mathbf{r}', 0) \rangle_T d\mathbf{r}' \,, \tag{D.2}$$

which becomes,

$$G(\mathbf{r},t) = \frac{1}{N} \langle \sum_{i=1}^{N} \sum_{j=1}^{N} \delta(\mathbf{r} - \hat{\mathbf{r}}_i(t) + \hat{\mathbf{r}}_j(0)) \rangle_T \,, \tag{D.3}$$

for a translationally invariant system. From chapter 2 the intermediate scattering function, dynamic and static structure factors are then defined as follows,

$$F(\mathbf{k},t) = \int_{-\infty}^{\infty} G(\mathbf{r},t) e^{-i\mathbf{k}.\mathbf{r}} \, \mathrm{d}\mathbf{r} \,, \tag{D.4}$$

$$S(\mathbf{k},\omega) = \frac{1}{2\pi} \int_{-\infty}^{\infty} \int_{-\infty}^{\infty} G(\mathbf{r},t) e^{-i\omega t} e^{-i\mathbf{k}.\mathbf{r}} \, \mathrm{d}t \mathrm{d}\mathbf{r} \,, \tag{D.5}$$

$$S(\mathbf{k}) = \int_{-\infty}^{\infty} S(\mathbf{k},\omega) \, \mathrm{d}\omega = F(\mathbf{k},0) \,. \tag{D.6}$$

Splitting the atomic motion into three components, the equilibrium lattice position $\mathbf{R}_i$, the oscillatory motion $\hat{\mathbf{u}}_{oi}(t)$ and the translational motion $\hat{\mathbf{u}}_{ti}(t)$ the SSF can be rewritten as,

$$\hat{\mathbf{r}}_i(t) = \mathbf{R}_i + \hat{\mathbf{u}}_{oi}(t) + \hat{\mathbf{u}}_{ti}(t) \,, \tag{D.7}$$

$$S(\mathbf{k}) = \frac{1}{N}\sum_{i=1}^{N}\sum_{j=1}^{N}\langle e^{-i\mathbf{k}.[\mathbf{R}_i+\hat{\mathbf{u}}_{oi}+\hat{\mathbf{u}}_{ti}-\mathbf{R}_j-\hat{\mathbf{u}}_{oj}-\hat{\mathbf{u}}_{tj}]}\rangle_T\,, \tag{D.8}$$

where we have written $\hat{\mathbf{u}}_{oj}(0)$ as $\hat{\mathbf{u}}_{oj}$. Exploiting the linear property of the canonical average to split up the terms assuming the oscillatory motion and translational motion are decoupled and statistically independent. i.e. there is no covariance between them [79]. This is equivalent to,

$$\begin{gathered}\langle e^{-i\mathbf{k}.[\hat{\mathbf{u}}_{oi}-\hat{\mathbf{u}}_{oj}]}\, e^{-i\mathbf{k}.[\hat{\mathbf{u}}_{tk}-\hat{\mathbf{u}}_{tj}]}\rangle_T = \\ \delta_{ik}\langle e^{-i\mathbf{k}.[\hat{\mathbf{u}}_{oi}-\hat{\mathbf{u}}_{oj}]}\rangle_T\langle e^{-i\mathbf{k}.[\hat{\mathbf{u}}_{tk}-\hat{\mathbf{u}}_{tj}]}\rangle_T\end{gathered}\,, \tag{D.9}$$

which allows the SSF to be simplified as,

$$\begin{aligned}S(\mathbf{k}) = \frac{1}{N^2}&\left(\sum_{i=1}^{N}\sum_{j=1}^{N} e^{-i\mathbf{k}.[\mathbf{R}_i-\mathbf{R}_j]}\,\langle e^{-i\mathbf{k}.[\hat{\mathbf{u}}_{oi}-\hat{\mathbf{u}}_{oj}]}\rangle_T\right)\\ &\times\left(\sum_{k=1}^{N}\sum_{l=1}^{N}\langle e^{-i\mathbf{k}.[\hat{\mathbf{u}}_{tk}-\hat{\mathbf{u}}_{tl}]}\rangle_T\right)\end{aligned}\,, \tag{D.10}$$

$$S(\mathbf{k}) = \frac{S_t(\mathbf{k})}{N}\left(\sum_{i=1}^{N}\sum_{j=1}^{N} e^{-i\mathbf{k}.[\mathbf{R}_i-\mathbf{R}_j]}\, e^{\frac{-\mathbf{k}^2}{2}.\langle[\hat{\mathbf{u}}_{oi}-\hat{\mathbf{u}}_{oj}]^2\rangle_T}\right)\,, \tag{D.11}$$

$$S_t(\mathbf{k}) = \frac{1}{N}\sum_{i=1}^{N}\sum_{j=1}^{N}\langle e^{-i\mathbf{k}.[\hat{\mathbf{u}}_{ti}-\hat{\mathbf{u}}_{tj}]}\rangle_T\,, \tag{D.12}$$

where (D.12) is defined as as *translational* structure factor. Using approximation (D.13) which applies provided x has a Gaussian distribution or is small [202] to simplify the expression further.

$$\langle e^{ix}\rangle = 1 + i\langle x\rangle - \frac{1}{2}\langle x^2\rangle - \frac{1}{6}i\langle x^3\rangle + ... = e^{\frac{-\langle x^2\rangle}{2}}\,, \tag{D.13}$$

$$S(\mathbf{k}) = \frac{S_t(\mathbf{k})}{N}\left(\sum_{i=1}^{N}\sum_{j=1}^{N} e^{-i\mathbf{k}.[\mathbf{R}_i-\mathbf{R}_j]}\, e^{\frac{-\mathbf{k}^2}{2}.\langle[\hat{\mathbf{u}}_{oi}(0)-\hat{\mathbf{u}}_{oj}(0)]^2\rangle_T}\right)\,, \tag{D.14}$$

$$S(\mathbf{k}) = \frac{S_t(\mathbf{k})}{N}\left(\sum_{i}^{N}\sum_{j}^{N} e^{-i\mathbf{k}.[\mathbf{R}_i-\mathbf{R}_j]}\, e^{\frac{-\mathbf{k}^2}{2}.[\langle\hat{\mathbf{u}}_{oi}^2\rangle_T-2\langle\hat{\mathbf{u}}_{oi}\hat{\mathbf{u}}_{oj}\rangle_T+\langle\hat{\mathbf{u}}_{oj}^2\rangle_T]}\,,\right) \tag{D.15}$$

$$S(\mathbf{k}) = \frac{S_t(\mathbf{k})e^{-2\mathbf{W}}}{N}\left(\sum_{i}^{N}\sum_{j}^{N} e^{-i\mathbf{k}.[\mathbf{R}_i-\mathbf{R}_j]} + \sum_{i}^{N}\sum_{j}^{N} e^{-i\mathbf{k}.[\mathbf{R}_i-\mathbf{R}_j]}\,[e^{\mathbf{k}^2.\langle\hat{\mathbf{u}}_{oi}\hat{\mathbf{u}}_{oj}\rangle_T}-1]\,,\right) \tag{D.16}$$

where we have let $e^{\mathbf{k}^2\langle\hat{\mathbf{u}}_{oi}\hat{\mathbf{u}}_{oj}\rangle_T} = 1 + [e^{\mathbf{k}^2\langle\hat{\mathbf{u}}_{oi}\hat{\mathbf{u}}_{oj}\rangle_T} - 1]$ and $\mathbf{k}^2\langle\hat{\mathbf{u}}_{oi}^2\rangle = \mathbf{k}^2\langle\hat{\mathbf{u}}_{oj}^2\rangle = 2\mathbf{W}$

The first term in the brackets represents a complete sum over all the equilibrium lattice positions of the atoms. It is this term which gives rise to delta functions in reciprocal space, i.e. Bragg scattering. This is modulated by the $e^{-2\mathbf{W}}$ term which reduces the intensity of the scattered radiation as the atomic vibrations increase. The second term in the brackets behaves very differently and has an intensity that increases with atomic vibration, the structure factor here is given by the correlations between atom displacements given by the term $\langle\hat{\mathbf{u}}_{oi}\hat{\mathbf{u}}_{oj}\rangle_T$. This term gives rise to thermal diffuse scattering (TDS). Finally, making the approximation that we have no correlations between atoms,

$$\langle\hat{\mathbf{u}}_{oi}\hat{\mathbf{u}}_{oj}\rangle_T = 0 \qquad i \neq j\,, \tag{D.17}$$

$$S(\mathbf{k}) = \frac{S_t(\mathbf{k})e^{-2\mathbf{W}}}{N}\left(\sum_i^N\sum_j^N e^{-i\mathbf{k}.[\mathbf{R}_i-\mathbf{R}_j]} + N[e^{2W}-1]\right)\,, \tag{D.18}$$

$$S(\mathbf{k}) = S_t(\mathbf{k})e^{-2\mathbf{W}}\left(b(\mathbf{k}) + [e^{2W}-1]\right)\,, \tag{D.19}$$

where letting $b(\mathbf{k}) = \frac{1}{N}\sum_{i=1}^N\sum_{j=1}^N e^{-i\mathbf{k}.[\mathbf{R}_i-\mathbf{R}_j]}$, gives,

$$S(\mathbf{k}) = S_t(\mathbf{k})\left(1 - e^{-2W} + e^{-2W}\,b(\mathbf{k})\right)\,. \tag{D.20}$$

Appendix E

Graphite EOS

It is necessary to calculate the EOS for graphite to solve the coupled equations of the TTM, that is the specific heat for both the electron and ion subsystems. In the case of the ionic subsystem two different models were used: PROPACEOS 4.2 [124] and *ab-initio* DFT for the electrons coupled to classical molecular dynamics for the ions (DFT-MD) [208]. DFT calculations for the electrons were carried out using the ABINIT software package [74]. In the simulations the structure of solid graphite was taken to be hexagonal with Pearson symbol hP4, space group P63/mmc, using 194 lattice points with lattice constants $a = 2.456$ Å and $c = 6.696$ Å. An electron-ion pseudopotential that explicitly treated 4 valence electrons using the Perdew-Burke-Ernzerhof GGA functional was used. The number of k-points treated per dimension was 35 and the plane wave cut-off was 1088 eV ensuring convergence in the electronic DOS. Temperature results from these different calculations are reported in Fig. E.1.

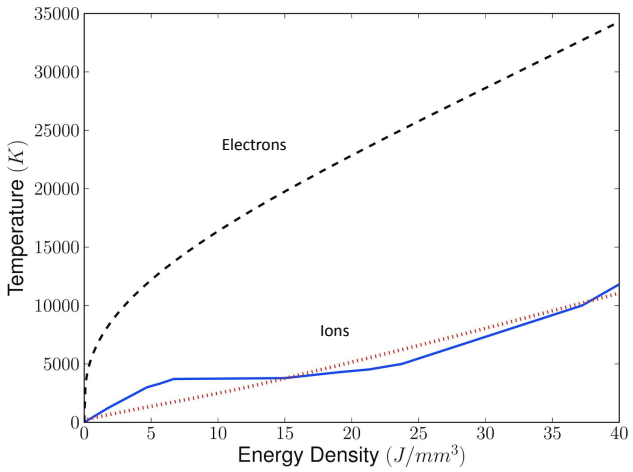

Figure E.1: Black dashed line: electron temperature plotted against internal energy; Red dotted line: ion temperature plotted against internal energy extracted from PROPACEOS 4.2; Blue solid line: ion temperature plotted against internal energy extracted from DFTMD. The plateau in the temperature, seen when the deposited energy ranges from from 7 to 22 J/mm^3, is associated to latent heat (not included in PROPACEOS).

Appendix F

Energy Transfer to Electrons and Ions by a Fast Particle

This appendix outlines a simple derivation found in many classical electromagnetism textbooks [102]. Consider a proton of mass M_p and energy $E_p = M_p\gamma c^2$ incident upon a stationary target of mass M_T. Here, $\gamma = 1/(1 - v_p^2/c^2)^{\frac{1}{2}}$, c is the speed of light in a vacuum and v_p the velocity of the incoming proton. The approximation of a stationary target and an un-deflected proton (impulse approximation) is valid when the velocity of the incoming beam is very much greater than the thermal velocity of the target particle.

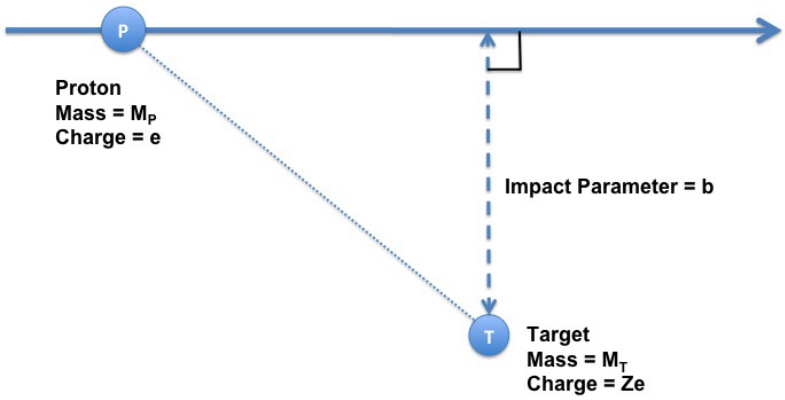

Figure F.1: Diagram showing typical Coulomb scattering event

The magnitude of the perpendicular and parallel components of the electric field incident on the target particle are given by,

$$E_\perp(b) = \frac{\gamma e b}{(b^2 + \gamma^2 v_p^2 t^2)^{\frac{3}{2}}} \tag{F.1}$$

$$E_{\parallel}(b) = -\frac{\gamma e v_p t}{(b^2 + \gamma^2 v_p^2 t^2)^{\frac{3}{2}}} \tag{F.2}$$

where b is the impact parameter and represents the point of closest approach to the target. In this formulation $t = 0$ is the time when the proton is positioned at b. The integral over all time of the parallel electric field (F.2) is zero. The integral of the perpendicular magnetic field (F.1) is non-zero and related to the momentum transfer through,

$$\begin{aligned} \Delta p &= \int_{-\infty}^{\infty} dt(ZeE_{\perp}) = \int_{-\infty}^{\infty} dt \frac{Ze\gamma eb}{(b^2 + \gamma^2 v^2 t^2)^{\frac{3}{2}}} \\ &= \frac{Ze^2 b}{v} \int_{-\infty}^{\infty} \frac{dx}{(b^2 + x^2)^{\frac{3}{2}}} = \frac{Ze^2}{bv} \int_{-\infty}^{\infty} \frac{du}{(1 + u^2)^{\frac{3}{2}}} = \frac{2Ze^2}{bv} \end{aligned} \tag{F.3}$$

where Ze is the charge of the target particle. Making one final approximation that the energy transfer $\Delta p << mc$, i.e. non-relativistic, we can approximate the energy transfer to the target as,

$$\Delta E = \frac{\Delta p^2}{2M_T} = \frac{2Z^2 e^4}{M_T b^2 v^2} \propto \frac{Z^2}{M_T} \tag{F.4}$$

Table F.1: Energy transfer to electrons and ions in a plasma by a hot ion

Effect	Ion	Electron
Charge	z^2	1
Mass	$1/1836z$	1
Density	1	z
Total	$z/1836$	z

Looking now at an ion traversing through a macroscopic sample we can compare energy lost to the electrons and ions. Table F shows the relative energy deposited in each of the ion species taking into account density, charge and mass. This shows that the energy transferred to the ions by the fast protons is 1836 times less than the energy transferred to the electrons.

Appendix G

Additional Details on Fast Electron Transport

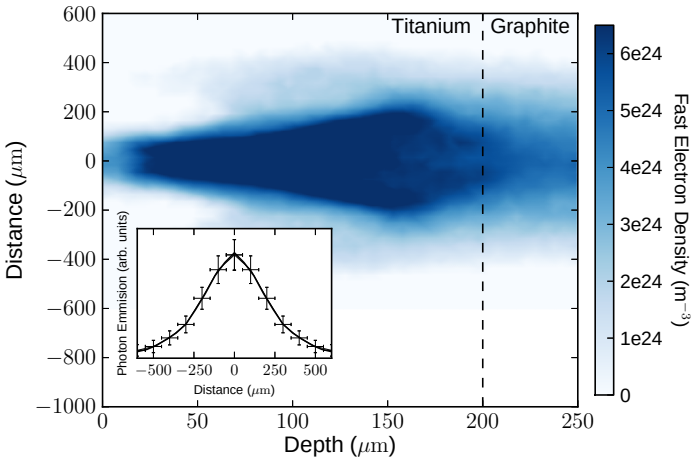

Figure G.1: Simulation results showing the fast electrons, produced from the laser interaction of the target, heating the graphite sample. These results are produced from the fast electron transport code ZEPHYROS. The fast electron density (units $1/\mathrm{m}^3$) is shown at time=0.8 ps. The insert shows the Ti-K$_\alpha$ emission from the simulation and the experimental measurement using an absolutely calibrated imaging spectrometer.

This appendix will discuss in greater detail the effects of magnetic focusing, instability formation and the time-scale of the heating mechanism. This is achieved by inspecting the results for fast electron density, fast electron current, induced electric and magnetic fields, heating and resistivity plots from the transport code ZEPHYROS. Each of the plots presented here represents an xy slice through the target. The x-direction corresponds to the depth within the sample (fast electron propagation di-

rection), while the y-direction (along page) and z-direction (out of page) correspond to the distance along the sample surface.

Fig. G.1 is reproduced from section 3.4.2 for clarity and shows the fast electron density at t=0.8 s produced from the fast electron transport code ZEPHYROS. The inset shows the resultant line emission at the characteristic energy of 4.51 keV from the Ti substrate. As discussed earlier this resulting line emission was used to calibrate the fast electron beam properties including energy, spectral temperature and divergence angle.

G.1 Magnetic Focusing

By fitting the simulated line emission to the one measured experimentally the divergence angle was found to be ∼80° in each of the shots analysed. However, analysis of the fast electron density divergence from Fig. G.1 shows that the divergence after propagating through the sample a distance of 50 μm has been reduced to ∼70°. This is the effect of magnetic focusing in the target.

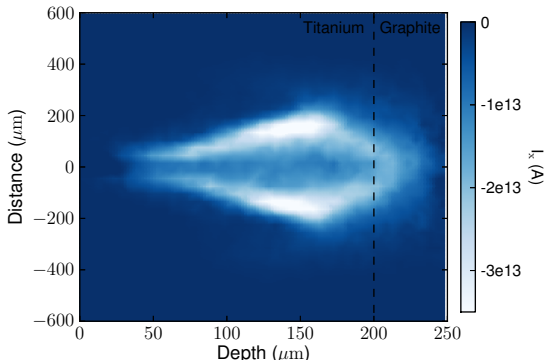

Figure G.2: Simulation results from ZEPHYROS electron transport code showing the resistive return current corresponding to the fast electron density in Fig. G.1 at 0.8 ps after the laser is incident on the sample.

The high currents within the sample induce strong electric and magnetic fields shown in Figs. G.6 and G.7 respectively. These fields can cause the initially divergent fast electron beam to focus. Evidence of this can be seen in the final panel of Fig. G.6 where strong magnetic fields confine the fast electrons.

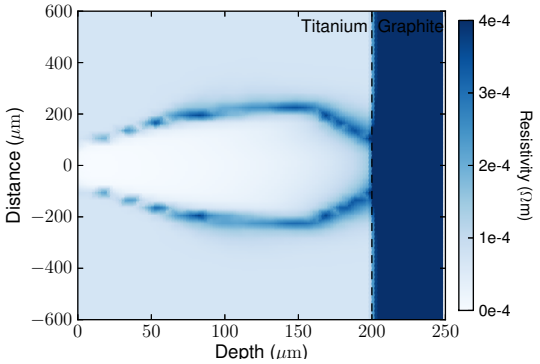

Figure G.3: Simulation results from ZEPHYROS electron transport code showing the resistivity corresponding to the fast electron density in Fig. G.1 at 0.8 ps after the laser is incident on the sample.

G.2 Instability Formation

The fast electron current creates a strong electric field in the sample which produces a cold return current in the opposite direction, see Fig. G.2. This cold return current experiences greater resistivity and hence through Joule heating deposits energy into the electron subsystem. Fig. G.3 shows the resistivity at 0.8 ps calculated using the reduced Lee-Moore model, while Fig. G.4 shows the resultant electron temperature from this heating. On this time-scale any energy loss to the ions can be considered negligible.

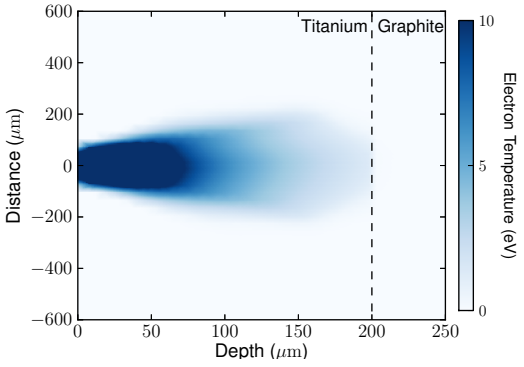

Figure G.4: Simulation results from ZEPHYROS electron transport code showing the electron temperature corresponding to the fast electron density in Fig. G.1 at 0.8 ps after the laser is incident on the sample.

The variation of the resistivity with temperature leads to the possibility that struc-

tures or instabilities can form within the sample. The properties of these structures vary depending on how the resistivity varies with temperature. A detailed description can be found in [153, 154]. In the Lee-More model resistivity increases with temperature up to around 2 eV and decreases above this value. No evidence of filamentation instabilities are seen in the simulations. The formation of so called *striations*, larger scale structures may be visible towards the end of the Ti substrate. However, once the electron beam passes into the graphite is appears that no remnants of this structure remain. The experimental data corroborates this as there is no large scale structure in either the ion temperature measurements or the spatially resolved X-ray emission (inset of Fig. G.1).

G.3 Time-scale of Heating by Fast Electrons

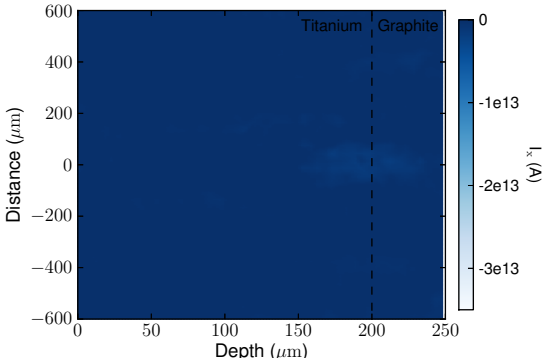

Figure G.5: Simulation results from ZEPHYROS electron transport code showing the current corresponding to the fast electron density 2.0 ps after the laser is incident on the sample.

Finally, when heating by a short-pulse beam propagating near the axis it is possible for currents to remain in the system long after the laser beam has been switched off. A current loop can be formed with in the sample with a typical decay time of the order of the resistive skin time, $\mu_0 a^2/\eta$. A calculation of the skin time, with a scale length of a =50 μm (graphite depth) and a resistivity of the order of η =1e-3 Ohm-m for cold graphite (perpendicular to the basal plane), leads to a skin-time of the order of 1 ps. As we expect currents formed in the sample to decay on this time scale and the time scale of the experiment is of the order of 100 ps we can consider the heating mechanism to be instantaneous in the graphite. Additionally, by looking at

the evolution of the currents in the ZEPHYROS simulation we find that within 2 ps of the laser pulse the electrons have a negligible effect on the heating, see Fig G.5.

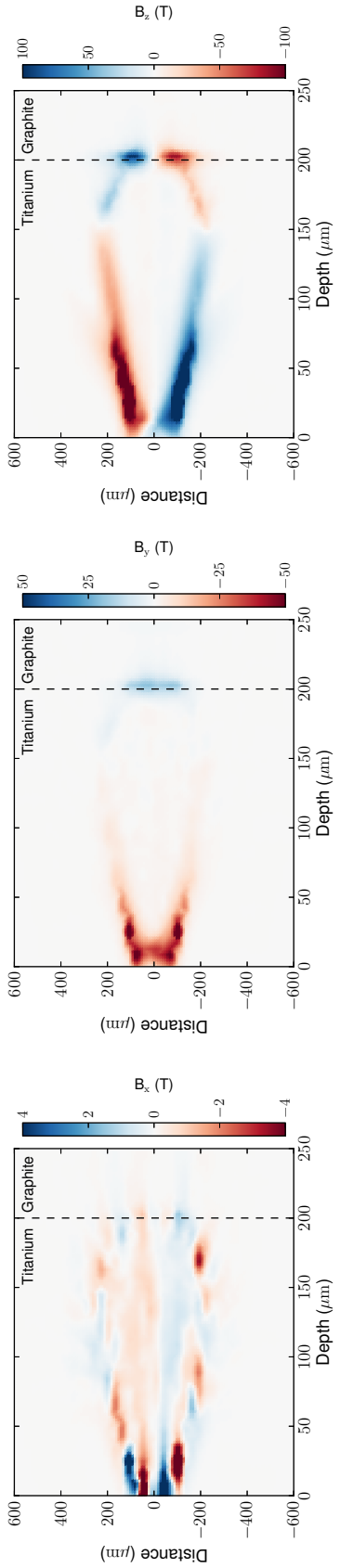

Figure G.6: Simulation results from ZEPHYROS electron transport code showing the magnetic field strength corresponding to the fast electron density in Fig. G.1 at 0.8 ps after the laser is incident on the sample.

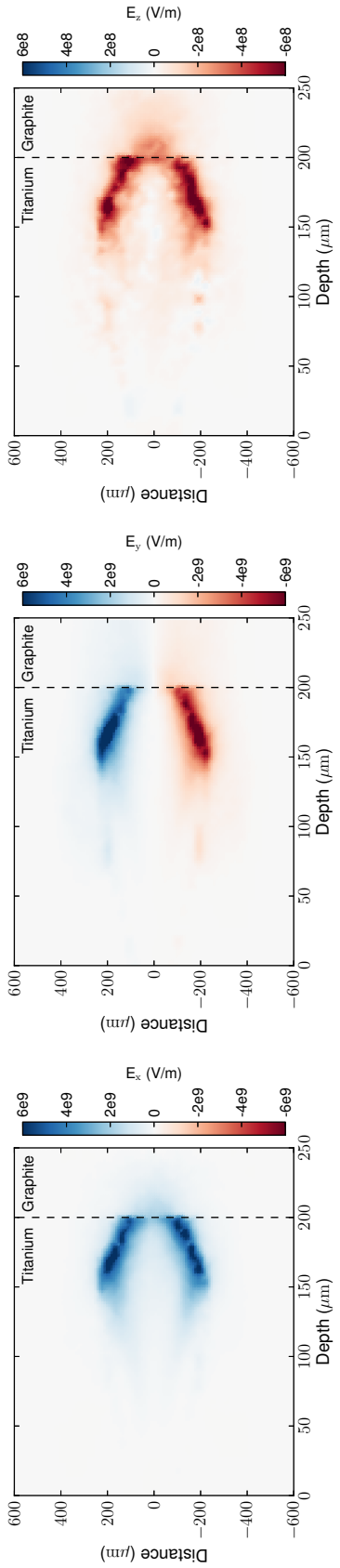

Figure G.7: Simulation results from ZEPHYROS electron transport code showing the electric field strength corresponding to the fast electron density in Fig. G.1 at 0.8 ps after the laser is incident on the sample.

Appendix H

Simple Proof of Hohenberg and Kohn Theorems

The first Hohenberg and Kohn theorem states that the external potential of a system, $v(\mathbf{r})$ is determined entirely by the electron density $\rho(\mathbf{r})$. The proof of this theorem is exquisitely simple. First we note that simple integration of the electron density provides N, the number of electrons in the system. Then we consider two systems with differing potentials, v_1 and v_2 which have the same ground state density, ρ. We would then have two Hamiltonians H_1 and H_2 with two differing ground state wave functions ϕ_1 and ϕ_2.

Since $E_0 = \min_{\phi} E[\phi]$ it follows that $E[\phi] \geq E_0$. Inserting the wave functions ϕ_2 into the Hamiltonian for system 1 the inequality can be written as,

$$E_{01} < \langle \phi_2 | \hat{H}_1 | \phi_2 \rangle = \langle \phi_2 | \hat{H}_2 | \phi_2 \rangle + \langle \phi_2 | \hat{H}_1 - \hat{H}_2 | \phi_2 \rangle \,, \tag{H.1}$$

$$= E_{02} + \int \rho(\mathbf{r})[v_1(\mathbf{r}) - v_2(\mathbf{r})] d\mathbf{r} \,. \tag{H.2}$$

Similarly inserting the wave functions ϕ_1 into the Hamiltonian for system 2 the inequality can be written as,

$$E_{02} < \langle \phi_1 | \hat{H}_2 | \phi_1 \rangle = \langle \phi_1 | \hat{H}_1 | \phi_1 \rangle + \langle \phi_1 | \hat{H}_2 - \hat{H}_1 | \phi_1 \rangle \,, \tag{H.3}$$

$$= E_{01} - \int \rho(\mathbf{r})[v_1(\mathbf{r}) - v_2(\mathbf{r})] d\mathbf{r} \,. \tag{H.4}$$

Adding equations H.2 and H.4 gives $E_{01} + E_{02} < E_{02} + E_{01}$ which is a contradiction. Thus, there cannot be two different potentials that give the same ground state electronic density [148].

Appendix I

Extracting Transport Coefficients from Molecular Dynamics

In section 5.6 a generalised hydrodynamic model of the DSF is used to fit the X-ray scattering spectrum taken from a dense aluminium plasma. Thermodynamic and transport coefficients are then extracted through fitting the scattering spectrum.

In section 2.1.3 on correlation functions it is demonstrated that the internal energy of a system and its pressure can both be obtained from the RDF of a MD simulation. In fact, many more thermodynamic and transport coefficients can be extracted from MD in a similar way. It is therefore of interest to compare the results from the two methods as a study of the applicability of MD to describe these dense plasmas. Specifically, for a Yukawa plasma, these coefficients have been parametrised in various studies negating the need to actually run the numerical simulations. These parametrisations allow thermodynamic and transport coefficients to be calculated analytically, albeit from the fit to numerical data.

For the aluminium plasma studied in chapter 5.6 (T=5 eV, ρ=7 g/cm^3) we obtain an ion-ion coupling parameter of $\Gamma_{ii} \sim 5.6$ and a screening length of $\kappa = 1.75 - 2.14$ Å^{-1}. This gives a value for the dimensionless screening length of $\kappa^* = \kappa a \sim 2 - 2.3$ depending on the choice of model, either the two temperature mixing [67] or the Thomas-Fermi [174]. Other parameters necessary to calculate the following transport and thermodynamic coefficients are the ion density, $n_i = 1.5 \times 10^{29}$ /m^3, the plasma frequency, ω_p =0.15 fs^{-1}, and, the WignerSeitz radius $a = 1.15$ Å. An ionisation of Z=1.5 was used throughout the calculation.

I.1 Sound Speed and Heat Capacity Ratio

Hamaguchi *et al.* (1996, 1997) [83, 84] demonstrated that for a Yukawa plasma the excess internal energy extracted from a MD simulation can be fitted to,

$$u(\kappa,\Gamma) = a(\kappa)\Gamma + b(\kappa)\Gamma^s + c(\kappa) + d(\kappa)\Gamma^{-s}\,, \tag{I.1}$$

where for a screening length of $\kappa^* = 2.0$ the parameters are,

$$\begin{aligned} a &= -1.270571 \\ b &= 0.442193 \\ c &= -0.382900 \\ d &= 0.100506 \end{aligned} \tag{I.2}$$

The excess energy per particle for this system is $u/\Gamma_{ii} = -1.188$.

The total internal energy of the system is given by,

$$U = U_0 + Nk_BTu(\kappa^*, \Gamma_{ii})\,, \tag{I.3}$$

where $U_0 = 3/2Nk_BT$ is the internal energy of the ideal gas. From this expression it is clear that $u(\kappa,\Gamma)$ is a dimensionless variable.

The following derivations are based on the work in appendix D of Ref. [133]. An expression for the pressure can be related to the internal energy through [21],

$$\frac{P}{P_0} = 1 + \frac{1}{2}\frac{U - U_0}{U_0}\,, \tag{I.4}$$

where $P_0 = nk_BT$ is the pressure of the idea gas. Then taking the standard thermodynamic expressions for the heat capacity at constant volume,

$$C_v = \left(\frac{\partial U}{\partial T}\right)_V\,, \tag{I.5}$$

the heat capacity at constant pressure,

$$C_P = \left(\frac{\partial U}{\partial T}\right)_P\,, \tag{I.6}$$

and the isothermal compressibility,

$$\chi_T = -\frac{1}{V}\left(\frac{\partial V}{\partial P}\right)_T\,, \tag{I.7}$$

can now all be derived in terms of the excess internal energy, u.

By taking the partial derivative of Eq. I.3 with respect to the temperature T an expression for the heat capacity at constant volume is found to be,

$$\begin{aligned}\frac{C_V}{Nk_B} &= \frac{3}{2} + \left(\frac{\partial}{\partial T}[Tu(\Gamma_{ii}, \kappa^*)]\right)_V \\ &= \frac{3}{2} + u(\Gamma_{ii}, \kappa^*) + T\left(\frac{\partial}{\partial T}u(\Gamma_{ii}, \kappa^*)\right)\end{aligned} \tag{I.8}$$

To calculate this function Mithen (2013) [133] notes that κ^* is just a number that governs the interaction potential and does not depend on temperature in the model Yukawa system. The partial derivative with respect to temperature can then be altered through the use of the chain rule to,

$$\frac{\partial}{\partial V} = \frac{\partial \Gamma_{ii}}{\partial V}\frac{\partial}{\partial \Gamma_{ii}} == \frac{1}{3}\frac{\Gamma_{ii}}{V}\frac{\partial}{\partial V}\,. \tag{I.9}$$

which gives,

$$\frac{C_V}{Nk_B} = \frac{3}{2} + u(\Gamma_{ii}, \kappa^*) - \Gamma\frac{\partial}{\partial \Gamma_{ii}}u(\Gamma_{ii}, \kappa^*)\,. \tag{I.10}$$

Given the parameterisation for u by the Hamaguchi EOS the heat capacity at constant volume can be numerically calculated from the above expression. Likewise appendix D of Ref. [133] derives similar expressions for the isothermal compressibility,

$$\frac{\chi_T^0}{\chi_T} = 1 + \frac{1}{3}u(\Gamma_{ii}, \kappa^*) + \frac{1}{9}\Gamma_{ii}\frac{\partial}{\partial \Gamma_{ii}}u(\Gamma_{ii}, \kappa^*)\,, \tag{I.11}$$

and the heat capacity at constant pressure,

$$\frac{C_P}{Nk_B} = \frac{C_V}{Nk_B} + \frac{1}{9}\left(\frac{C_V}{Nk_B}\right)^2\frac{\chi_T}{\chi_T^0}\,. \tag{I.12}$$

Finally an expression for the heat capacity ratio is obtained by,

$$\gamma = \frac{C_P}{C_V}\,, \tag{I.13}$$

and the sound speed through,

$$c_s = \sqrt{\frac{\gamma k_B T}{m}\frac{\chi_T^0}{\chi_T}}\,. \tag{I.14}$$

It must be noted that these derived equations are known to give a negative compressibility for the Yukawa system. As discussed in the main text this is due to the

Yukawa potential including the screening effects of the electrons but the simulation containing only ions. Hence, to obtain a physically accurate result the effect of the neutralising electron background must be included. Salin [172] (2007) notes that the effect of the background can be included by adding a term to the compressibility,

$$\frac{\chi_T^0}{\chi_T^{WB}} = \frac{\chi_T^0}{\chi_T} + \frac{4\pi\beta}{\kappa^{*2}}\rho\,, \tag{I.15}$$

which in the reduced units preferred by Mithen gives,

$$\frac{\chi_T^0}{\chi_T^{WB}} = \frac{\chi_T^0}{\chi_T} + \frac{3\Gamma_{ii}}{\kappa^{*2}}\,. \tag{I.16}$$

For the system studied here the heat capacity ratio is determined to be γ=1.08 and the sound speed to be c_s=6.54 km/s. Finally, it should be noted that the recovered sound speed disagrees with the sound speed obtained directly from the MD simulations performed by Mithen and given in Ref. [133]. For the case of $\Gamma_{ii} = 5$ and $\kappa^* = 2$ the sound speed obtained directly from MD is given as c_s=9.67 km/s. Since the cause of this discrepancy is currently unknown, both the fit to EOS models and the direct calculation are given in the main text. Preliminary work suggests that the paramaterisation of internal energy by Hamaguchi is the cause of the discrepency. The calculation of the heat capacity ratio shows no apparent discrepancy between the EOS fit and the MD [134].

I.2 Shear Viscosity

The transport coefficients have been directly parameterised and do not depend on the internal energy. The parameterisation of the terms are often given in terms of the dimensionless variable T_* which is the ratio of temperature T to the melt temperature T_m, or equivalently $\Gamma_{ii}^* = \Gamma_{ii\ m}/\Gamma_{ii}$. For a dimensionless screening parameter $\kappa^* = 2$ we have that $T_* = 78.6$ [170].

The shear viscosity term is calculated from parametrisations given by Saigo and Hamaguchi (2002) [170]. They define the reduced shear viscosity $\hat{\eta}$=$\eta/(\sqrt{3}mn_i\omega_E a^2)$ where the Einstein frequency, a characteristic frequency of the system, is given by 0.5315=$\sqrt{3}\omega_E/\omega_p$ for $\kappa^* = 2$. The parametrisation of the shear viscosity is then given by,

$$\hat{\eta} = aT^* + b/T^* + c \tag{I.17}$$

where for $\kappa^* = 2$,

$$\begin{aligned} a &= 0.005091 \\ b &= 0.393 \\ c &= 0.000596 \end{aligned} \tag{I.18}$$

giving $\hat{\eta}$=0.4 and η =2.97 mPa s.

Sanbonmatsu and Murillo (2007) [175] who discuss in detail the minimum bound on the shear viscosity give the value at $\Gamma_{ii} = 5$ and $\kappa^* \sim 2$ as η^*=0.0829, where the reduced shear viscosity is now $\eta^* = \eta/(mn_i\omega_p a^2)$, giving η =1.16 mPa s.

I.3 Thermal Diffusivity

The thermal diffusivity term can be directly calculated from the parametrisation of MD data provided by Ohta and Hamaguchi (2000) [146]. They propose the following equation,

$$D_T^* = \alpha(T^* - 1)^\beta + \gamma\,, \tag{I.19}$$

which for a dimensionless screening parameter $\kappa^* = 2$ the coefficients are given by,

$$\begin{aligned} \alpha &= 0.0131 \\ \beta &= 1.04 \\ \gamma &= 0.00385 \end{aligned} \tag{I.20}$$

which gives a dimensionless thermal diffusivity of $D_T^* = 1.21$ equating to $D_T = \omega_E a^2 D^* = 0.7 \times 10^{-6}$ m^2/s.

A second parameterisation of the thermal diffusivity is given by Donkó and Hartmann (2004) [50] where D_T is converted from values for the thermal conductivity λ through $D_T = \lambda/c_p$, in which c_p is the volumetric heat capacity at constant pressure calculated above in section I.1. They parametrise the thermal diffusivity by,

$$\lambda^* = 0.018T^* + 1.05/T^* + 0.115\,, \tag{I.21}$$

which for this system gives a dimensionless thermal conductivity of λ^* =1.79. Again, this can be related to the thermal conductivity through $\lambda = \lambda^* n k_B \sqrt{3}\omega_E a^2$ giving a value of λ =4.07 W/(K m). Converting this into a thermal diffusivity gives $D_T = 1.01 \times 10^{-6}$ m^2/s.

Appendix J

List of Publications

Publications in peer reviewed journals,

- **T. G. White**, N. J. Hartley, B. Borm, B. J. B. Crowley, J. W. O. Harris, D. C. Hochhaus, T. Kaempfer, K. Li, P. Neumayer, L.K. Pattison, F. Pfeifer, S. Richardson, A. P. L. Robinson, I. Uschmann, and G. Gregori, *Electron-ion equilibration in ultrafast heated graphite*, Physical Review Letters, *112*, 145005 (2014)

- **T. G. White**, P. Mabey, D. O. Gericke, N. J. Hartley, H. W. Doyle, D. McGonegle, D. Rackstraw, A. Higginbotham and G. Gregori, *Electron-phonon equilibration in laser heated gold films*, Physical Review B, *123*, 12345 (2014)

- **T. G. White**, S. Richardson, B. J. B. Crowley, L. K. Pattison, J. W. O. Harris, and G. Gregori, *Orbital-free density-functional theory simulations of the dynamic structure factor of warm dense aluminum*, Physical Review Letters, *111*, 175002 (2013)

- **T. G. White**, J. Vorberger, C. R. D. Brown, B. J. B. Crowley, P. Davis, S. H. Glenzer, J. W. O. Harris, D. C. Hochhaus, S. Le Pape, T. Ma, C. D. Murphy, P. Neumayer, L. K. Pattison, S. Richardson, D. O. Gericke and G. Gregori, *Observation of inhibited electron-ion coupling in strongly heated graphite*, Scientific Reports, *2*, 889 (2012)

- N. J. Hartley, P. Belancourt, D. Gericke, D Khaghani, P. Neumayer, L. Peters, **T. G. White**, and G. Gregori, *Electron-Ion Equilibration in Warm Dense Tantalum*, Submitted to High Energy Density Physics (2014)

- U. Zastrau, P. Sperling, A. Becker, T. Bornath, R. Bredow, T. Döppner, S. Dziarzhytski, T. Fennel, L. B. Fletcher, E. Förster, C. Fortmann, S. H. Glenzer, S. Göde, G. Gregori, M. Harmand, V. Hilbert, B. Holst, T. Laarmann, H. J. Lee, T. Ma, J. P. Mithen, R. Mitzner, C. D. Murphy, M. Nakatsutsumi, P. Neumayer, A. Przystawik, S. Roling, M. Schulz, B. Siemer, S. Skruszewicz, J. Tiggesbümker, S. Toleikis,4 T. Tschentscher, **T. G. White**, M. Wöstmann, H. Zacharias and R. Redmer, *Equilibration dynamics and conductivity of warm dense hydrogen*, Physical Review E *90*, 013104 (2014)

- C. R. D. Brown, D. O. Gericke, M. Cammarata, B. I. Cho, T. Döppner, K. Engelhorn, E. Förster, C. Fortmann, D. Fritz, E. Galtier, S. H. Glenzer, M. Harmand, P.

Heimann, N. L. Kugland, D. Q. Lamb, H. J. Lee, R. W. Lee, H. Lemke, M. Makita, A. Moinard, C. D. Murphy, B. Nagler, P. Neumayer, K-U. Plagemann, R. Redmer, D. Riley, F. B. Rosmej, P. Sperling, S. Toleikis, S. M. Vinko, J. Vorberger, S. White, **T. G. White**, K. Wunsch, U. Zastrau, D. Zhu, T. Tschentscher, G. Gregori, *Evidence for a glassy state in strongly driven carbon*, Scientific Reports, *4*, 5214 (2014)

- T. Ma, D. Chapman, T Dppner, R. W. Falcone, L. Fletcher, C. Fortmann, E. Galtier, D. O. Gericke, G. Gregori, J. Hastings, O. L. Landen, S. Le Pape, H. J. Lee, B. Nagler, P. Neumayer, A. Pak, D. Turnbull, J. Vorberger, **T. G. White**, K. Wünsch, U. Zastrau, and S. H. Glenzer, *Observations of strong ion-ion correlations in dense plasmas*, Physics of Plasmas, *21 (5)*, 056302 (2014)

- L. B. Fletcher, H. J. Lee, B. Barbrel, M. Gauthier, E. Galtier, B. Nagler, T. Döppner, S. LePape, T. Ma, A. Pak, D. Turnbull, **T. G. White**, G. Gregori, M. Wei, R. W. Falcone, P. Heimann, U. Zastrau, J. B. Hastings, S. H. Glenzer, *Exploring Mbar shock conditions and isochorically heated aluminum at the Matter in Extreme Conditions end station of the Linac Coherent Light Source*, Review of Scientific Instruments, *85 (11)*, 11E702 (2014)

- U. Zastrau, P. Sperling, M. Harmand, A. Becker, T. Bornath, R. Bredow, S. Dziarzhytski, T. Fennel, L. B. Fletcher, E. Förster, S. Göde, G. Gregori, V. Hilbert, D. Hochhaus, B. Holst, T. Laarmann, H. J. Lee, T. Ma, J. P. Mithen, R. Mitzner, C. D. Murphy, M. Nakatsutsumi, P. Neumayer, A. Przystawik, S. Roling, M. Schulz, B. Siemer, S. Skruszewicz, J. Tiggesbümker, S. Toleikis, T. Tschentscher, **T. G. White**, M. Wöstmann, H. Zacharias, T. Döppner, S. H. Glenzer and R. Redmer, *Resolving ultrafast heating of dense cryogenic hydrogen*, Physical Review Letters *112*, 105002 (2014)

- S. White, G. Nersisyan, B. Kettle, TWJ Dzelzainis, K McKeever, CLS Lewis, A Otten, K Siegenthaler, D Kraus, M Roth, **T. G. White**, G Gregori, DO Gericke, R Baggott, DA Chapman, K Wnsch, J Vorberger, D Riley, *X-ray scattering from warm dense iron*, High Energy Density Physics, *9 (3)*, 573-577 (2013)

- M. Harmand, C. D. Murphy, C. R. D. Brown, M. Cammarata, T. Doppner, S. Dsterer, D. Fritz, E. Forster, E. Galtier, J. Gaudin, S. H. Glenzer, S. Gode, G. Gregori, V. Hilbert, D. Hochhaus, T. Laarmann, H. J. Lee, H. Lemke, K-H. Meiwes-Broer, A. Moinard, P. Neumayer, A. Przystawik, H. Redlin, M. Schulz, S. Skruszewicz, F. Tavella, T. Tschentscher, **T. G. White**, U. Zastrau, S. Toleikis, *Plasma switch as a temporal overlap tool for pump-probe experiments at FEL facilities*, Journal of Instrumentation, *7 (08)*, P08007 (2012)

- U. Zastrau, V. Hilbert, C. Brown, T. Döppner, S Dziarzhytski, E Frster, SH Glenzer, S Göde, G Gregori, M Harmand, D Hochhaus, T Laarmann, HJ Lee, K-H Meiwes-Broer, P Neumayer, A Przystawik, P Radcliffe, M Schulz, S Skruszewicz, F Tavella, J Tiggesbumker, S Toleikis, **T. G. White**, *In-situ determination of dispersion and resolving power in simultaneous multiple-angle XUV spectroscopy*, Journal of Instrumentation, *6* P10001 (2011)

Publications in preperation or submitted to peer review journals,

- L. B. Fletcher, H. J. Lee , T. Döppner , C. Fortmann , S. LePape , T. Ma , A. Pak , D. Turnbull , D. A. Chapman , D. O. Gericke , J. Vorberger, **T. G. White** , G. Gregori , M. Wei , E. Galtier , U. Zastrau , B. Nagler , P. Heimann , J. Welch , B. Barbrel , R. W. Falcone , J. B. Hastings and S. H. Glenzer, *Exploring the high-pressure properties of aluminum with an ultra-bright seeded x-ray laser*, Submitted to Nature Materials (2014)

- G. Monaco, **T. G. White**, L. B. Fletcher, H. J. Lee , T. Döppner , C. Fortmann , S. LePape , T. Ma , A. Pak , D. Turnbull , D. A. Chapman , D. O. Gericke , J. Vorberger, G. Gregori , M. Wei , E. Galtier , U. Zastrau , B. Nagler , P. Heimann , J. Welch , B. Barbrel , R. W. Falcone , J. B. Hastings and S. H. Glenzer, Low frequency structural dynamics of warm dense aluminium, In Preperation (2014)

Bibliography

[1] M. Agranat, S. Anisimov, and B. Makshantsev. The anomalous thermal radiation of metals produced by ultrashort laser pulses. *Applied Physics B* **55**:451–461 (1992).

[2] S. Glenzer et al. Melting of Aluminium at high-pressure *submitted to Nature Physics* (2014).

[3] B. Alder and T. Wainwright. Phase transition for a hard sphere system. *The Journal of Chemical Physics* **27**:1208–1209 (1957).

[4] B. J. Alder and T. Wainwright. Studies in molecular dynamics. i. general method. *The Journal of Chemical Physics* **31**:459–466 (1959).

[5] P. Allen and D. Tildesley. *Computer Simulation of Liquids*. Oxford Science Publ (Clarendon Press, 1989).

[6] P. B. Allen. Theory of thermal relaxation of electrons in metals. *Physical Review Letters* **59**:1460 (1987).

[7] J. Als-Nielsen and D. McMorrow. *Elements of Modern X-ray Physics* (Wiley, 2011).

[8] B. L. Altshuler, A. G. Aronov, and P. Lee. Interaction effects in disordered fermi systems in two dimensions. *Physical Review Letters* **44**:1288 (1980).

[9] L. V. Al'tshuler. *Zhurnal Eksperim i. Teoretich Fiziki* **13**:11–12 (1943).

[10] J. Amann, W. Berg, V. Blank, F. J. Decker, Y. Ding, P. Emma, Y. Feng, J. Frisch, D. Fritz, J. Hastings, *et al.* Demonstration of self-seeding in a hard-X-ray free-electron laser. *Nature Photonics* **6**:693–698 (2012).

[11] S. Anisimov, B. Kapeliovich, and T. Perelman. Electron emission from metal surfaces exposed to ultrashort laser pulses. *Zhurnal Eksperimentalnoi i Teoreticheskoi Fiziki* **66**:375–7 (1974).

[12] J. Anta, B. Jesson, and P. Madden. Ion-electron correlations in liquid metals from orbital-free ab initio molecular dynamics. *Physical Review B* **58**:6124 (1998).

[13] N. Ashcroft and N. Mermin. *Solid State Physics* (Harcourt Asia, 2001).

[14] S. Atzeni and J. Meyer-ter Vehn. *The Physics of Inertial Fusion : BeamPlasma Interaction, Hydrodynamics, Hot Dense Matter: BeamPlasma Interaction, Hydrodynamics, Hot Dense Matter*. International Series of Monographs on Physics (Clarendon Press, 2004).

[15] D. Baiko, A. Kaminker, A. Potekhin, and D. Yakovlev. Ion structure factors and electron transport in dense coulomb plasmas. *Physical Review Letters* **81**:5556 (1998).

[16] J. Bailey, G. Rochau, R. Mancini, C. Iglesias, J. MacFarlane, I. Golovkin, C. Blancard, P. Cosse, and G. Faussurier. Experimental investigation of opacity models for stellar interior, inertial fusion, and high energy density plasmas. *Physics of Plasmas* **16**:058101 (2009).

[17] A. Baldereschi. Mean-value point in the brillouin zone. *Physical Review B* **7**:5212 (1973).

[18] J. Bardeen, L. N. Cooper, and J. R. Schrieffer. Theory of superconductivity. *Physical Review* **108**:1175 (1957).

[19] J. Bardeen and D. Pines. Electron-phonon interaction in metals. *Physical Review* **99**:1140 (1955).

[20] D. Bäuerle. *Laser Processing and Chemistry* (Springer, 2011).

[21] M. Baus and J.-P. Hansen. Statistical mechanics of simple coulomb systems. *Physics Reports* **59**:1 – 94 (1980).

[22] G. Baym. *Lectures on Quantum Mechanics*. Advanced book program (Addison-Wesley, 1990).

[23] M. Berger, J. Coursey, M. Zucker, and J. Chang. Estar, pstar, and astar: computer programs for calculating stopping-power and range tables for electrons, protons, and helium ions (version 1.2.3). *Available: http://physics.nist.gov/Star* (2013).

[24] P. E. Blöchl. Projector augmented-wave method. *Physical Review B* **50**:17953 (1994).

[25] S. E. Boulfelfel, A. R. Oganov, and S. Leoni. Understanding the nature of superhard graphite. *Scientific Reports* **2** (2012).

[26] W. Bragg. The diffraction of short electromagnetic waves by a crystal. In *Proceedings of the Cambridge Philosophical Society*, vol. 17, pp. 43–57 (1913).

[27] S. Brorson, J. Fujimoto, and E. Ippen. Femtosecond electronic heat-transport dynamics in thin gold films. *Physical Review Letters* **59**:1962 (1987).

[28] S. Brorson, A. Kazeroonian, J. Moodera, D. Face, T. Cheng, E. Ippen, M. Dresselhaus, and G. Dresselhaus. Femtosecond room-temperature measurement of the electron-phonon coupling constant γ in metallic superconductors. *Physical Review Letters* **64**:2172 (1990).

[29] H. Brysk. Electron-ion equilibration in a partially degenerate plasma. *Plasma Physics* **16**:927 (1974).

[30] E. Burkel. Introduction to x-ray scattering. *Journal of Physics: Condensed Matter* **13**:7477 (2001).

[31] M. Calandra and F. Mauri. Electron-phonon coupling and electron self-energy in electron-doped graphene: Calculation of angular-resolved photoemission spectra. *Physical Review B* **76**:205411 (2007).

[32] E. M. Campbell, N. C. Holmes, S. B. Libby, B. A. Remington, and E. Teller. The evolution of high-energy-density physics: from nuclear testing to the superlasers. *Laser and Particle Beams* **15**:607–626 (1997).

[33] P. Celliers, A. Ng, G. Xu, and A. Forsman. Thermal equilibration in a shock wave. *Physical Review Letters* **68**:2305 (1992).

[34] D. M. Ceperley and B. Alder. Ground state of the electron gas by a stochastic method. *Physical Review Letters* **45**:566 (1980).

[35] Z. Chen, B. Holst, S. Kirkwood, V. Sametoglu, M. Reid, Y. Tsui, V. Recoules, and A. Ng. Evolution of ac conductivity in nonequilibrium warm dense gold. *Physical Review Letters* **110**:135001 (2013).

[36] L. Chhabildas, L. Davison, and Y. Horie. *High-Pressure Shock Compression of Solids VIII: The Science and Technology of High-Velocity Impact*. Shock Wave and High Pressure Phenomena (Springer, 2006).

[37] J. Chihara. Difference in x-ray scattering between metallic and non-metallic liquids due to conduction electrons. *Journal of Physics F: Metal Physics* **17**:295 (1987).

[38] J. Chihara. Interaction of photons with plasmas and liquid metals-photoabsorption and scattering. *Journal of Physics: Condensed Matter* **12**:231 (2000).

[39] M. Coury, D. Carroll, A. Robinson, X. Yuan, C. Brenner, M. Burza, R. Gray, K. Lancaster, Y. Li, X. Lin, *et al.* Injection and transport properties of fast electrons in ultraintense laser-solid interactions. *Physics of Plasmas* **20**:043104 (2013).

[40] J. Daligault and S. Gupta. Electron–ion scattering in dense multi-component plasmas: Application to the outer crust of an accreting neutron star. *The Astrophysical Journal* **703**:994 (2009).

[41] J.-F. Danel, L. Kazandjian, and G. Zérah. Equation of state of dense plasmas by ab initio simulations: Bridging the gap between quantum molecular dynamics and orbital-free molecular dynamics at high temperature. *Physics of Plasmas* **19**:122712 (2012).

[42] M. S. Daw and M. Baskes. Semiempirical, quantum mechanical calculation of hydrogen embrittlement in metals. *Physical Review Letters* **50**:1285 (1983).

[43] P. Debye. *The collected papers of Peter J.W. Debye* (Ox Bow Press, 1954).

[44] B. J. Demaske, V. V. Zhakhovsky, N. A. Inogamov, and I. I. Oleynik. Ultrashort shock waves in nickel induced by femtosecond laser pulses. *Phys. Rev. B* **87**:054109 (2013).

[45] P. Dendy and B. Heaton. *Physics for Diagnostic Radiology, Third Edition*. Series in Medical Physics and Biomedical Engineering (Taylor & Francis, 2011).

[46] M. Dharma-Wardana. Static and dynamic conductivity of warm dense matter within a density-functional approach: Application to aluminum and gold. *Physical Review E* **73**:036401 (2006).

[47] M. Dharma-Wardana and F. Perrot. Energy relaxation and the quasiequation of state of a dense two-temperature nonequilibrium plasma. *Physical Review E* **58**:3705 (1998).

[48] M. W. C. Dharma-wardana and F. Perrot. Erratum: Energy relaxation and the quasiequation of state of a dense two-temperature nonequilibrium plasma. *Physical Review E* **63**:069901 (2001).

[49] G. Dimonte and J. Daligault. Molecular-dynamics simulations of electron-ion temperature relaxation in a classical coulomb plasma. *Physical Review Letters* **101**:135001 (2008).

[50] Z. Donkó and P. Hartmann. Thermal conductivity of strongly coupled Yukawa liquids. *Physical Review E* **69**:016405 (2004).

[51] Z. Donkó and P. Hartmann. Shear viscosity of strongly coupled yukawa liquids. *Physical Review E* **78**:026408 (2008).

[52] R. Drake. *High-Energy-Density Physics: Fundamentals, Inertial Fusion, and Experimental Astrophysics*. Shock Wave and High Pressure Phenomena (Springer, 2006).

[53] L. Dubrovinsky, N. Dubrovinskaia, V. B. Prakapenka, and A. M. Abakumov. Implementation of micro-ball nanodiamond anvils for high-pressure studies above 6 [thinsp] mbar. *Nature communications* **3**:1163 (2012).

[54] H. Elsayed-Ali and T. Juhasz. Femtosecond time-resolved thermomodulation of thin gold films with different crystal structures. *Physical Review B* **47**:13599 (1993).

[55] R. Ernstorfer, M. Harb, C. T. Hebeisen, G. Sciaini, T. Dartigalongue, and R. D. Miller. The formation of warm dense matter: Experimental evidence for electronic bond hardening in gold. *Science* **323**:1033–1037 (2009).

[56] P. Ewald. *Fifty years of X-ray diffraction: Dedicated to the International Union of Crystallography on the occasion of the commemoration meeting in Munich, July 1962* (Published for the International Union of Crystallography by A. Oosthoek's Uitgeversmij., 1962).

[57] K. Falk. Measurement of equation of state of compressed hydrogen and deuterium. D. Phil. Merton College, University of Oxford (2011).

[58] L. Fletcher, E. Galtier, P. Heimann, H. Lee, B. Nagler, J. Welch, U. Zastrau, J. Hastings, and S. Glenzer. Plasmon measurements with a seeded x-ray laser. *Journal of Instrumentation* **8**:C11014 (2013).

[59] E. Förster, K. Goetz, K. Schäfer, and W. Zimmer. Laser generated plasma as a source for real time studies in x-ray crystal research: Part i: Fundamental remarks about source characteristics and requirements. *Laser and particle beams* **2**:167–185 (1984).

[60] D. Frenkel and B. Smit. *Understanding Molecular Simulation: From Algorithms to Applications*. Computational science series (Elsevier Science, 2001).

[61] K. Gaffney, A. Lindenberg, J. Larsson, K. Sokolowski-Tinten, C. Blome, O. Synnergren, *et al.* Observation of structural anisotropy and the onset of liquidlike motion during the nonthermal melting of insb. *Phys. Rev. Lett.* **95**:125701 (2005).

[62] S. Galambosi. Electronic excitations in solids studied unsing inelastic x-ray scattering. PhD. University Of Helsinki (2007).

[63] D. Gericke. Kinetic approach to temperature relaxation in dense plasmas. In *Journal of Physics: Conference Series*, vol. 11, p. 111 (IOP Publishing, 2005).

[64] D. Gericke, S. Kosse, M. Schlanges, and M. Bonitz. T-matrix approach to equilibium and nonequilibrium carrier-carrier scattering in semiconductors. *Physical Review B* **59**:10639 (1999).

[65] D. Gericke, M. Murillo, and M. Schlanges. Dense plasma temperature equilibration in the binary collision approximation. *Physical Review E* **65**:036418 (2002).

[66] D. O. Gericke and J. Vorberger. Energy transfer rates in dense two-temperature plasmas with degenerate electrons. Tech. rep., Central Laser Facility Annual Report, 2006/2007 (2010).

[67] D. O. Gericke, J. Vorberger, K. Wünsch, and G. Gregori. Screening of ionic cores in partially ionized plasmas within linear response. *Physical Review E* **81**:065401 (2010).

[68] T. C. Germann and K. Kadau. Trillion-Atom Molecular Dynamics Becomes a Reality. *International Journal of Modern Physics C* **19**:1315–1319 (2008).

[69] J. B. Gibson, A. N. Goland, M. Milgram, and G. H. Vineyard. Dynamics of radiation damage. *Physical Review* **120**:1229–1253 (1960).

[70] B. Giordano. *De linfinito, universo e mondi* (1584).

[71] S. Glenzer, B. MacGowan, P. Michel, N. Meezan, L. Suter, S. Dixit, J. Kline, G. Kyrala, D. Bradley, D. Callahan, *et al.* Symmetric inertial confinement fusion implosions at ultra-high laser energies. *Science* **327**:1228–1231 (2010).

[72] S. H. Glenzer, O. L. Landen, P. Neumayer, R. W. Lee, K. Widmann, S. W. Pollaine, R. J. Wallace, G. Gregori, A. Höll, T. Bornath, R. Thiele, V. Schwarz, W.-D. Kraeft, and R. Redmer. Observations of plasmons in warm dense matter. *Physical Review Letters* **98**:065002 (2007).

[73] S. H. Glenzer and R. Redmer. X-ray Thomson scattering in high energy density plasmas. *Reviews of Modern Physics* **81**:1625 (2009).

[74] X. Gonze, B. Amadon, P.-M. Anglade, J.-M. Beuken, F. Bottin, P. Boulanger, F. Bruneval, D. Caliste, R. Caracas, M. Cote, *et al.* Abinit: First-principles approach to material and nanosystem properties. *Computer Physics Communications* **180**:2582–2615 (2009).

[75] F. R. Graziani, V. S. Batista, L. X. Benedict, J. I. Castor, H. Chen, S. N. Chen, C. A. Fichtl, J. N. Glosli, P. E. Grabowski, A. T. Graf, *et al.* Large-scale molecular dynamics simulations of dense plasmas: The cimarron project. *High Energy Density Physics* **8**:105–131 (2012).

[76] J. Green, V. Ovchinnikov, R. Evans, K. Akli, H. Azechi, F. Beg, C. Bellei, R. Freeman, H. Habara, R. Heathcote, *et al.* Effect of laser intensity on fast-electron-beam divergence in solid-density plasmas. *Physical Review Letters* **100**:015003 (2008).

[77] G. Gregori and D. O. Gericke. A reduced coupled-mode description for the electron-ion energy relaxation in dense matter. *EPL (Europhysics Letters)* **83**:15002 (2008).

[78] G. Gregori and D. O. Gericke. Low frequency structural dynamics of warm dense matter. *Physics of Plasmas* **16**:056306 (2009).

[79] G. Gregori, S. Glenzer, and O. Landen. Generalized x-ray scattering cross section from nonequilibrium plasmas. *Physical Review E* **74**:026402 (2006).

[80] G. Gregori, S. Glenzer, W. Rozmus, R. Lee, and O. Landen. Theoretical model of x-ray scattering as a dense matter probe. *Physical Review E* **67**:026412 (2003).

[81] T. Guillot. Interiors of giant planets inside and outside the solar system. *Science* **286**:72–77 (1999).

[82] D. W. Hamacher II. A search for transiting extrasolar planets from the southern hemisphere. Master's Thesis University of New South Wales (2008).

[83] S. Hamaguchi, R. Farouki, and D. Dubin. Triple point of yukawa systems. *Physical Review E* **56**:4671 (1997).

[84] S. Hamaguchi, R. T. Farouki, and D. H. E. Dubin. Phase diagram of Yukawa systems near the one-component-plasma limit revisited. *The Journal of Chemical Physics* **105**:7641 (1996).

[85] S. Hamel. Personal Communication (2013).

[86] J. Hansen and I. McDonald. *Theory of Simple Liquids* (Elsevier Science, 2006).

[87] N. Harrison. An introduction to density functional theory. *NATO Science Series, III: Computer and Systems Sciences* **187**:45–70 (2003).

[88] P. Hart, S. Boutet, G. CarmI, A. Dragone, B. Duda, D. Freytag, G. Haller, R. Herbst, S. Herrmann, C. Kenney, J. Morse, M. Nordby, J. Pines, N. van Bakel, M. Weaver, and G. Williams. The cornell-slac pixel array detector at LCLS. In *Nuclear Science Symposium and Medical Imaging Conference (NSS/MIC), 2012 IEEE*, pp. 538–541 (2012).

[89] V. Heine. The pseudopotential concept. *Solid State Physics* **24**:1–36 (1970).

[90] J. Helliwell and P. Rentzepis. *Time-resolved Diffraction*. Oxford Series on Synchrotron Radiation (Clarendon Press, 1997).

[91] H. Herman. *Treatise on Materials Science and Technology*. v. 8 (Elsevier Science, 2013).

[92] A. Higginbotham. Shock induced phase transitions in iron: Studies via exafs and x-ray diffraction. D. Phil. Hartford College, University of Oxford (2009).

[93] N. R. C. Committee on High Energy Density Plasma Physics, Plasma Science Committee. *Frontiers in High Energy Density Physics:The X-Games of Contemporary Science* (The National Academies Press, 2003).

[94] J. Hohlfeld, S.-S. Wellershoff, J. Güdde, U. Conrad, V. Jähnke, and E. Matthias. Electron and lattice dynamics following optical excitation of metals. *Chemical Physics* **251**:237–258 (2000).

[95] N. C. Holmes, J. A. Moriarty, G. R. Gathers, and W. J. Nellis. The equation of state of platinum to 660 gpa (6.6 mbar). *Journal of Applied Physics* **66** (1989).

[96] C. Huang and E. A. Carter. Transferable local pseudopotentials for magnesium, aluminum and silicon. *Physical Chemistry Chemical Physics* **10**:7109–7120 (2008).

[97] S. Huotari, G. Vankó, F. Albergamo, C. Ponchut, H. Graafsma, C. Henriquet, R. Verbeni, and G. Monaco. Improving the performance of high-resolution x-ray spectrometers with position-sensitive pixel detectors. *Journal of Synchrotron Radiation* **12**:467–472 (2005).

[98] S. Ichimaru. Strongly coupled plasmas: high-density classical plasmas and degenerate electron liquids. *Reviews of Modern Physics* **54**:1017 (1982).

[99] S. Ichimaru. *Statistical Plasma Physics, Volume II: Condensed plasmas*. Frontiers in Physics Series (Westview Press, 2004).

[100] S. Ichimaru. *Statistical Plasma Physics, Volume I: Basic Principles*. Frontiers in Physics Series (Westview Press, 2008).

[101] Y. Ishida, T. Togashi, K. Yamamoto, M. Tanaka, T. Taniuchi, T. Kiss, M. Nakajima, T. Suemoto, and S. Shin. Non-thermal hot electrons ultrafastly generating hot optical phonons in graphite. *Scientific Reports* **1** (2011).

[102] J. Jackson. *Classical Electrodynamics* (Wiley, 1998).

[103] A. Javan, W. R. Bennett, and D. R. Herriott. Population inversion and continuous optical maser oscillation in a gas discharge containing a he-ne mixture. *Physical Review Letters* **6**:106–110 (1961).

[104] Q. Johnson, A. Mitchell, R. N. Keeler, and L. Evans. X-ray diffraction during shock-wave compression. *Physical Review Letters* **25**:1099–1101 (1970).

[105] T. Juhasz, H. Elsayed-Ali, G. Smith, C. Suarez, and W. Bron. Direct measurements of the transport of nonequilibrium electrons in gold films with different crystal structures. *Physical Review B* **48**:15488 (1993).

[106] K. Kadau, T. C. Germann, P. S. Lomdahl, and B. L. Holian. Microscopic view of structural phase transitions induced by shock waves. *Science* **296**:1681–1684 (2002).

[107] S. Kar, A. Robinson, D. Carroll, O. Lundh, K. Markey, P. McKenna, P. Norreys, and M. Zepf. Guiding of relativistic electron beams in solid targets by resistively controlled magnetic fields. *Physical Review Letters* **102**:055001 (2009).

[108] G. Kimminau. Studies of shock-induced plasticity by use of molecular dynamics and x-ray diffraction. D. Phil. Linacre College, University of Oxford (2009).

[109] M. Klein, F. Hache, D. Ricard, and C. Flytzanis. Size dependence of electron-phonon coupling in semiconductor nanospheres: The case of cdse. *Physical Review B* **42**:11123 (1990).

[110] D. Kraus, J. Vorberger, D. O. Gericke, V. Bagnoud, A. Blažević, W. Cayzac, A. Frank, G. Gregori, A. Ortner, A. Otten, *et al.* Probing the complex ion structure in liquid carbon at 100 GPa. *Physical Review Letters* **111**:255501 (2013).

[111] A. L. Kritcher, P. Neumayer, J. Castor, T. Döppner, R. W. Falcone, O. L. Landen, H. J. Lee, R. W. Lee, E. C. Morse, A. Ng, *et al.* Ultrafast x-ray thomson scattering of shock-compressed matter. *Science* **322**:69–71 (2008).

[112] A. Kugler. Theory of the local field correction in an electron gas. *Journal of Statistical Physics* **12**:35–87 (1975).

[113] S. Kurth, J. P. Perdew, and P. Blaha. Molecular and solid-state tests of density functional approximations: LSD, GGAs, and meta-GGAs. *International Journal of Quantum Chemistry* **75**:889–909 (1999).

[114] L. Landau. Kinetic equation for the coulomb effect. *Physikalische Zeitschrift der Sowjetunion* **10**:154 (1936).

[115] K. W. D. Ledingham and W. Galster. Laser-driven particle and photon beams and some applications. *New Journal of Physics* **12**:66 (2010).

[116] J. Lee, S. Han, and J. Inoue. Sharp contrasts in low-energy quasiparticle dynamics of graphite between brillouin zone k and h points. *Physical Review Letters* **100**:216801 (2008).

[117] C. Leem, B. Kim, C. Kim, S. Park, T. Ohta, A. Bostwick, E. Rotenberg, H.-D. Kim, M. Kim, H. Choi, *et al.* Effect of linear density of states on the quasiparticle dynamics and small electron-phonon coupling in graphite. *Physical Review Letters* **100**:016802 (2008).

[118] P. Leguay, A. Lévy, B. Chimier, F. Deneuville, D. Descamps, C. Fourment, C. Goyon, S. Hulin, S. Petit, O. Peyrusse, *et al.* Ultrafast short-range disordering of femtosecond-laser-heated warm dense aluminum. *Physical Review Letters* **111**:245004 (2013).

[119] M. Ligges, I. Rajkovic, P. Zhou, O. Posth, C. Hassel, G. Dumpich, and D. Von der Linde. Observation of ultrafast lattice heating using time resolved electron diffraction. *Applied Physics Letters* **94**:1910 (2009).

[120] Z. Lin, L. V. Zhigilei, and V. Celli. Electron-phonon coupling and electron heat capacity of metals under conditions of strong electron-phonon nonequilibrium. *Physical Review B* **77**:075133 (2008).

[121] A. Lindenberg, I. Kang, S. Johnson, T. Missalla, P. Heimann, Z. Chang, J. Larsson, P. Bucksbaum, H. Kapteyn, H. Padmore, R. Lee, J. Wark, and R. Falcone. Time-resolved x-ray diffraction from coherent phonons during a laser-induced phase transition. *Phys. Rev. Lett.* **84**:111–114 (2000).

[122] A. M. Lindenberg, J. Larsson, K. Sokolowski-Tinten, K. Gaffney, C. Blome, O. Synnergren, J. Sheppard, C. Caleman, A. MacPhee, D. Weinstein, *et al.* Atomic-scale visualization of inertial dynamics. *Science* **308**:392–395 (2005).

[123] T. Ma, T. Döppner, R. Falcone, L. Fletcher, C. Fortmann, D. Gericke, O. Landen, H. Lee, A. Pak, J. Vorberger, *et al.* X-ray scattering measurements of strong ion-ion correlations in shock-compressed aluminum. *Physical Review Letters* **110**:065001 (2013).

[124] J. MacFarlane, I. Golovkin, and P. Woodruff. Helios-cr a 1-d radiation-magnetohydrodynamics code with inline atomic kinetics modeling. *Journal of Quantitative Spectroscopy and Radiative Transfer* **99**:381–397 (2006).

[125] T. H. Mainman. Stimulated optical radiation in ruby. *Nature* **187**:493–494 (1960).

[126] M. Mattesini, A. B. Belonoshko, E. Buforn, M. Ramirez, S. Simak, A. Udias, H.-K. Mao, and R. Ahuja. Hemispherical anisotropic patterns of the earths inner core. *Proceedings of the National Academy of Sciences of the United States of America* **107**:9507–9512 (2010).

[127] M. K. Matzen, M. Sweeney, R. Adams, J. Asay, J. Bailey, G. Bennett, D. Bliss, D. Bloomquist, T. Brunner, R. Campbell, *et al.* Pulsed-power-driven high energy density physics and inertial confinement fusion research. *Physics of Plasmas* **12**:055503 (2005).

[128] F. McClung and R. Hellwarth. Giant optical pulsations from ruby. *Journal of Applied Physics* **33**:828–829 (1962).

[129] C. F. McConaghy and L. W. Coleman. Picosecond xray streak camera. *Applied Physics Letters* **25** (1974).

[130] A. Michette and C. Buckley. *X-Ray Science and Technology,* (Taylor & Francis, 1993).

[131] D. Milathianaki, S. Boutet, G. Williams, A. Higginbotham, D. Ratner, A. Gleason, M. Messerschmidt, M. M. Seibert, D. Swift, P. Hering, *et al.* Femtosecond visualization of lattice dynamics in shock-compressed matter. *Science* **342**:220–223 (2013).

[132] T. Missalla, I. Uschmann, E. Förster, G. Jenke, and D. Von der Linde. Monochromatic focusing of subpicosecond x-ray pulses in the kev range. *Review of Scientific Instruments* **70**:1288–1299 (1999).

[133] J. P. Mithen. Molecular dynamics simulations of the equilibrium dynamics of non-ideal plasmas. D. Phil. Trinity College, University of Oxford (2012).

[134] J. P. Mithen. Personal Communication (2013).

[135] J. P. Mithen, J. Daligault, B. J. Crowley, and G. Gregori. Density fluctuations in the Yukawa one-component plasma: An accurate model for the dynamical structure factor. *Physical Review E* **84**:046401 (2011).

[136] J. P. Mithen, J. Daligault, and G. Gregori. Extent of validity of the hydrodynamic description of ions in dense plasmas. *Physical Review E* **83**:015401 (2011).

[137] H. W. Mocker and R. Collins. Mode competition and self-locking effects in a q-switched ruby laser. *Applied Physics Letters* **7**:270–273 (1965).

[138] I. Morozov, H. Reinholz, G. Röpke, A. Wierling, and G. Zwicknagel. Molecular dynamics simulations of optical conductivity of dense plasmas. *Physical Review E* **71**:066408 (2005).

[139] R. L. Mössbauer and W. H. Wiedemann. Kernresonanzabsorption nicht dopplerverbreiterter gammastrahlung in re187. *Zeitschrift für Physik* **159**:33–48 (1960).

[140] B. Mueller and B. Rethfeld. Relaxation dynamics in laser-excited metals under nonequilibrium conditions. *Physical Review B* **87**:035139 (2013).

[141] G. A. Naylor, K. Scheidt, J. Larsson, M. Wulff, and J. M. Filhol. A sub-picosecond accumulating streak camera for x-rays. *Measurement Science and Technology* **12**:1858 (2001).

[142] N. Nettelmann, R. Redmer, and D. Blaschke. Warm dense matter in giant planets and exoplanets. *Physics of Particles and Nuclei* **39**:1122–1127 (2008).

[143] A. Ng. Outstanding questions in electron–ion energy relaxation, lattice stability, and dielectric function of warm dense matter. *International Journal of Quantum Chemistry* **112**:150–160 (2012).

[144] A. Ng, P. Celliers, G. Xu, and A. Forsman. Electron-ion equilibration in a strongly coupled plasma. *Physical Review E* **52**:4299 (1995).

[145] M. Nicoul, U. Shymanovich, A. Tarasevitch, D. von der Linde, and K. Sokolowski-Tinten. Picosecond acoustic response of a laser-heated gold-film studied with time-resolved x-ray diffraction. *Applied Physics Letters* **98**:191902 (2011).

[146] H. Ohta and S. Hamaguchi. Molecular dynamics evaluation of self-diffusion in Yukawa systems. *Physics of Plasmas* **7**:4506 (2000).

[147] A. Pak, G. Gregori, J. Knight, K. Campbell, D. Price, B. Hammel, O. L. Landen, and S. H. Glenzer. X-ray line measurements with high efficiency bragg crystals. *Review of Scientific Instruments* **75** (2004).

[148] R. Parr and W. Yang. *Density-Functional Theory of Atoms and Molecules*. International Series of Monographs on Chemistry (Oxford University Press, USA, 1989).

[149] M. Passoni, L. Bertagna, and A. Zani. Target normal sheath acceleration: theory, comparison with experiments and future perspectives. *New Journal of Physics* **12**:045012 (2010).

[150] A. Pelka, G. Gregori, D. O. Gericke, J. Vorberger, S. Glenzer, M. Günther, K. Harres, R. Heathcote, A. Kritcher, N. Kugland, *et al.* Ultrafast melting of carbon induced by intense proton beams. *Physical Review Letters* **105**:265701 (2010).

[151] J. P. Perdew, K. Burke, and M. Ernzerhof. Generalized gradient approximation made simple. *Physical Review Letters* **77**:3865 (1996).

[152] M. Pessot, P. Maine, and G. Mourou. 1000 times expansion/compression of optical pulses for chirped pulse amplification. *Optics Communications* **62**:419 – 421 (1987).

[153] K. J. Peterson, P. Y. Edmund, D. B. Sinars, M. E. Cuneo, S. A. Slutz, J. M. Koning, M. M. Marinak, C. Nakhleh, and M. C. Herrmann. Simulations of electrothermal instability growth in solid aluminum rods. *Physics of Plasmas* **20**:056305 (2013).

[154] K. J. Peterson, D. B. Sinars, P. Y. Edmund, M. C. Herrmann, M. E. Cuneo, S. A. Slutz, I. C. Smith, B. W. Atherton, M. D. Knudson, and C. Nakhleh. Electrothermal instability growth in magnetically driven pulsed power liners. *Physics of Plasmas* **19**:092701 (2012).

[155] S. Piscanec, M. Lazzeri, F. Mauri, A. Ferrari, and J. Robertson. Kohn anomalies and electron-phonon interactions in graphite. *Physical Review Letters* **93**:185503 (2004).

[156] S. Plimpton. Fast parallel algorithms for short-range molecular dynamics. *Journal of Computational Physics* **117**:1–19 (1995).

[157] B. V. Prasad, M. E. Hardy, T. Dokland, J. Bella, M. G. Rossmann, and M. K. Estes. X-ray crystallographic structure of the norwalk virus capsid. *Science* **286**:287–290 (1999).

[158] W. Press. *Numerical Recipes 3rd Edition: The Art of Scientific Computing* (Cambridge University Press, 2007).

[159] E. Prince and I. U. of Crystallography. *International Tables for Crystallography, Mathematical, Physical and Chemical Tables*. International Tables for Crystallography (Wiley, 2004).

[160] A. Rahman. Correlations in the motion of atoms in liquid argon. *Physical Review* **136**:A405–A411 (1964).

[161] V. Recoules, F. Lambert, A. Decoster, B. Canaud, and J. Clérouin. Ab initio determination of thermal conductivity of dense hydrogen plasmas. *Physical Review Letters* **102**:075002 (2009).

[162] B. A. Remington, R. P. Drake, and D. D. Ryutov. Experimental astrophysics with high power lasers and z pinches. *Reviews of Modern Physics* **78**:755 (2006).

[163] D. Riley, N. Woolsey, D. McSherry, I. Weaver, A. Djaoui, and E. Nardi. X-ray diffraction from a dense plasma. *Physical Review Letters* **84**:1704 (2000).

[164] L. Robson, P. Simpson, R. Clarke, K. Ledingham, F. Lindau, O. Lundh, T. McCanny, P. Mora, D. Neely, C.-G. Wahlström, *et al.* Scaling of proton acceleration driven by petawatt-laser–plasma interactions. *Nature Physics* **3**:58–62 (2006).

[165] W. C. Röntgen. On a new kind of rays. *The British Journal of Radiology* **4**:32–33 (1931).

[166] C. Rose-Petruck, R. Jimenez, T. Guo, A. Cavalleri, C. W. Siders, F. Rksi, J. A. Squier, B. C. Walker, K. R. Wilson, and C. P. Barty. Picosecond–milliångström lattice dynamics measured by ultrafast x-ray diffraction. *Nature* **398**:310–312 (1999).

[167] M. Roth. The diagnostics of ultra-short pulse laser-produced plasma. *Journal of Instrumentation* **6**:R09001–R09001 (2011).

[168] M. Roth, I. Alber, V. Bagnoud, C. Brown, R. Clarke, H. Daido, J. Fernandez, K. Flippo, S. Gaillard, C. Gauthier, *et al.* Proton acceleration experiments and warm dense matter research using high power lasers. *Plasma Physics and Controlled Fusion* **51**:124039 (2009).

[169] H. R. Rüter and R. Redmer. Ab initio simulations for the ion-ion structure factor of warm dense aluminum. *Physical Review Letters* **112**:145007 (2014).

[170] T. Saigo and S. Hamaguchi. Shear viscosity of strongly coupled Yukawa systems. *Physics of Plasmas* **9**:1210 (2002).

[171] E. G. Saiz, G. Gregori, D. O. Gericke, J. Vorberger, B. Barbrel, R. Clarke, R. R. Freeman, S. Glenzer, F. Khattak, M. Koenig, *et al.* Probing warm dense lithium by inelastic x-ray scattering. *Nature Physics* **4**:940–944 (2008).

[172] G. Salin. Hydrodynamic limit of the Yukawa one-component plasma. *Physics of Plasmas* **14**:082316 (2007).

[173] G. Salin and J.-M. Caillol. Equilibrium molecular dynamics simulations of the transport coefficients of the Yukawa one component plasma. *Physics of Plasmas (1994-present)* **10** (2003).

[174] D. Salzmann. *Atomic Physics in Hot Plasmas*. International series of monographs on physics (Oxford University Press, USA, 1998).

[175] K. Y. Sanbonmatsu and M. S. Murillo. Shear viscosity of strongly coupled Yukawa systems on finite length scales. *Physical Review Letters* **86**:1215–1218 (2001).

[176] K. Schafer and W. Zimmer. Laser generated plasmas as a source lor real time studies in x-ray crystal research part ii: In search of an optimum choice of laser plasma coupling conditions. *Laser and Particle Beams* **2**:187–199 (1984).

[177] S. Schäfer, W. Liang, and A. H. Zewail. Primary structural dynamics in graphite. *New Journal of Physics* **13**:063030 (2011).

[178] M. Scheuch, T. Kampfrath, M. Wolf, K. Von Volkmann, C. Frischkorn, and L. Perfetti. Temperature dependence of ultrafast phonon dynamics in graphite. *Applied Physics Letters* **99**:211908 (2011).

[179] R. Schmidt, B. Crowley, J. Mithen, and G. Gregori. Quantum hydrodynamics of strongly coupled electron fluids. *Physical Review E* **85**:046408 (2012).

[180] J. Schneider, C. Dedieu, P. Le Sidaner, R. Savalle, and I. Zolotukhin. Defining and cataloging exoplanets: the exoplanet. eu database. *Astronomy & Astrophysics* **532**:A79 (2011).

[181] T. Scopigno, U. Balucani, G. Ruocco, and F. Sette. Collective dynamics of liquid aluminum probed by inelastic x-ray scattering. *Physical Review E* **63**:011210 (2000).

[182] H. Sheng, M. Kramer, A. Cadien, T. Fujita, and M. Chen. Highly optimized embedded-atom-method potentials for fourteen fcc metals. *Physical Review B* **83**:134118 (2011).

[183] L. Spitzer. *Physics of Fully Ionized Gases*. Interscience tracts on physics and astronomy (Interscience Publ., 1964).

[184] T. Starke. PHERMEX standing-wave linear electron accelerator. *IEEE Transactions on Nuclear Science* **30**:1402–1404 (1983).

[185] V. N. Staroverov, G. E. Scuseria, J. Tao, and J. P. Perdew. Tests of a ladder of density functionals for bulk solids and surfaces. *Physical Review B* **69**:075102 (2004).

[186] D. Strickland and G. Mourou. Compression of amplified chirped optical pulses. *Optics Communications* **56**:219 – 221 (1985).

[187] C. Suarez, W. Bron, and T. Juhasz. Dynamics and transport of electronic carriers in thin gold films. *Physical Review Letters* **75**:4536 (1995).

[188] K. Sugawara, T. Sato, S. Souma, T. Takahashi, and H. Suematsu. Anomalous quasiparticle lifetime and strong electron-phonon coupling in graphite. *Physical Review Letters* **98**:036801 (2007).

[189] D. C. Swift. Properties of plastic ablators in laser-driven material dynamics experiments. *Physical Review E* **77**:066402 (2008).

[190] A. Thomas, M. Sherlock, C. Kuranz, C. Ridgers, and R. Drake. Hybrid vlasov–fokker–planck–maxwell simulations of fast electron transport and the time dependance of k-shell excitation in a mid-z metallic target. *New Journal of Physics* **15**:015017 (2013).

[191] V. A. Tsukermann and A. I. Andeenko. *Zhurnal Tekhnicheskoi Fiziki* **12**:185 (1942).

[192] M. E. Tuckerman and G. J. Martyna. Understanding modern molecular dynamics: techniques and applications. *The Journal of Physical Chemistry B* **104**:159–178 (2000).

[193] M. E. Tuckerman and G. J. Martyna. Understanding modern molecular dynamics: techniques and applications. *The Journal of Physical Chemistry B* **104**:159–178 (2000).

[194] A. Tuffanelli, M. Sanchez del Rio, G. Pareschi, M. Gambaccini, A. Taibi, A. Fantini, and M. Ohler. Comparative characterization of highly oriented pyrolytic graphite by means of diffraction topography (1999).

[195] L. Verlet. Computer experiments on classical fluids. I. thermodynamical properties of Lennard-Jones molecules. *Physical Review* **159**:98 (1967).

[196] J. Vorberger. Personal Communication (2012).

[197] J. Vorberger, Z. Donko, I. Tkachenko, and D. O. Gericke. Dynamic ion structure factor of warm dense matter. *Physical Review Letters* **109**:225001 (2012).

[198] J. Vorberger and D. Gericke. Effective ion–ion potentials in warm dense matter. *High Energy Density Physics* **9**:178–186 (2013).

[199] J. Vorberger and D. O. Gericke. Coupled mode effects on energy transfer in weakly coupled, two-temperature plasmas. *Physics of Plasmas* **16**:082702 (2009).

[200] J. Vorberger, D. O. Gericke, T. Bornath, and M. Schlanges. Energy relaxation in dense, strongly coupled two-temperature plasmas. *Physical Review E* **81**:046404 (2010).

[201] J. Wark. X-ray diffraction: Table-top picosecond sources. *Nature* **398**:284–285 (1999).

[202] B. Warren. *X-Ray Diffraction*. Dover Books on Physics (Dover Publications, 2012).

[203] J. D. Watson and F. H. Crick. Molecular structure of nucleic acids: A structure for deoxyribose nucleic acid. *Nature* **171**:737–738 (1953).

[204] S. Weir, A. Mitchell, and W. Nellis. Metallization of fluid molecular hydrogen at 140 gpa (1.4 mbar). *Physical Review Letters* **76**:1860 (1996).

[205] S.-S. Wellershoff, J. Hohlfeld, J. Güdde, and E. Matthias. The role of electron–phonon coupling in femtosecond laser damage of metals. *Applied Physics A* **69**:S99–S107 (1999).

[206] T. G. White, N. J. Hartley, B. Borm, B. Crowley, J. Harris, D. Hochhaus, T. Kaempfer, K. Li, P. Neumayer, L. K. Pattison, *et al.* Electron-ion equilibration in ultrafast heated graphite. *Physical Review Letters* **112**:145005 (2014).

[207] T. G. White, P. Mabey, D. O. Gericke, N. J. Hartley, H. Doyle, D. McGonegle, D. S. Rackstraw, A. Higginbotham, and G. Gregori. Electron-phonon equilibration in laser-heated gold films. *Physical Review B* **90**:014305 (2014).

[208] T. G. White, S. Richardson, B. J. B. Crowley, L. Pattison, J. W. O. Harris, and G. Gregori. Orbital-free density-functional theory simulations of the dynamic structure factor of warm dense aluminum. *Physical Review Letters* **111**:175002 (2013).

[209] T. G. White, J. Vorberger, C. R. D. Brown, B. J. B. Crowley, P. Davis, S. H. Glenzer, J. W. O. Harris, D. C. Hochhaus, S. Le Pape, T. Ma, *et al.* Observation of inhibited electron-ion coupling in strongly heated graphite. *Scientific Reports* **2** (2012).

[210] S. Wilks, A. Langdon, T. Cowan, M. Roth, M. Singh, S. Hatchett, M. Key, D. Pennington, A. MacKinnon, and R. Snavely. Energetic proton generation in ultra-intense laser–solid interactions. *Physics of Plasmas* **8**:542–549 (2001).

[211] P. Willmott. *An Introduction to Synchrotron Radiation: Techniques and Applications* (Wiley, 2011).

[212] A. Wolszczan and D. A. Frail. A planetary system around the millisecond pulsar psr 1257+ 12. *Nature* **355**:145–147 (1992).

[213] O. B. Wright. Ultrafast nonequilibrium stress generation in gold and silver. *Physical Review B* **49**:9985 (1994).

[214] Q. Wu and W. Yang. A direct optimization method for calculating density functionals and exchangecorrelation potentials from electron densities. *The Journal of Chemical Physics* **118**:2498 (2003).

[215] H. Yan, D. Song, K. F. Mak, I. Chatzakis, J. Maultzsch, and T. F. Heinz. Time-resolved Raman spectroscopy of optical phonons in graphite: Phonon anharmonic coupling and anomalous stiffening. *Physical Review B* **80**:121403 (2009).

[216] U. Zastrau, P. Audebert, V. Bernshtam, E. Brambrink, T. Kämpfer, E. Kroupp, R. Loetzsch, Y. Maron, Y. Ralchenko, H. Reinholz, *et al.* Temperature and K_α-yield radial distributions in laser-produced solid-density plasmas imaged with ultrahigh-resolution x-ray spectroscopy. *Physical Review E* **81**:026406 (2010).

[217] B. Zhou, Y. Alexander Wang, and E. Carter. Transferable local pseudopotentials derived via inversion of the Kohn-Sham equations in a bulk environment. *Physical Review B* **69**:125109 (2004).

[218] S. Zhou, G.-H. Gweon, J. Graf, A. Fedorov, C. Spataru, R. Diehl, Y. Kopelevich, D.-H. Lee, S. G. Louie, and A. Lanzara. First direct observation of Dirac fermions in graphite. *Nature Physics* **2**:595–599 (2006).